Mag. rer. nat. Isabella Rojs BSc

Assessment of Input Parameters for Climate Models Based on Remote Sensing Technology

MASTER'S THESIS

to achieve the university degree of

Master of Science

Master's degree programme: Geospatial Technologies

submitted to

Graz University of Technology

Supervisor

Univ.-Prof. Dr.rer.nat. Dipl.-Forstwirt, Mathias Schardt

Institute of Geodesy

Graz, November 2019

AFFIDAVIT

I declare that I have authored this thesis independently, that I have not used other than the declared sources/resources, and that I have explicitly indicated all material which has been quoted either literally or by content from the sources used. The text document uploaded to TUGRAZonline is identical to the present master‘s thesis.

Date

Signature

Abstract

Climate models provide important input for political decision-making concerning the future challenges of climate change. The land component in those models is a major driver in Earth's climate system, therefore information about land surfaces is crucial for the successful application of the models. Often, biogeophysical parameters, which are used to describe the processes on land surfaces, are set statically within the land component. Remote sensing is a convenient tool to provide data of land surfaces, covering large areas repeatedly in a relatively short amount of time. The aim of this thesis is to provide dynamic information on three biogeophysical parameters - Albedo, Fraction of Vegetation Cover, Leaf Area Index - by the means of optical remote sensing techniques based on ESA's freely available Sentinel-2 imagery. The spatial and temporal resolution of the Sentinel-2 sensors make their data a suitable candidate to deliver input for deriving dynamics of biogeophysical parameters. From literature, appropriate methods for deriving the three parameters are chosen and applied to the Sentinel-2 data. With different datasets on ground cover and reference data containing non-remote sensing based measurements of the parameters, the results are analysed regarding their validity and plausibility. The tests show that the obtained results are overall plausible and within the expected range. However, limitations regarding the reference data have to be considered when analysing the results. Ground truth measurements of the investigated parameters in the study area, ideally synchronised with the overfly time of the satellite, which provides the imagery, would be necessary to evaluate the results more accurately.

Kurzfassung

Klimamodelle leisten einen wichtigen Beitrag im politischen Entscheidungsprozess, vor allem in Hinblick auf die zukünftigen Herausforderungen des Klimawandels. Das Landmodul in Klimamodellen stellt einen der Hauptantriebskomponenten des Klimasystems der Erde dar. Deswegen sind Informationen über die Landoberfläche essentiell für eine erfolgreiche Anwendung dieser Modelle. Oftmals werden die biogeophysikalischen Parameter, welche die Prozesse auf der Landoberfläche beschreiben, als statischer Input im Landmodul festgelegt. Fernerkundung ist ein geeignetes Werkzeug, um großflächige Daten einfach und in kurzer Zeit zur Verfügung zu stellen. Ziel dieser Arbeit ist es, die Dynamik von drei biogeophysikalischen Parametern - Albedo, Fraction of Vegetation Cover, Leaf Area Index - mit Hilfe von optischen Fernerkundungsmethoden aus Sentinel-2 Bilddaten abzuleiten. Durch die geometrische und zeitliche Auflösung der Sentinel-2 Daten eignen sie sich besonders gut zur Ableitung der Dynamik dieser drei Parameter. Aus der Literatur werden passende Methoden zur Bestimmung der Parameter ausgewählt und auf die Sentinel-2 Daten angewandt. Mittels verschiedener Referenzdatensätze aus terrestrischen Parametermessungen und Daten zur Bodenbedeckung werden die Ergebnisse hinsichtlich ihrer Validität und Plausibilität analysiert. Aus den Ergebnissen lässt sich auf eine allgemeine Gültigkeit innerhalb des erwarteten Bereiches schließen. Einschränkungen bezüglich der Referenzdaten sind jedoch bei der Auswertung der Ergebnisse zu beachten. Ground Truth Messungen zu den drei Parametern innerhalb des Untersuchungsgebietes und idealerweise zeitnah zu den Aufnahmezeitpunkten der verwendeten Fernerkundungsdaten sind für eine genauere Evaluierung der Ergebnisse unbedingt erforderlich.

Contents

List of Figures

List of Tables

1 Introduction

1.1 Remote Sensing of Surface Variables

Remote sensing is a useful tool to provide data on the physical characteristics of land surfaces. As opposed to ground measurements or field campaigns, it can produce data at a much higher temporal resolution and spatial coverage (Dorigo et al., 2007) and can therefore deliver vital input for different climate and weather models on various scales (e.g. Jiménez-Muñoz, J. A. Sobrino, Plaza, et al., 2009).
Modern day coupled climate models consist of different components to project the effects of Earth's climate drivers in the best possible way: atmosphere, ocean, land, and sea ice (Gent, 2013). The land component of these models provides important information on transfers of water and energy fluxes to the atmosphere (Zeng et al., 2000). Biogeophysical variables, such as albedo or the Leaf Area Index, are measurable quantities, which „*validate, calibrate and drive these [...] global and regional models at various scales*“ (S. Liang, 2007).
The main approaches for the remote sensing of biogeophysical variables are usually classified into two groups: statistical and physical techniques (e.g. Dorigo et al., 2007; S. Liang, 2007). The former is mostly expressed by regression functions, derived from an empirical relationship between biogeophysical variables and remote sensing observations, such as a vegetation index (S. Liang, 2007). The latter uses cause-effect relationships based on physical laws, mainly through the means of radiative transfer models (Verrelst et al., 2015). Both of these approaches will be discussed in the state of the art chapter.
Retrieving biogeophysical variables from remote sensing data can improve climate models, as they can better describe the temporal dynamics of vegetation (Brovkin et al., 2013; Wegehenkel, 2009). Many studies have reported enhancements of results when directly comparing the use of dynamic vegetation over static vegetation models (e.g. Wegehenkel, 2009; Stauffer et al., 2007; Strengers

et al., 2010), and using dynamic vegetation models in climate modelling has become state of the art (Brovkin et al., 2013). This thesis originally emerged from a cooperation between Joanneum Research and Wegener Center for Climate and Global Change, with the aim of providing dynamic biogeophysical parameter input for Wegener Center's used CALMET model, which will be described shortly in the subsequent chapter.

1.2 The CALMET Model input parameters

The California Meteorological Model (CALMET) is a diagnostic model with a wind field generator, which is used to contribute to dispersion models (models, which mathematically describe the distribution of air pollutants in the atmosphere), like CALPUFF (California Puff Model) (Scire et al., 2000; W. Wang et al., 2008). To simulate wind fields, CALMET requires different input datasets such as surface meteorological data and geophysical data. Next to the obligatory geophysical data of gridded fields of terrain elevation and land use categories, six biogeophysical parameters are listed as optional input:

- Albedo
- Anthropogenic Heat Flux
- Bowen Ratio
- Leaf Area Index
- Soil Heat Flux
- Surface Roughness Length

Additionally, in agreement with Wegener Center, another biogeophysical variable, the Fraction of Vegetation Cover, is chosen to be added to the list of parameters, to provide further input for their models.
In the default settings of CALMET, its biogeophysical parameters are set statically depending on the land use category. A static value is assigned to each class in the deployed land use classification without spatial or temporal variations. However, the model also allows for gridded field input at this place (Scire et al., 2000). The aim of this thesis is, to provide dynamic information of the listed variables, through the means of remote sensing technology. After initial research, only two out of the six CALMET parameters defined in the default settings proved to be suitable candidates for a solely optical remote

sensing based approach. The remaining four cannot be derived exclusively from optical remote sensing data, but require additional input data. Anthropogenic Heat Flux, the „*heat generated from human energy use [...]* “ (Flanner, 2009), has been reported to be derived based on country-specific data of energy consumption (Flanner, 2009). The Bowen Ratio, expressing the heat transfer for a surface through the ratio of sensible heating to latent heating (Perez, Castellvi, and Martínez-Cob, 2008), and the Soil Heat Flux, which describes „*the amount of thermal energy that moves through an area of soil in a unit of time [...]* “ (Sauer and Horton, 2005), both depend upon surface temperature data. Surface Roughness Length, „*[...] defined as the height above the surface at which the horizontal component of the wind speed approaches zero [...]* “ (Nicholas and Lewis, 1980), requires, for example, LiDAR data, to be derived through remote sensing techniques (Tian et al., 2011). Therefore, the following three parameters will be investigated in this thesis:

- Albedo
- Fraction of Vegetation Cover
- Leaf Area Index

The definition of these biogeophysical variables and their state of the art remote sensing based retrieval techniques, as well as their application to this work will be presented and discussed in depth in the following chapters.

1.3 Study Objectives

As stated in the previous chapters, this thesis aims to provide dynamic information on three biogeophysical parameters through the course of a year by the means of optical remote sensing techniques. Hence, two main objectives arise from this task:

1. Finding techniques based on optical remote sensing for the retrieval of each of the three parameters, which are applicable to the used Sentinel-2 data
2. Verifying the plausibility of the obtained results and thus, analysing the applicability of techniques to this thesis' study area and sensor data

1 Introduction

The used remote sensing data basis comprises freely available Sentinel-2A multi-temporal satellite imagery from 2016. To best capture the dynamic of the parameters through the course of a year, one scene per month is acquired for processing. In order to find applicable techniques for retrieving the investigated variables, an extensive literature review on the state of the art methods of each parameter is conducted. Once, the suitable approaches are selected, they are applied to the data. The results will be analysed regarding their plausibility through a comparison of in situ measurements for different cover types, gained through non-remote sensing methods found in literature.

2 State of the Art in Remote Sensing derived Surface Variables

This literature review will discuss state of the art remote sensing techniques of the three investigated parameters: Albedo, Fraction of Vegetation Cover, and Leaf Area Index. Each subchapter will give a definition of the parameter and its role and significance in (climate) modelling, as well as looking into methods currently used to retrieve the discussed parameters by means of remote sensing technology. Depending on their applicability to the study area and input data the methods to be applied to the data will be selected (see chapter 5).

2.1 Albedo

The albedo of a surface is defined as "*the ratio between the up-welling and down-welling incident irradiance upon a surface*" (Mattar et al., 2014). In other words, surface albedo is the fraction of incident sunlight, which is reflected by the surface (Coakley, 2003). Theoretically, the albedo of a surface can reach values between 0 (complete absorption) and 1 (complete reflection) (*Deutsches Zentrum für Luft- und Raumfahrt* 2019).
In literature different or often interchangeable terms for albedo are in use, e.g. surface albedo, broadband albedo, or white-sky albedo, to name only a few. Often, explanations and clear definitions of the used terms are missing. Schaepman-Strub et al., 2006 dedicated a publication to identify this terminology misuse and ambiguous nomenclature of reflectance quantities in optical remote sensing. Their paper uses the nomenclature for reflectance properties

introduced by Nicodemus et al., 1977 and aims to give "*an extensive physical and mathematical description of different reflectance quantities and separate conceptual from measurable quantities*" (Schaepman-Strub et al., 2006).

The concept of reflectance quantities is based on the Bidirectional Reflectance Distribution Function (BRDF), which describes the "*scattering of a parallel beam of incident light from one direction in the hemisphere into another direction in the hemisphere*". The quantity most often called albedo is the Bihemispherical Reflectance (BHR). It is the "*ratio of the radiant flux reflected from a unit surface area into the whole hemisphere to the incident radiant flux of hemispherical angular extent*" (Schaepman-Strub et al., 2006). This is a more precise definition of the one stated at the beginning of this chapter (by Mattar et al., 2014). Following this definition, the authors recommend to always include the illumination geometry when describing albedo from remotely sensed data. Schaepman-Strub et al., 2006 criticise this lack of standardisation when using terminology connected to the terms *reflectance* and *albedo* and the resulting source of error in albedo products. They also give many further definitions and examples on different terms of albedo, which will not be discussed in depth here.

Surface albedo should not be confused with surface reflectance, which is defined in the same way as surface albedo, but only from a single incident angle. Consequently, the albedo of a surface is the integration of reflectance over all sun-view geometrics (Mattar et al., 2014; Pinty and Verstraete, 1992). Despite this fact, many studies assume that surfaces are Lambertian, meaning that the radiance intensity is distributed circularly, for the sake of simplification. That would mean in turn, that surface reflectance equals surface albedo (Mattar et al., 2014). Land surfaces, however, are highly anisotropic and the spectral and angular distribution of incident light determines surface reflectance and consequently surface albedo (Coakley, 2003).

It is crucial to understand, that albedo is not an intrinsic property of a surface (Coakley, 2003) but depending on different factors. The solar zenith angle, the topography of the surface, and atmospheric conditions like precipitation, dew, frost or snow cover, wind, or water-vapour content can have an influence on albedo measurements. Structural properties of vegetation canopies, like shadowing, or the contrast between soil and vegetation depending on their humidity or dryness can change the albedo of a surface within a few hours. Therefore, surface albedo shows strong spatial and temporal variability (S. Wang and Davidson, 2007; Román et al., 2009; Cescatti et al., 2012; Ollinger et al., 2008).

Many publications account surface albedo as a key parameter in the Earth's climate and surface energy balance, as it is an essential variable in controlling the planetary radiative energy budget, estimating Earth's net radiation, determining energy fluxes in the atmosphere, as well as affecting the surface temperature and boundary-layer structure of the atmosphere (Mattar et al., 2014; Cescatti et al., 2012; Coakley, 2003; Silva et al., 2016; Lukeš et al., 2014; Souza, Ceballos, and Silva, 2014; S. Wang and Davidson, 2007; Rautiainen, Stenberg, et al., 2011). Albedo has an influence on surface temperature, cloud formation and precipitation, evaporation and transpiration, photosynthesis and many other processes in the planetary boundary layer (Sellers, Hall, et al., 1997; S. Wang and Davidson, 2007; Mattar et al., 2014; Silva et al., 2016). Accurate knowledge and monitoring of surface albedo and changes in surface albedo are important, as they can be an indicator for the extent of snow cover, phenology and the state and extent of vegetation, flooding, or drought (Mattar et al., 2014; Román et al., 2009; Cescatti et al., 2012; Coakley, 2003; S. Wang and Davidson, 2007). Hence, albedo is a fundamental input parameter of many global as well as regional climate models and weather forecast models (S. Liang et al., 2003; Mattar et al., 2014; S. Wang and Davidson, 2007).
The Global Climate Observing System (GCOS) lists albedo among the Essential Climate Variables (ECV), a set of key components needed to monitor Earth's climate change (GCOS, 2019). Nevertheless, surface albedo remains one the main uncertainties in current climate modelling (S. Liang, 2000; Lukeš et al., 2014; Kuusinen et al., 2014; Mattar et al., 2014; Burakowski et al., 2015).

For the remote sensing of albedo, the technical literature provides different approaches, which are mostly based on Radiative Transfer Models (RTMs). A beam of radiation is affected by absorption, emission, and scattering. This physical process is referred to as radiative transfer and Radiative Transfer Models are used to calculate and predict these processes (NASA, 2019). As most of the optical remote sensors measure reflectance only from one viewing angle, and albedo is the integration of reflectance over all sun-view geometrics (Mattar et al., 2014; Pinty and Verstraete, 1992) as stated previously, models mostly based on the BRDF have to be applied, to account for this. BRDF, however, cannot be measured directly (Nicodemus et al., 1977), therefore albedo "*products should only be considered as approximations [...], a fact often neglected*" (Schaepman-Strub et al., 2006).

Many publications, which focus on the application of albedo in modelling (e.g. Cescatti et al., 2012; Román et al., 2009; Lukeš et al., 2014) use the MODIS albedo product. This global land surface product with a spatial resolution of 500 m is acquired by the satellites Terra and Aqua over a period of 16 days making the product available every eight days due to the MODIS double repeat cycle. It contains both the white-sky and black-sky albedo (for definitions, see Schaepman-Strub et al., 2006) for MODIS bands 1 to 7 as well as for three broad bands (MODIS, 2019). The *RossThickLiSparseReciprocal BRDF model* is used to model albedo. This model provides three weighting parameters for each spectral band of MODIS that best describe the anisotropy of each pixel (MODIS, 2019).
A widely cited and used technique for the remote sensing of albedo was proposed by S. Liang, 2000. He introduces formulas to convert top-of-atmosphere (TOA) reflectance measurements of several narrow-band satellites (including Landsat ETM+, ASTER, AVHRR, MODIS and others) to average land surface broadband albedos. Based on MODTRAN (*MODerate resolution atmospheric TRANsmission*, a Radiative Transfer Model) simulations under different atmospheric and surface conditions, linear combinations of the different bands of each satellite are given, to calculate shortwave, visible, NIR, direct, and diffuse albedos. S. Liang, 2000 found the coefficients for ETM+ to be equally suitable for its predecessor Landsat TM. A study by Gratton, Howarth, and Marceau, 1993 proposes different weighting functions for Landsat TM and ETM+ bands based on different land cover types to calculate albedo. The use of other RTMs to obtain albedo was also proposed by Tasumi, Allen, and Trezza, 2008 or Rautiainen, Stenberg, et al., 2011.

2.2 Fraction of Vegetation Cover

The Fraction of Vegetation Cover [...] corresponds to the fraction of ground covered by green vegetation. Practically, it quantifies the spatial extent of the vegetation (Copernicus, 2018). In literature, Fraction of Vegetation Cover is also referred to as Vegetation (Covered) Fraction or Fractional (Green) Vegetation Cover and abbreviated as VF or FVC (sometimes FCover) respectively (Gitelson, Kaufman, et al., 2002; Jiménez-Muñoz, J. A. Sobrino, Plaza, et al.,

2009). In this thesis the abbreviation FVC will be used.
As a fraction of an area, the FVC can assume values between 0 and 1 or 0% and 100% (Gitelson, Kaufman, et al., 2002). FVC quantifies the spatial distribution of vegetation and is therefore an important indicator for the interaction between land, atmosphere, and hydrosphere (Gitelson, Kaufman, et al., 2002; Y. Li, H. Wang, and X.-B. Li, 2015; Salimi-Kouchi et al., 2013). Subsequently, it is an essential input parameter to simulate surface processes in the land component for numerical weather models as well as global and regional climate models (Jiménez-Muñoz, J. A. Sobrino, Plaza, et al., 2009; Barlage and Zeng, 2004; Gutman and Ignatov, 1998). The parameter is also used for the evaluation of land degradation and desertification, and is a controlling factor in the mathematical soil erosion models of the *universal soil loss equation* (USLE) and the *revised universal soil loss equation* (RUSLE) (Sellers, Los, et al., 1996; G. Wang et al., 2002; Y. Li, H. Wang, and X.-B. Li, 2015). FVC can further be applied in thermal remote sensing for surface emissivity estimation. (J. Sobrino et al., 2008; Jiménez-Muñoz, J. A. Sobrino, Plaza, et al., 2009)

In literature the two most commonly applied approaches for remote sensing of Fraction of Vegetation Cover are Spectral Mixture Analysis (SMA) and, as a special case of SMA, regression-based models with various Vegetation Indices (VI) (e.g. Jiménez-Muñoz, J. A. Sobrino, Plaza, et al., 2009; Gitelson, Kaufman, et al., 2002; Johnson, Tateishi, and Kobayashi, 2012; Y. Li, H. Wang, and X.-B. Li, 2015). Other, more sophisticated, approaches include inversion of RTMs (see for example Jiménez-Muñoz, J. A. Sobrino, Guanter, et al., 2005) and Artificial Neural Networks (see for example Baret et al., 1995, as cited in Jiménez-Muñoz, J. A. Sobrino, Plaza, et al., 2009). However, these approaches will not be further discussed in this thesis.
As a result of the spatial resolution of many remote sensing platforms, pixels in the acquired images are a composite of more than one individual substance, so-called mixed pixels. Spectral unmixing tries to disperse the spectrum of a pixel into a compilation of basic reflectance and its respective fractions in the pixel, also called *endmembers* and *abundances* respectively (Keshava and Mustard, 2002; Somers et al., 2011).
SMA can be conducted using a linear or a non-linear model, with the linear approach being the most commonly applied in remote sensing applications (Keshava and Mustard, 2002; Somers et al., 2011; Buyantuyev, J. Wu, and Gries, 2007; Jiménez-Muñoz, J. A. Sobrino, Plaza, et al., 2009; Johnson, Tateishi, and Kobayashi, 2012). Linear unmixing models assume, that one pixel is composed

of a linear combination of the endmembers, weighted by their fractional cover at the subpixel level (Somers et al., 2011; Y. Li, H. Wang, and X.-B. Li, 2015; Keshava and Mustard, 2002; Settle and Drake, 1993). Selecting the endmembers is a key step in SMA (Keshava and Mustard, 2002).
When selecting endmembers for the SMA, two aspects need to be considered. Firstly, the endmembers need to be distinguishable spectrally - mathematically speaking, the endmembers should be linearly independent. Secondly, the number of endmembers should be kept as small as possible. Too many, spectrally too similar endmembers lead to inaccurate fraction estimations (Adams and Gillespie, 2006, as cited in Somers et al., 2011). Another issue to take into account is the spatial and temporal variability of endmembers. The use of fixed endmembers throughout a scene, though easy to implement, cannot account for spatial variations in landscapes and temporal variations in time series due to different illumination conditions or season changes (Somers et al., 2011; Johnson, Tateishi, and Kobayashi, 2012; Keshava and Mustard, 2002; Jiménez-Muñoz, J. A. Sobrino, Plaza, et al., 2009). Therefore, Johnson, Tateishi, and Kobayashi, 2012 propose the application of spatially interpolated endmembers, using Ordinary Kriging and Inverse Distance Weighting to further improve FVC estimates as opposed to using fixed endmembers. Somers et al., 2011 list five basic principles to address endmember variability and minimise errors in SMA.
There are several techniques proposed in literature to extract endmembers, ranging from field-based methods (with Land Use Maps or field knowledge) (Jiménez-Muñoz, J. A. Sobrino, Plaza, et al., 2009; Somers et al., 2011) to semi-automated methods (Pixel Purity Index (Boardman et al., 1995, as cited in Somers et al., 2011; Jiménez-Muñoz, J. A. Sobrino, Plaza, et al., 2009)) and fully automated algorithms (Adams and Gillispie, 1993 or Tompkins et. al, 1997, both as cited in Keshava and Mustard, 2002).
If the mixed pixel is composed of reflectances, which are multiply scattered, like in mineral mixtures or sand grains, the spectral composition can no longer be treated as a linear combination, and non-linear unmixing techniques have to be applied (C. Wu and Murray, 2003; Keshava and Mustard, 2002). These include adding additional endmembers, using a training dataset to automatically calculate the mathematical relationship between the spectral data and the classes of interest (Somers et al., 2011) or more sophisticated models like Artificial Neural Networks or decision tree classifiers (see for example Somers et al., 2011). However, the use of non-linear unmixing approaches in remote sensing applications has not become a standard procedure yet (Somers et al., 2011; Keshava and Mustard, 2002). Many authors relate this to a lack

of in-depth understanding of this approach by most image analysts (Somers et al., 2011; Keshava and Mustard, 2002), even though many studies show the superior effects of non-linear models over linear models (Somers et al., 2011).

A special case of SMA are the mentioned regression-based approaches. Most of these studies work on the principle, that a correlation exists between Vegetation Indices and FVC and try to find a best-fit regression function between ground measurements of FVC and one or more VIs derived from remote sensing data (e.g. Jiménez-Muñoz, J. A. Sobrino, Plaza, et al., 2009; Jiang et al., 2006; Buyantuyev, J. Wu, and Gries, 2007; Barati et al., 2011; Kaspersen, Fensholt, and Drews, 2015; Z. Liang et al., 2008).
An equation widely used throughout most of the reviewed literature is the scaled VI function:

$$FVC = \frac{VI - VI_s}{VI_v - VI_s} \tag{2.1}$$

where VI_v represents the Vegetation Index at a fully vegetated pixel ($FVC = 1$) and VI_s of a bare soil pixel ($FVC = 0$) (Carlson and Ripley, 1997). In connection to SMA, VI_v and VI_s constitute the endmembers. While it is very easy to implement, some things have to be considered when using this scaling function.
First, a suitable Vegetation Index has to be chosen. A great number of authors (Carlson and Ripley, 1997; Gutman and Ignatov, 1998; Gitelson, Kaufman, et al., 2002; Jiang et al., 2006; Johnson, Tateishi, and Kobayashi, 2012; Jiménez-Muñoz, J. A. Sobrino, Plaza, et al., 2009; Barati et al., 2011; Buyantuyev, J. Wu, and Gries, 2007; Kaspersen, Fensholt, and Drews, 2015) uses the *Normalized Difference Vegetation Index*, NDVI, for deriving FVC with the formula 2.1. The NDVI is an easily computable and understandable, widely used index in remote sensing, which comes with certain limitations. In connection with the retrieval of FVC:

- NDVI of mixed pixels at medium to coarse spatial resolution cannot account for heterogeneous landscapes or canopy structures (Jiang et al., 2006; Buyantuyev, J. Wu, and Gries, 2007),
- NDVI has been shown to be insensitive to moderate to high chlorophyll content (Buschmann and Nagel, 1993, Gitelson and Merzlyak, 1994, both as cited in Carlson and Ripley, 1997), and

– NDVI varies strongly with variations in soil brightness (Liu and Huete, 1995, as cited in Carlson and Ripley, 1997).

All these limitations might affect the FVC results and need to be kept in mind whilst working with the NDVI. To avoid this, or improve FVC retrieval, a number of other indices have been proposed and tested by various studies. These include the *Soil-Adjusted Vegetation Index* (SAVI) and its derivatives, with the advantage of being less sensitive to soil brightness (Johnson, Tateishi, and Kobayashi, 2012; Kaspersen, Fensholt, and Drews, 2015; Buyantuyev, J. Wu, and Gries, 2007), the *Green Vegetation Index* (GVI) and the related *Variable Atmospherically Resistant Index* (VARI), to account for the saturation problem of NDVI at high chlorophyll levels (Gitelson, Kaufman, et al., 2002; Jiménez-Muñoz, J. A. Sobrino, Plaza, et al., 2009), or others like the *Simple Ratio* (SR) or the *Modified Triangulation Vegetation Index* (MTVI) (Barati et al., 2011). The choice of the index depends strongly on the area of applications. While Jiménez-Muñoz, J. A. Sobrino, Plaza, et al., 2009 were indicating, that the VARI, which uses the green band, delivered good results in their study area of agricultural, irrigated fields in Spain, Barati et al., 2011 stated, that indices using the green band are less suited for arid, sparsely vegetated areas, and Kaspersen, Fensholt, and Drews, 2015 found the SAVI to deliver the best results in urban areas.
Moreover, VI_v and VI_s need to be identified correctly, attributing to their regional and seasonal variability (Jiménez-Muñoz, J. A. Sobrino, Plaza, et al., 2009). Some authors suggest using the maximum and minimum of the used VI in the scene (e.g. Jiménez-Muñoz, J. A. Sobrino, Plaza, et al., 2009). When using the NDVI however, NDVI values can be negative, for example at water bodies, which might affect VI_s. Another proposed practise by Jiménez-Muñoz, J. A. Sobrino, Plaza, et al., 2009 is to use the NDVI histogram, which should show two peaks, if enough fully-vegetated and bare soil pixels exist throughout the scene. Also a combination of the histogram value for VI_s and the maximum value for VI_v were suggested in their study. Other propositions include the manual selection of a fully vegetated and a bare soil pixel through the aid of additional data or field knowledge (Johnson, Tateishi, and Kobayashi, 2012; Jiménez-Muñoz, J. A. Sobrino, Plaza, et al., 2009), the use of the ASTER spectral library (Jiménez-Muñoz, J. A. Sobrino, Plaza, et al., 2009), using global values for coarse spatial resolution as suggested by Gutman and Ignatov, 1998, or Spectral Mixture Analysis with two endmembers, full vegetation cover

and bare soil. The difference to SMA is the number of endmembers. While SMA needs as few endmembers as possible (Adams and Gillespie, 2006, as cited in Somers et al., 2011), regression-based approaches usually require a much larger dataset of reference values. An extensive study on advantages and disadvantages of using the above mentioned methods for determining VI_v and VI_s can be found at Jiménez-Muñoz, J. A. Sobrino, Plaza, et al., 2009, or Jiménez-Muñoz, J. A. Sobrino, Guanter, et al., 2005. It should be noted, that many studies, which use the method as described in equation 2.1, are not mentioning explicitly, how VI_v and VI_s were found.
Equation 2.1 describes a linear relationship, which could also be denoted as:

$$FVC = a \cdot VI - b; a = \frac{1}{VI_v - VI_s}, b = \frac{VI_s}{VI_v - VI_s}. \tag{2.2}$$

Carlson and Ripley, 1997 propose, that a quadratic relationship (of 2.2) improve results of FVC estimates, Wittich and Hansinng, 1995 (as cited in Wittich, 1997), however, show in their study, this is not the case. This further underlines the regional and seasonal variability of Vegetation Indices and FVC. Next to equation 2.1, other regression functions exist as well, as proposed for example by Gitelson, Kaufman, et al., 2002, the broad majority of reviewed studies, however, uses the scaled VI function.
Trying to find a regression function between remotely sensed VI and field measurements is a standard procedure in remote sensing. The method most commonly used for this is *Ordinary Least Squares* (OLS), which treats the VI as independent variables X and field measurements as dependent variable Y (Price and Bausch, 1995, Cohen et al., 2003, both as cited in Buyantuyev, J. Wu, and Gries, 2007; Turner et al., 1999). However, research shows, that using OLS in ecological and remote sensing applications (e.g. Fernandes and Leblanc, 2005, as cited in Buyantuyev, J. Wu, and Gries, 2007) might be questionable, because OLS assumes X as error-free, which is rarely the case in remote sensing studies due to measurement errors (Cohen et al., 2003, as cited in Buyantuyev, J. Wu, and Gries, 2007). To manage this, other approaches like *reduced major axis* (RMA) regression (Curran and Hay, 1986) or non-parametric estimators (Fernandes and Leblanc, 2005, as cited in Buyantuyev, J. Wu, and Gries, 2007) are proposed.

2.3 Leaf Area Index

The Leaf Area Index (abbreviated as LAI) was first introduced by Watson, 1947 (as cited in Jonckheere et al., 2004) as "*the total one-sided area of leaf tissue per unit ground surface area*". Since unit leaf area per unit ground area is measured, the LAI is a dimensionless variable. This definition applies well to plants with flat leaves as both sides of the leaf have the same surface area. For plants with rolled-up or wrinkled leaves, or with needles this definition, however, is problematic (Jonckheere et al., 2004). A definition formulated by Chen and Black, 1992 to account for plants with needles or non-flat leaves describes LAI as "*half the total leaf area per unit ground surface area*". Other authors introduced the LAI as the projected area of the plant leaf on the ground area (e.g. Gong and J. R. Miller, 1995; Turner et al., 1999; Q. Wang et al., 2005). Within this definition, the orientation of leaves in the canopy as well as the chosen projection angle influence the resulting LAI (Jonckheere et al., 2004; Chen and Cihlar, 1996; Weiss et al., 2004). Yet another distinction can be made between *green* LAI and *brown* LAI (Delegido, Verrelst, Rivera, et al., 2015; Pasqualotto et al., 2019). The green LAI represents „*the leaves which are photosynthetically active*" (Pasqualotto et al., 2019), whereas brown LAI comprises „*brown or senescent vegetation*" (Delegido, Verrelst, Rivera, et al., 2015). It should be noted that the chosen definition has a large influence on the obtained LAI results.

Values of LAI for any given area can range from 0, for bare ground or generally vegetation-free areas, up to the highest possible values depending on the cover type (Herrmann et al., 2011). Following the definition of LAI, it is dependent on the plant type, given the different leaf shapes of plants. The highest reported LAI values vary in publications, but are generally recorded in (boreal) coniferous forests (Jonckheere et al., 2004).

The Leaf Area Index is an important variable in many different biological, physical, and environmental processes. As a characteristic of canopy structure (Chason, Baldocchi, and Huston, 1991), it influences interception, absorption, and attenuation of light through the canopy (Baldocchi and Meyers, 1998; Reichenau et al., 2016; Tanaka et al., 2015; Viña et al., 2011), depending on angular and spatial distribution of foliage in the canopy (Chen and Cihlar, 1996). The leaves in a vegetation cover, and consequently LAI, control evapotranspiration, rainfall and fog interception (Delegido, Verrelst, Alonso, et al., 2011;

Herrmann et al., 2011; Schiffmann et al., 2008; Gong, Pu, et al., 2003; Viña et al., 2011; Zheng and Moskal, 2009) and is generally an important component of the hydrological cycle (Xavier and Vettorazzi, 2004). LAI is paramount for the estimation of energy and mass exchange processes between the land surface layer and the atmosphere layer, including CO_2 fluxes, carbon and nutrient cycles, carbon sequestration, or photosynthesis (Colombo et al., 2003; Clevers, Kooistra, and Brande, 2017; Frampton et al., 2013; González-Sanpedro et al., 2008; Richter, Hank, et al., 2012; Zheng and Moskal, 2009; Zhu et al., 2013).
The index is an important indicator for predicting productivity and biomass of forests (Pope and Treitz, 2013; Zheng and Moskal, 2009), and for describing the structure and functioning of vegetation cover to efficiently monitor changes and adjust management practices (Delegido, Verrelst, Alonso, et al., 2011; Clevers, Kooistra, and Brande, 2017; Schiffmann et al., 2008). LAI also plays a major role in the agricultural sector connected to precision farming (Richter, Hank, et al., 2012). It is used to monitor crop growth, predict yield, assess crop stress, or adapt crop management through irrigation or the application of fertilisers (Nguy-Robertson, Gitelson, et al., 2012; Haboudane et al., 2004; González-Sanpedro et al., 2008; Gong and J. R. Miller, 1995).
Based on its notable influence in all the above mentioned processes, LAI becomes a key input parameter in modelling climate, ecosystem productivity, global environmental change, or dynamic vegetation in land surface models (Chen and Cihlar, 1996; Colombo et al., 2003; Pope and Treitz, 2013; Jonckheere et al., 2004; Laurent et al., 2014; S. Liang et al., 2003). Therefore, timely and accurate measurements of LAI are crucial for the successful application of these models. Furthermore, remote sensing satellites can cover large areas in short periods of time, thus making their products an important and useful tool for the assessment of LAI.

Before discussing remote sensing methods of LAI, ground-based measurements will be described very shortly at this point, as they are an integral part of many publications concerning the remote determination of Leaf Area Index. Ground-based measurements of LAI can be conducted via destructive harvesting methods, collecting and weighing total litter fall, allometry (especially when measuring the LAI of trees), or indirect non-contact tools which use hemispherical photography and/or gap fraction estimates (like the LAI-2000 plant canopy analyzer). These techniques will not be discussed here but should

only be noted for the sake of completeness. Further information on them can be found for example at Jonckheere et al., 2004, Weiss et al., 2004, or Zheng and Moskal, 2009.
To measure Leaf Area Index by means of remote sensing, two main fields of application can be found in literature. The first approach is based on finding best-fit regression functions between spectral vegetation indices (SVIs) derived from remote sensing data and LAI values usually measured in-situ with ground-based methods. The second technique relies on the inversion of Radiative Transfer Models, which often also requires ground-based LAI measurements.
Establishing empirical relationships between LAI and SVIs is the most commonly applied technique to investigate the spatial and temporal distribution, as it is very simple, convenient and easy to implement, once the labour-intensive task of gathering sufficient reference data is completed (Colombo et al., 2003; Viña et al., 2011; Delegido, Verrelst, Alonso, et al., 2011; Frampton et al., 2013; Tanaka et al., 2015). As mentioned before, this is usually done with ground-based measurements of LAI. These are either obtained specifically for the study, to also match the passing time of the used remote sensing satellite over the chosen study area (e.g. Colombo et al., 2003, Viña et al., 2011, or Tanaka et al., 2015), or are taken from extensive field campaigns like SPARC or AgriSAR (e.g. Delegido, Verrelst, Alonso, et al., 2011, or Richter, Atzberger, et al., 2011), two campaigns supported by ESA (European Space Agency), to acquire data on various crops over a whole growing season (ESA, 2005; Hajnsek et al., 2007).
Studies have been carried out using different remote sensing platforms, including Landsat TM or ETM+ (Bach et al., 2003; Chen and Cihlar, 1996; Xavier and Vettorazzi, 2004; Schiffmann et al., 2008; Turner et al., 1999), IKONOS (Colombo et al., 2003), MODIS and SPOT (Turner et al., 1999), airborne hyperspectral CASI (Compact Airborne Spectrographic Imager) (Delegido, Verrelst, Alonso, et al., 2011; Haboudane et al., 2004; Gong and J. R. Miller, 1995), AISA (aircraft-mounted hyperspectral imaging spectroradiometer) (Viña et al., 2011; Nguy-Robertson, Gitelson, et al., 2012), and field spectrometers (Viña et al., 2011; Tanaka et al., 2015; Gong, Pu, et al., 2003; Nguy-Robertson, Peng, et al., 2014). To establish empirical relationships, a wide range of SVIs has been tested for deriving LAI from this remote sensing data. One of the most applied indices is the NDVI. It is easy to calculate and can be used to estimate the density of green vegetation on a surface (Weier and Herring, 2000). Many studies, however, came to the conclusion, that NDVI suffers from a saturation

effect at medium to high LAI values, meaning that with increasing LAI no more increase in NDVI can be measured (Haboudane et al., 2004; Tanaka et al., 2015; Reichenau et al., 2016; Q. Wang et al., 2005; González-Sanpedro et al., 2008). This is due to the high absorption coefficient of chlorophyll which makes the reflectance in the red region saturate and consequently also the NDVI (Nguy-Robertson, Gitelson, et al., 2012; Carlson and Ripley, 1997). The point at which this NDVI "insensitivity" comes into effect is dependent on the crop or plant type, but lies often at LAI values between 2 and 3 (González-Sanpedro et al., 2008; Carlson and Ripley, 1997). Also, NDVI has been shown to be very susceptible to canopy architecture, soil background and atmospheric effects (Nguy-Robertson, Gitelson, et al., 2012).
Other indices tested include the WDRVI (Wide Dynamic Range Vegetation Index) (Nguy-Robertson, Gitelson, et al., 2012; Nguy-Robertson, Peng, et al., 2014; Tanaka et al., 2015; Viña et al., 2011), which has been shown to be both, less sensitive (Nguy-Robertson, Gitelson, et al., 2012; Viña et al., 2011) and more sensitive to higher LAI values compared to NDVI (Tanaka et al., 2015). Nguy-Robertson, Peng, et al., 2014 showed in their study, that WDRVI derived from the green band is very reliable at predicting the LAI of maize, potato, and wheat but not soybean, whereas WDRVI derived from the red edge band has the highest potential for a unified formula for different crop types. Nguy-Robertson, Gitelson, et al., 2012 proposed to combine different SVIs according to their sensitivity along the entire range of LAI to achieve maximal sensitivity for a certain crop type. This also goes along with the findings of Q. Wang et al., 2005, who found a strong linear relationship between NDVI and LAI for the phenological stages of leaf production and leaf senescence but no clear relationship during the leaf-constant period. Other studies suggest to include hyperspectral data to gain more information than from SVIs, which are generally computed from two to three spectral bands (Richter, Hank, et al., 2012; S. Liang et al., 2003; Tanaka et al., 2015). Chlorophyll indices (Gitelson, Gritz, and Merzlyak, 2003, as cited in Viña et al., 2011) computed from the green or red edge band show a strong linear relationship with LAI and appear to be well suited also for higher LAI values, with the red edge Chlorophyll Index showing less sensitivity to crop type (Viña et al., 2011; Tanaka et al., 2015; Nguy-Robertson, Gitelson, et al., 2012; Nguy-Robertson, Peng, et al., 2014).

When reading the literature on empirical SVI-LAI relationships, it becomes clear that no universal formula exists. On the one hand this is strongly connected to the crop and plant type, or more generally speaking, the land cover type dependency of LAI (Haboudane et al., 2004; González-Sanpedro et al., 2008), although some indices have shown an insensitivity to crop type (e.g. Richter, Hank, et al., 2012; Viña et al., 2011). On the other hand, these empirical relationships were formed under certain atmospheric conditions, sensor configurations, and sensor-sun-target geometries and were developed for certain land cover types at a certain time in the year in a specific location. Applying these very site-specific relationships to other locations under different conditions cannot do justice to the spatial and temporal variability of LAI and might impose uncertainties to the obtained results (Reichenau et al., 2016; Delegido, Verrelst, Alonso, et al., 2011; Chason, Baldocchi, and Huston, 1991). It should also be noted, that most of the empirical relationships are established for green LAI only, and the methods fail for the leaf senescence stage of plants (Delegido, Verrelst, Rivera, et al., 2015).

The second, though less often applied approach for the retrieval of LAI through remote sensing data is the inversion of Radiative Transfer Models. The advantages of this method are the possibility to use the full spectrum of multi- or hyperspectral sensors, as well as the exploitation of directional signatures of multi-angle sensors (Richter, Atzberger, et al., 2011). However, the models are more complex to handle than simple empirical relationships and need considerable parametrisation (González-Sanpedro et al., 2008; Richter, Atzberger, et al., 2011). The inversion of the models presents an ill-posed and underdetermined problem (Laurent et al., 2014). Generally a lot of additional input data is needed, but different regularisation methods exist to overcome this problem. One inversion technique connected to remote sensing is the use of lookup tables (LUTs), which has been applied by Richter, Atzberger, et al., 2011; Richter, Hank, et al., 2012 or González-Sanpedro et al., 2008. Results by Richter, Atzberger, et al., 2011 also demonstrate the crop type dependency of LAI by suggesting to use crop specific RTMs. Other inversion techniques include Bayesian object-based estimations (Laurent et al., 2014), iterative optimisation (Jacquemoud et al., 1995, as cited in Richter, Atzberger, et al., 2011) or Artificial Neural Networks (Atzberger, 2004, as cited in Laurent et al., 2014). As RTMs will not be used in this work, the reader is referred to Myneni et al., 1997 or Jacquemoud et al., 1995 (as cited in Richter, Atzberger, et al., 2011) for further information.

3 Data Source

Chapter 3 summarises all necessary remote sensing and ancillary data, for the retrieval of the selected parameters as well as the in-situ and ancillary data used for the subsequent plausibility analyses of the derived results. Optical remote sensing data from the Sentinel-2A satellite are used as input to derive the parameter (chapter 3.1). In chapter 3.2, in-situ measurements found in literature are described, which will be used to compare the results derived from the satellite images to. In order to achieve this, information on ground cover is necessary, and chapter 3.3 contains the different sets of data on ground cover.

3.1 Input Data: Sentinel-2A

The Copernicus programme, formerly GMES, short for Global Monitoring for Environment and Security, is a joint programme by the European Commission and ESA with the aim to provide global, timely, and easily and free accessible information on land, climate change, and other application domains. ESA's satellite mission Sentinel, as a part of the GMES initiative, will contribute a set of observations, including C-band SAR, medium to high resolution thermal and optical data, and atmospheric chemistry observations. An overview of the Sentinel missions (realised and planned) is shown in table 3.1. Following the EU GMES Regulations, all data acquired from the Sentinel missions can be accessed by anybody for free. The first three Sentinel missions are based on a constellation of two satellites (referred to as A and B; for Sentinel-3 a third and fourth satellite are planned), circling the same sun-synchronous, near-polar orbit with a phase delay of 180°. This set-up allows for a high revisit time, thus leading to a higher temporal resolution (Fletcher, 2012; Aschbacher and Milagro-Pérez, 2012; Drusch et al., 2012; Berger et al., 2012; Malenovský et al., 2012; ESA, 2018a; ESA, 2018b). For this thesis Sentinel-2A data will be deployed.

Table 3.1: Overview of ESA's Sentinel Missions

Sentinel Mission	*Main application domain*
Sentinel-1	C-band SAR
Sentinel-2	high-resolution optical sensor
Sentinel-3	sea-surface topography
Sentinel-4	atmospheric monitoring
Sentinel-5P	air quality monitoring
Sentinel-5	air quality monitoring
Sentinel-6	radar altimeter to measure global sea-surface height

Source: Berger et al., 2012

The aim of the Sentinel-2 mission is to provide multi-spectral, high-spatial-resolution optical observations for several products and services, such as geophysical parameters, or mapping land-cover and land-change. The mission will complement SPOT- and Landsat-data and improve data availability for users (Aschbacher and Milagro-Pérez, 2012; Drusch et al., 2012; Suhet, 2015; Martimort et al., 2007). The most important characteristics of the Sentinel-2 mission are summarised in Table 3.2. Sentinel-2A was launched on 23rd June 2015 and Sentinel-2B followed on 7th March 2017.

Table 3.2: Mission features of the Sentinel-2 mission

Mission Features	*Data*
Satellite life time	7.25 yrs (consumables for 12 yrs)
Number of satellites	2
Nominal orbit	sun-synch. at 786 km (mean alt.)
Land coverage	56° S to 84° N
Global revisit time	5 days at equator
Spatial Resolution	10 m, 20 m, 60 m
Radiometric Resolution	12 bit (4096 grey values)
Swath width	290 km

Source: Drusch et al., 2012; Suhet, 2015

The MSI (MultiSpectral Instrument) of the Sentinel-2 satellites comprises 13 spectral bands, covering VNIR up to SWIR. Spatial resolution spans from 10 m (four bands in the visible and near infra-red spectrum), to 20 m (six bands in the vegetation red-edge and short wave infra-red spectrum), and up to 60 m (three bands for cloud screening and atmospheric corrections). The details on wave length of the individual spectral bands are shown in figure 3.1 (Main-Knorn, Pflug, Debaecker, et al., 2015; Martimort et al., 2007; Drusch et al., 2012; Suhet, 2015; Fletcher, 2012).

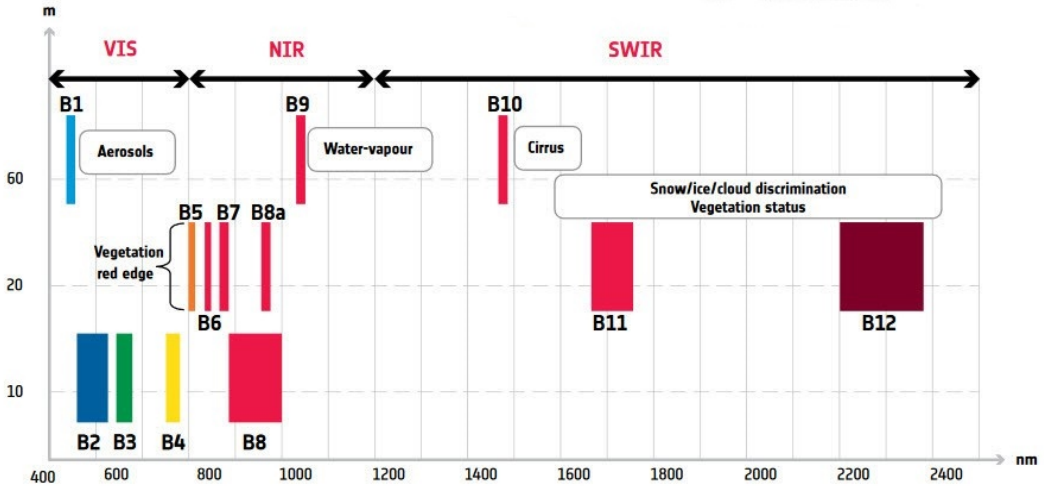

Figure 3.1: Wave length (x-axis) and spatial resolution (y-axis) of Sentinel-2's MSI

Source: ESA, 2015

Products from the acquired Sentinel-2 data are delivered in a compilation of granules, with a granule being "*the minimum indivisible partition of a product (containing all possible spectral bands)*" (Suhet, 2015). There are several levels in the processing steps of the products. Level-0 and Level-1A products comprise raw compressed and uncompressed data and are not available to the user. The Level-1B product comprises top of atmosphere (TOA) radiances in sensor geometry and is made available to users. Up to this processing level the granule size amounts to 25 km across track and 23 km along track. Level-1C provides the first ortho-rectified product. A Digital Elevation Model is used to project the image in UTM/WGS84 projection. This level also includes masks

for clouds (including cirrus clouds), and land/water, with a granule size of 100 km × 100 km. Up to this processing level, the products are systematically generated at the ground segment. Using the Sentinel-2 Toolbox Sen2Cor, users can derive the Level-2A product, which provides bottom of atmosphere (BOA) radiances, from the Level-1C. Additionally, an enhanced cloud mask and a more detailed scene classification are generated by the toolbox. Projection and granule size remain the same (Suhet, 2015; Fletcher, 2012; ESA, 2018a).
For this thesis, 13 scenes acquired between 7th January 2016 and 12th December 2016 by the Sentinel-2A satellite (see table 3.3), were downloaded as Level-1C products and further processed to Level-2A. Sentinel-2B scenes were not used in this thesis as they were not available yet for the investigated year of 2016. Due to cloud coverage, no scene from June 2016 was available.

Table 3.3: Source and acquisition dates of the used Sentinel-2A scenes

scene name of both granules	*scene index*	*date of scene*
$S2A\_USER\_PRD\_MSIL2A\_PDMC\_20160107T200822\_R122\_V20160107T101243\_20160107T101243\_T33TWM$ $S2A\_USER\_PRD\_MSIL2A\_PDMC\_20160107T200822\_R122\_V20160107T101243\_20160107T101243\_T33TWN$	scene 1	07.01.2016
$S2A\_USER\_PRD\_MSIL2A\_PDMC\_20160206T202544\_R122\_V20160206T100203\_20160206T100203\_T33TWM$ $S2A\_USER\_PRD\_MSIL2A\_PDMC\_20160206T202544\_R122\_V20160206T100203\_20160206T100203\_T33TWN$	scene 2	06.02.2016
$S2A\_USER\_PRD\_MSIL2A\_PDMC\_20160315T064850\_R079\_V20160314T095144\_20160314T095144\_T33TWM$ $S2A\_USER\_PRD\_MSIL2A\_PDMC\_20160315T064850\_R079\_V20160314T095144\_20160314T095144\_T33TWN$	scene 3	14.03.2016
$S2A\_USER\_PRD\_MSIL2A\_PDMC\_20160414T030145\_R079\_V20160413T095322\_20160413T095322\_T33TWM$ $S2A\_USER\_PRD\_MSIL2A\_PDMC\_20160414T030145\_R079\_V20160413T095322\_20160413T095322\_T33TWN$	scene 4	13.04.2016
$S2A\_USER\_PRD\_MSIL2A\_PDMC\_20160523T144152\_R079\_V20160523T095404\_20160523T095404\_T33TWM$ $S2A\_USER\_PRD\_MSIL2A\_PDMC\_20160523T144152\_R079\_V20160523T095404\_20160523T095404\_T33TWN$	scene 5	23.05.2016
$S2A\_USER\_PRD\_MSIL2A\_PDMC\_20160712T145235\_R079\_V20160712T095351\_20160712T095351\_T33TWM$ $S2A\_USER\_PRD\_MSIL2A\_PDMC\_20160712T145235\_R079\_V20160712T095351\_20160712T095351\_T33TWN$	scene 6	07.12.2016

Continued on next page

Table 3.3 – continued from previous page

scene name of both granules	*scene index*	*date of scene*
$S2A\_USER\_PRD\_MSIL2A\_PDMC\_20160806T083936\_R122\_V20160804T100613\_20160804T100613\_T33TWM$ $S2A\_USER\_PRD\_MSIL2A\_PDMC\_20160806T083936\_R122\_V20160804T100613\_20160804T100613\_T33TWN$	scene 7	04.08.2016
$S2A\_USER\_PRD\_MSIL2A\_PDMC\_20160901T191809\_R079\_V20160831T095032\_20160831T095217\_T33TWM$ $S2A\_USER\_PRD\_MSIL2A\_PDMC\_20160901T191809\_R079\_V20160831T095032\_20160831T095217\_T33TWN$	scene 8	31.08.2016
$S2A\_USER\_PRD\_MSIL2A\_PDMC\_20160925T050831\_R122\_V20160923T100022\_20160923T100625\_T33TWM$ $S2A\_USER\_PRD\_MSIL2A\_PDMC\_20160925T050831\_R122\_V20160923T100022\_20160923T100625\_T33TWN$	scene 9	23.09.2016
$S2A\_USER\_PRD\_MSIL2A\_PDMC\_20161014T032537\_R122\_V20161013T100022\_20161013T100022\_T33TWM$ $S2A\_USER\_PRD\_MSIL2A\_PDMC\_20161014T025554\_R122\_V20161013T100022\_20161013T100022\_T33TWN$	scene 10	13.10.2016
$S2A\_USER\_PRD\_MSIL2A\_PDMC\_20161023T235528\_R122\_V20161023T100052\_20161023T100052\_T33TWM$ $S2A\_USER\_PRD\_MSIL2A\_PDMC\_20161023T231042\_R122\_V20161023T100052\_20161023T100052\_T33TWN$	scene 11	23.10.2016
$S2A\_USER\_PRD\_MSIL2A\_PDMC\_20161129T183110\_R079\_V20161129T095342\_20161129T095342\_T33TWM$ $S2A\_USER\_PRD\_MSIL2A\_PDMC\_20161129T181730\_R079\_V20161129T095342\_20161129T095342\_T33TWN$	scene 12	29.11.2016
$S2A\_MSIL2A\_20161209T095402\_N0204\_R079\_T33TWM\_20161209T095503\_T33TWM$ $S2A\_MSIL2A\_20161209T095402\_N0204\_R079\_T33TWN\_20161209T095503\_T33TWN$	scene 13	09.12.2016

3.2 Reference Data

To validate the plausibility of remotely sensed parameters, reference data, gained through non remote sensing methods, is necessary. In their publication, Pielke and Avissar, 1990 summarise typical albedo ranges for different ground cover types, taken from various studies, which determined albedo with non-remote sensing techniques. For the Leaf Area Index, databases exist, which collected all publications on LAI field measurements for different plant or cover types. Scurlock, Asner, and Gower, 2001 published over 1000 records of measurements between 1932 and 2000, which include information on the location, time of measurement, used method, biome and dominant species, and more next to the LAI measurement. This database will be used for the plausibility analysis of crop-specific LAI (chapter 5.4.2). Similar to this database and issued by the same archive center (ORNL DAAC - the Oak Ridge National Library Distributed Active Archive Center for biogeochemical dynamics), a database specifically for woody plants was published by Iio and Ito, 2014, compiling over 1000 field-observed measurements between 1932 and 2011, which will be used for the validation of forest-specific LAI.

3.3 Ground Cover Data

Different sets on ground cover data will be applied in this thesis to validate the plausibility of results, depending on the investigated parameter. For albedo, Copernicus' Urban Atlas classification will be used. Leaf Area Index results will be analysed using information on the ground covers *crop type* and *forest type*. The investigated crop types are *maize* and *wheat* and forest type describes either *coniferous forest* or *deciduous forest*. Both datasets are provided by Joanneum Research. A soil sealing map, provided by the city of Graz, will form the basis of Fraction of Vegetation Cover plausibility tests.

3.3.1 Copernicus land monitoring services: Urban Atlas classification

The European monitoring system Copernicus collects and provides data in the areas land, marine, atmosphere, climate change, emergency management, and security. In this thesis the freely available Urban Atlas product is downloaded and processed further to use for the plausibility analyses of the parameter results (Copernicus, 2019a).
The Urban Atlas product is available for the years 2006 and 2012 as vector data derived from data at a spatial resolution of 20 m. Considering the date of the satellite images (2016), the Urban Atlas data for 2012 is downloaded from the Copernicus Website for the urban region of Graz (see figure 3.2). Of the delivered 27 classes in the Urban Atlas layer only those classes are used for the plausibility analyses, where literature provided information on parameter value ranges gained through non-remote sensing methods (Copernicus, 2019b). These are:

- 11100: Continuous Urban fabric (Sealing Level (S.L.)) >80%), 11210: Discontinuous Dense Urban Fabric (S.L.: 50% - 80%), 11220: Discontinuous Medium Density Urban Fabric (S.L.: 30% - 50%, 11230: Discontinuous Low Density Urban Fabric (S.L.: 10% - 30%) all combined to one class *urban*
- 21000: Arable land (annual crops)
- 23000: Pastures
- 50000: Water

The class 31000: Forests is not used, as information on that ground cover is taken from the LiDAR-based forest classification (see 3.3.3).

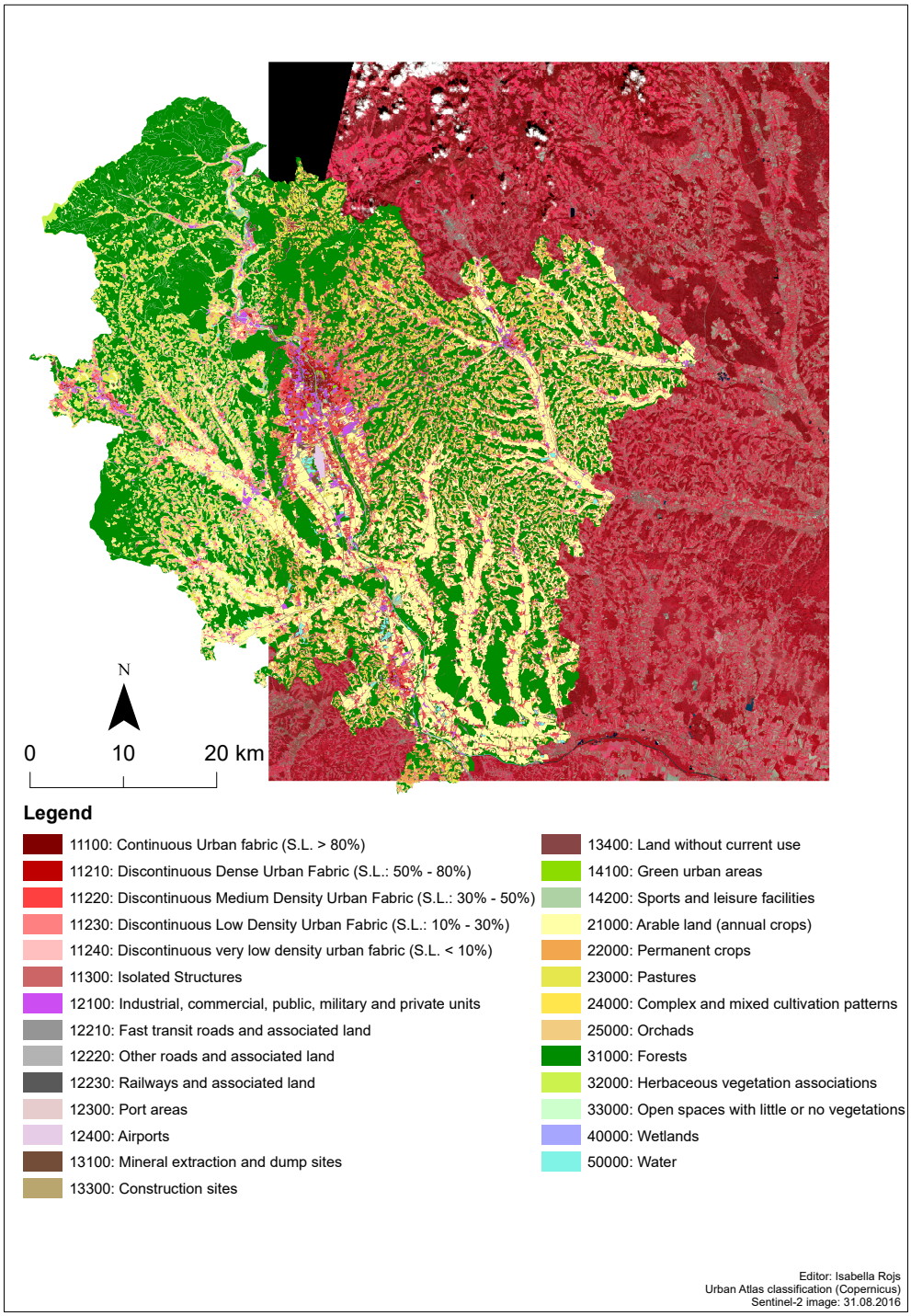

Figure 3.2: Copernicus Urban Atlas Layer of Graz with Sentinel-2 scene in background

Source: Copernicus, 2019b

3.3.2 Ground truth data for crop types

In-situ measurements from summer and autumn 2016 of several crop types located in the used study area were made available by Joanneum Research as a shapefile. The shapefile includes information on the crop type (e.g. maize or wheat) and the observation date of a polygon, among other attributes. The crop type information is necessary to validate the remote sensing data-based LAI calculations by means of comparing the results to crop-type specific LAI values gained through non-remote sensing based methods. From this rasterised dataset, information on the crop type of a pixel will be used for the plausibility analysis of the crop-specific LAI calculations (see chapter 5.5.3).

3.3.3 LiDAR-based forest variables

Next to ground truth data on crop types, forest classification data from 2015 has also been provided by Joanneum Research. For the project on Indicative Hazard Maps for Styria, aerial images with a spatial resolution of 20 cm and a Digital Terrain and Surface Model with a spatial resolution of 50 cm were used to create a forest mask of Styria as a basic product. Subsequently, more than six million homogeneous entities were formed using a segmentation algorithm. For each segment several forest parameters were derived, such as age class (ranging from culture to old forest), crown closure (in %), timber volume, or mean and upper tree height. Satellite remote sensing data from IRS (Indian Remote Sensing Programme) were used to determine the percentage of coniferous and deciduous for each of the segments. The outcome of this processing step is an Esri shapefile (Bauer et al., 2015).
For this thesis LAI calculations for coniferous and deciduous forest were tested separately. Segments with a coniferous ratio greater or equal 75% were exported into a shapefile representing coniferous forest, and segments with a coniferous ratio less than 25% were exported into a shapefile representing deciduous forest. Similar to crop types, LAI values for coniferous and deciduous forest from literature are used to validate the calculations and the LiDAR forest map provides the ground cover data basis for these plausibility tests.

3.3.4 Sealing Map

The city of Graz provided a shapefile containing information on soil sealing, which is needed to validate the results of Fraction of Vegetation Cover. Figure 3.3 shows all the sealed areas in the provided sealing data in grey. The extract in the lower left corner of the figure shows a part of the city at a smaller scale and illustrates, that buildings are not included in this data set. This fact needs to be considered when preparing the dataset for the validation. For the validation of FVC, information about the fraction of soil sealing per pixel is necessary, as it is assumed, that FVC and soil sealing complement each other to 100% (FVC [%] = 100 - fraction of sealed soil [%]) (Kaspersen, Fensholt, and Drews, 2015). The further processing steps of deriving fraction of soil sealing per pixel from this dataset are described in chapter 5.5.2.

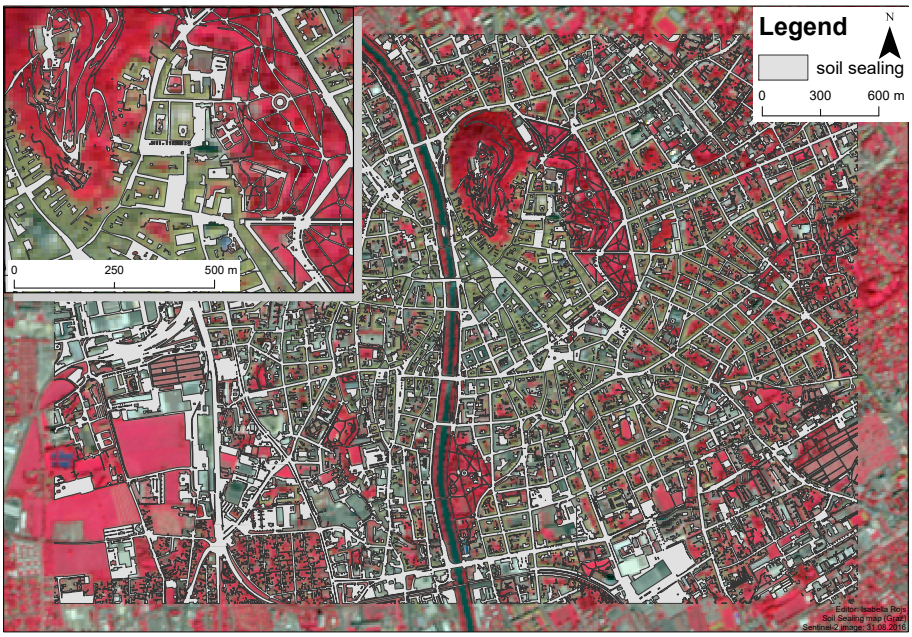

Figure 3.3: Soil sealing map of the (inner) city of Graz

Source: own illustration, data by Graz, 2019

4 Study Area

The study area is located in the southern foreland of the Eastern Alps. It spans from the Schöckl in the north west to Murska Sobota, Slovenia, in the south east. Figure 4.1 illustrates it's location in the foreland. The extent of the study area is defined by a bounding box around two study regions of the Wegener Center: the Raabtal Region (RTR) and South-East Styria (SES) (Kirchengast, 2018) (see figure 4.1). With a size of 4620 km^2 it contains approximately 130 Styrian municipalities and also covers small parts of western Burgenland and northern Slovenia. The biggest settlement in the study area is the city of Graz; other larger settlements include Weiz, Hartberg, Fürstenfeld, Feldbach and Leibnitz.

According to the *Gebietsgliederung* by Lieb, 1991 (adaptation depicted in figure 4.2), Styria can be divided into two superordinate entities, based on geological and geomorphological features: the alpine and the non-alpine region. At an altitude of 1445 m, the Schöckl and it's immediate surroundings are included in the alpine region while the greater part of the study area counts among the non-alpine region. This part, the foreland, is characterised by the valley floors of the rivers Mur and Raab, and elongated ridges, so-called *Riedel*, which are eponymous for the *East Styrian Riedelland*. (Kabas, 2012; Lieb, 1991)
The *Klimaatlas Steiermark* defines the homonymous climate region foreland (German: *Vorland*), which can be further divided into subcategories. Valley floors in this region are affected by continental climate conditions, effecting in warm summers and relatively cold winters. Additionally, in winter, fog and atmospheric inversion are abundant in this region, thus preventing outflow of cold ground air, which further intensifies the effect and leading to problems with air pollution. Higher located ridges are less afflicted by these circumstances, leading to milder winters with less frost risk, compared to the valley floors. The foreland is prone to thunderstorms and hail in summer, which in return are

more frequent and intense on the ridges than in the valleys. (Wakonigg and Podesser, 2018; Wakonigg, 1978; Wakonigg, 1967)
Monthly mean temperatures in January vary from −4 °C to −1 °C and in July from 17 °C to 19.5 °C. The annual mean varies between 7.5 °C and 8.7 °C, depending on the specific location. The annual precipitation amounts to approximately 800 mm, with most of the precipitation accumulating in summer due to convective rainfalls. (Wakonigg and Podesser, 2018; Wakonigg, 1978)
The IPCC Report of 2007 presented a global temperature rise of 0.76 °C (±0.19 °C within a 95 % confidence interval) between 1850 and 2001 (Solomon et al., 2007). For Europe the temperature rise amounts to 0.8 °C (±0.3 °C) with a high regional variability (Luterbacher et al., 2004). Many studies prove, that the Alpine region shows a very high sensitivity to changing climate conditions (Climate Change (APCC), 2014). The study *Austrian long-term climate* (ALOCLIM) by Auer, Böhm, and Schöner, 2001 evaluated annual mean temperatures between 1890 and 1999 of 56 sites in and close to Austria. The sites were split into two groups, high-level and low-level regions, depending on their altitude. The results show a linear trend of 1.28 °C for high-level regions and 1.22 °C for low-level regions. Both values lie well above the 0.8 °C for Europe (Luterbacher et al., 2004), demonstrating the importance of considering regional variability when talking about temperature rise. For precipitation, ALOCLIM results reflect the high variability of these events with a slight decreasing trend for eastern and southern Austria (Auer, Böhm, and Schöner, 2001; Climate Change (APCC), 2014).

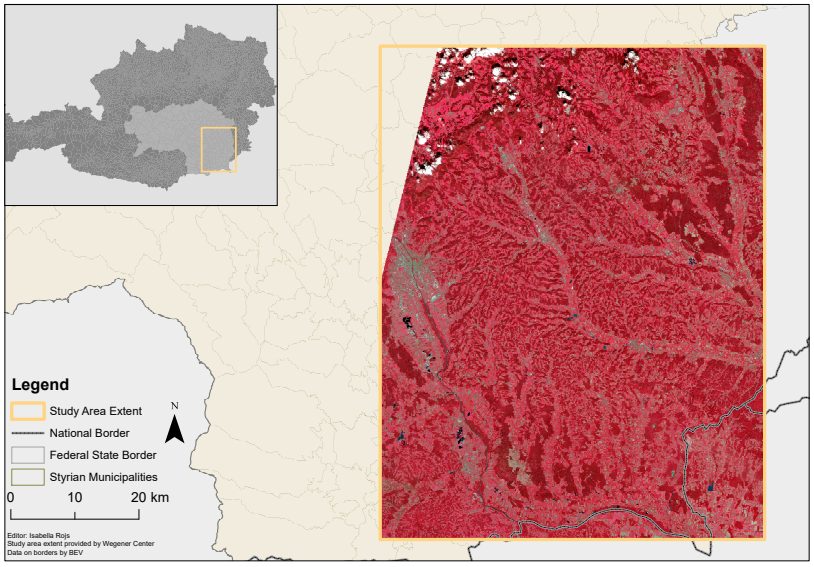

Figure 4.1: Study area

Source: own illustration

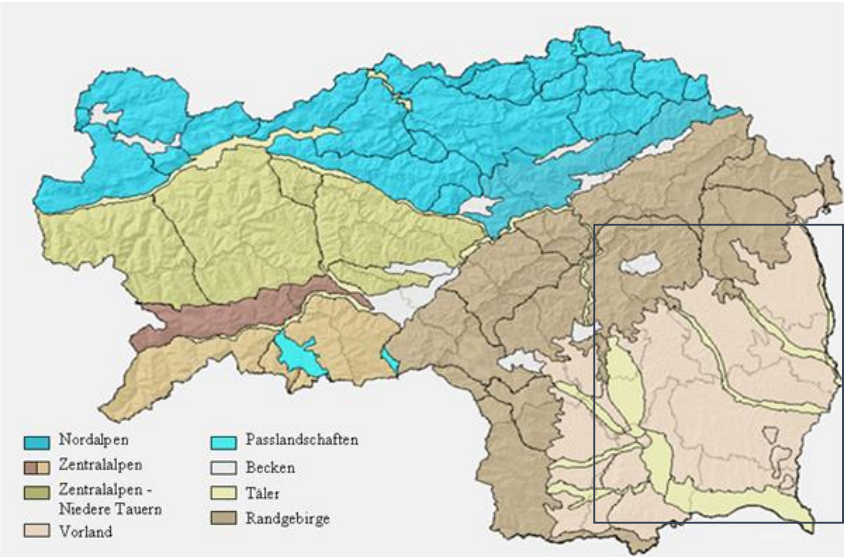

Figure 4.2: Gebietsgliederung of Styria, grey rectangle symbolises study area

Source: adapted after Wakonigg and Podesser, 2018

5 Methodology

This chapter provides an overview of the workflow, including the steps of data acquisition and pre-processing (chapter 5.1), the applied methodology for the parameter calculation (chapter 5.2, 5.3, and 5.4), and the chosen approaches for the plausibility checks (chapter 5.5). Figure 5.1 gives an overview of the workflow and, where necessary, more detailed workflow diagrams will be shown in the according sub-chapters.
The data pre-processing step is divided into two branches, as two of the three parameters (FVC and LAI) require bottom of atmosphere reflectance and one (albedo) requires top of atmosphere reflectance. From the literature review (chapter 2) a set of suitable methods for each of the three selected parameters is chosen to be applied to the imagery data. To check the plausibility of each calculated parameter, results from in-situ measurements found in literature as well as available ancillary data is required.
For albedo, non remote sensing values could be obtained for some land cover classes from literature, which will be used to validate the calculations based on Urban Atlas classifications (chapter 3.3.1) and the LiDAR-based forest classification (chapter 3.3.3). The plausibility of the FVC results will be validated using an Imperviousness Density dataset (chapter 3.3.4) provided by the city of Graz (Graz, 2019). Databases with Leaf Area Index data from field measurements are freely available for different plant types like coniferous and deciduous trees, and different crop types (chapter 3.2). This information will be used to validate the calculations based on ground cover information gained through in-situ crop type determinations (chapter 3.3.2) and the LiDAR-based forest classification (chapter 3.3.3), similar to the plausibility analysis of albedo results. Additionally, assumptions are made regarding the LAI of a forest in connection to its age class, an attribute delivered within the LiDAR dataset.

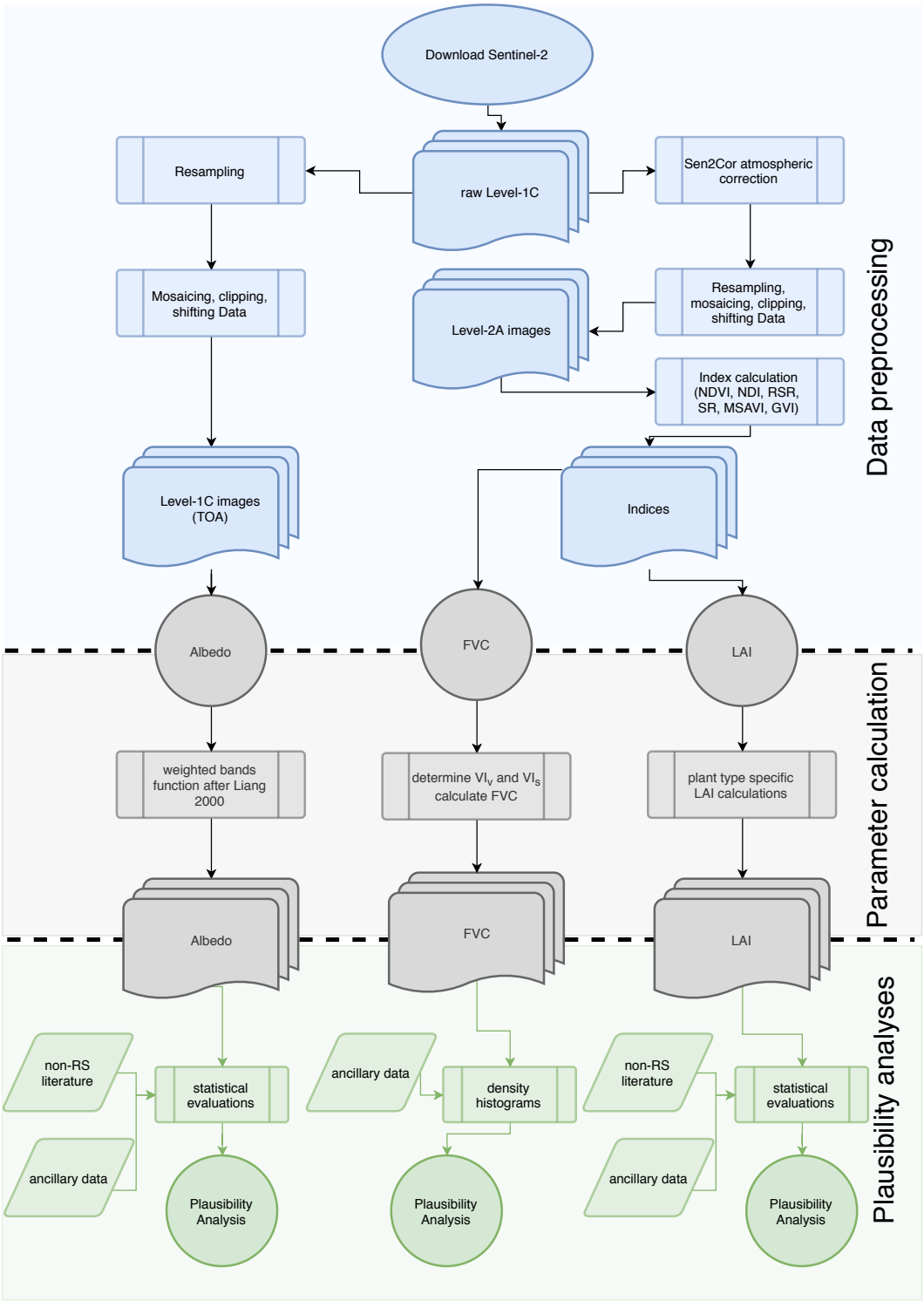

Figure 5.1: Workflow diagram

Source: own illustration

5.1 Data Acquisition and Pre-processing

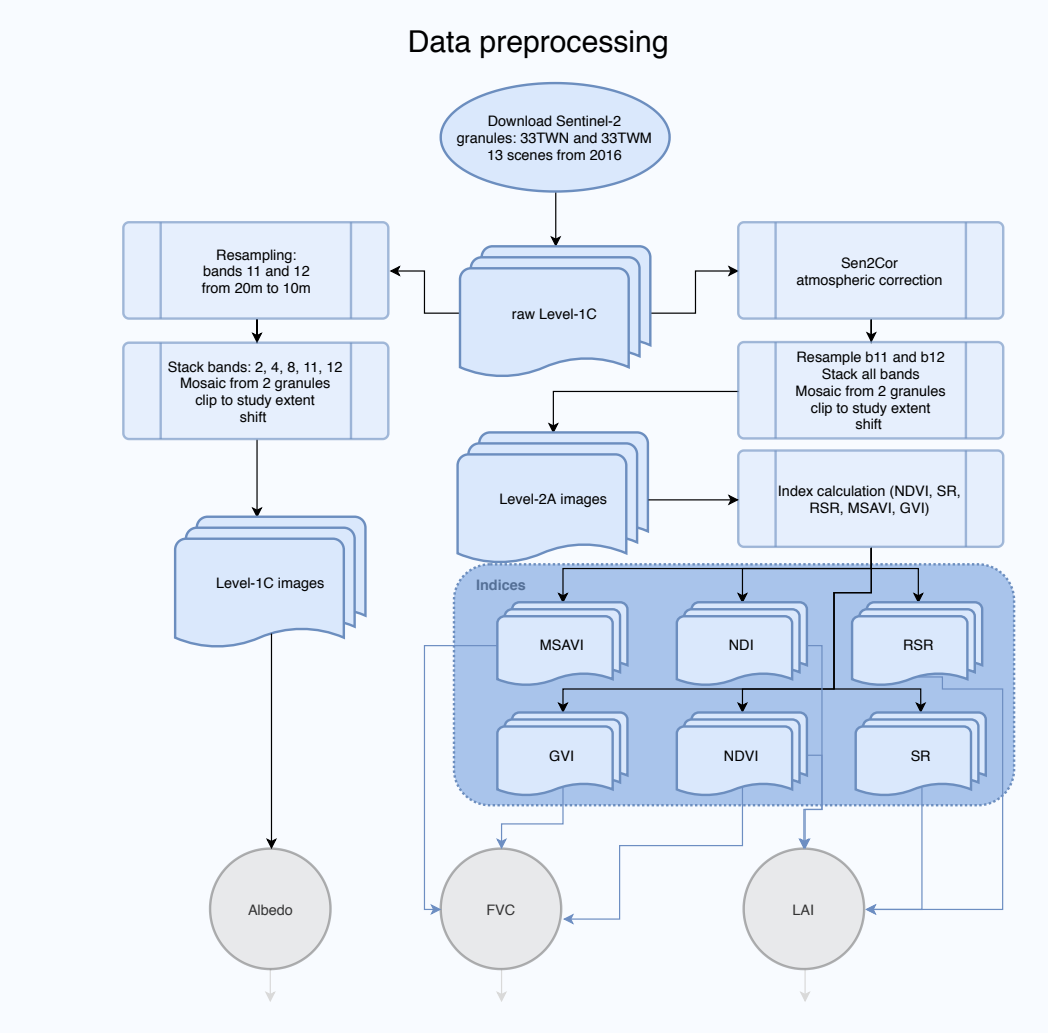

Figure 5.2: Data preprocessing workflow

Source: own illustration

Figure 5.2 gives a more detailed overview of the necessary preprocessing steps. Sentinel-2 data at Level-1C are downloaded from the *Copernicus Open Access Hub* (`https://scihub.copernicus.eu/`). To cover the study area completely (see figure 4.1) two granules are necessary: T33TWN and T33TWM (for a full list of downloaded scenes see table 3.3). As the method of S. Liang, 2000 requires top of atmosphere reflectance to calculate albedo, the Level-1C product can be used directly.
This paragraph describes the preprocessing steps of the Level-1C product (left branch in figure 5.2), which are necessary to derive albedo. First, the two SWIR bands (band 11 and band 12) are resampled from 20 m to 10 m and are stacked together with the other necessary bands for albedo calculation: bands 2 (blue), 4 (red), and 8 (NIR). Subsequently, mosaics from the two granule stacks are created for each date and clipped to the extent of the study area. After analysing the clipped scenes, a few shifts between some dates become apparent, as depicted in figure 5.3 for the scenes of 23.05.2016 (left) and 31.08.2016 (right). A master scene is determined (31.08.2016) and all scenes which do not match the master, are shifted. Table 5.1 summarises all shifted scenes. After this step, the scenes are ready to be used for the calculation of albedo after the method proposed by S. Liang, 2000.

Table 5.1: Shift for Level-1C scenes

Scene	*Shift*
14.03.2016	Y -10
13.04.2016	Y -10
23.05.2016	Y -10
29.11.2016	Y +10
09.12.2016	X +10

The right branch in figure 5.2 describes the preprocessing steps to require bottom of atmosphere reflectance values through atmospheric correction. Sen2Cor is ESA's Level-2A processor, developed by *Telespazio VEGA Deutschland GmbH* as a third-party plugin to the Sentinel-2 Toolbox, which corrects top of atmosphere reflectance from Level-1C to bottom of atmosphere reflectance (Main-Knorn, Pflug, Louis, et al., 2017). The processor also generates additional

output, like a Scene Classification (SCL) and Quality Indicators for cloud and snow probabilities, among other output (Main-Knorn, Pflug, Louis, et al., 2017; Müller-Wilm, Devignot, and Pessiot, 2017), which are not used in this thesis.

For the atmospheric correction, radiative transfer functions need to be calculated, to account for different sensor and solar geometries, ground elevations and the atmosphere (Müller-Wilm, Devignot, and Pessiot, 2017). The Sen2Cor processor uses *libRadtran*, a library consisting of several C and Fortran functions and programmes to calculate both solar and thermal radiation of the Earth's atmosphere (Müller-Wilm, Devignot, and Pessiot, 2017; Emde et al., 2016). *LibRadtran* generates several Look-Up Tables (LUTs) including tables to differentiate between (a) mid latitude summer and winter atmosphere, (b) rural and maritime aerosols, and (c) different ozone contents, to meet the conditions of the scene's geographic location and climatology (Main-Knorn, Pflug, Louis, et al., 2017). Configurations can be made in the $L2A\_GIPP.xml$ file. For the observed scenes of this thesis, the aerosol type is set to $RURAL$ and the atmosphere type is set to $AUTO$, as scenes from throughout the calendar year are being processed together.

Finally, the 20 m bands are being resampled to 10 m and stacked to images together with the other 10 m bands. Table 5.2 shows the order the stacked bands. Analogous to the top of atmosphere stacks, mosaics from the two granule stacks are created for each date and clipped to the extent of the study area. Shifts were also necessary for the bottom of atmosphere scenes (see for example figure 5.4). However, they were not congruent with the shifts needed for the top of atmosphere scenes. No satisfactory explanation could be found for this fact and was attributed to a step in the Sen2Cor process. The scene of 31.08.2016 was again chosen as the master and table 5.3 specifies the necessary shifts for the scenes.

Table 5.2: Order of bands in the bottom of atmosphere stacks

original number	number in stack	name
1	*not used*	coastal aerosol
2	1	blue
3	2	green
4	3	red
5	5	vegetation red edge 1
6	6	vegetation red edge 2
7	7	vegetation red edge 3
8	4	NIR
8a	8	narrow NIR
9	*not used*	water vapour
10	*not used*	SWIR Cirrus
11	9	SWIR 1
12	10	SWIR 2

Table 5.3: Shift for Level-2A scenes

Scene	*Shift*
14.03.2016	Y -20
13.04.2016	Y -20
23.05.2016	Y -20
12.07.2016	Y -10
29.11.2016	Y +10
09.12.2016	X +10

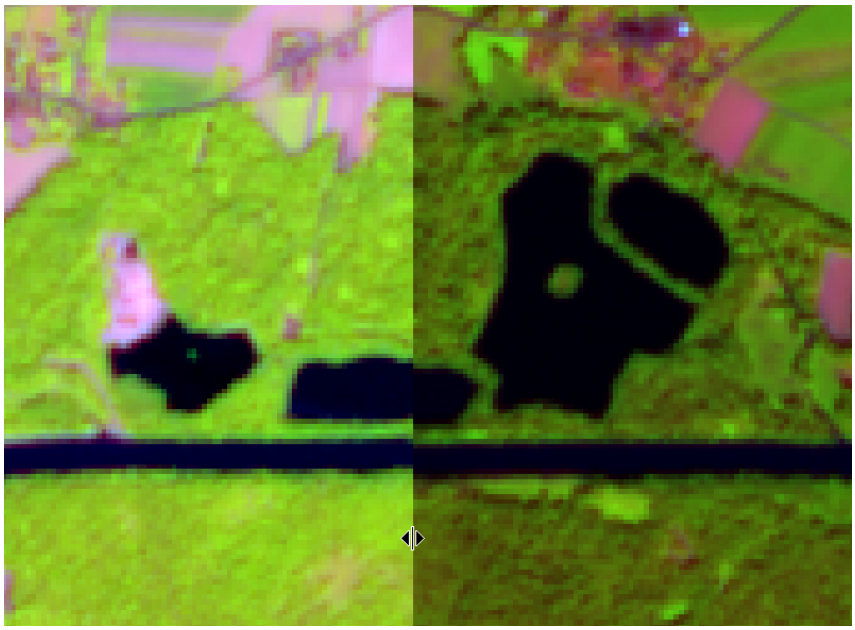

Figure 5.3: Shift at Level-1C between the scenes of 23.05.2016 (left) and 31.08.2016 (right)

Source: own illustration

Figure 5.4: Shift at Level-2A between the scenes of 09.12.2016 (top) and 31.08.2016 (bottom)

Source: own illustration

The final preprocessing step is the calculation of indices, which are required for the regression-based determination of FVC and LAI. The following indices (equations 5.1 - 5.6) are calculated (max and min in equation 5.5 are taken from each scene).

$$NDVI = \frac{\rho_{nir} - \rho_{red}}{\rho_{nir} + \rho_{red}} \tag{5.1}$$

(Johnson, Tateishi, and Kobayashi, 2012; Chen and Cihlar, 1996; Schiffmann et al., 2008; Bach et al., 2003)

$$GVI = \frac{\rho_{green} - \rho_{red}}{\rho_{green} + \rho_{red}} \tag{5.2}$$

(Jiménez-Muñoz, J. A. Sobrino, Plaza, et al., 2009)

$$MSAVI = \frac{2 \cdot \rho_{nir} + 1 - \sqrt{(2 \cdot \rho_{nir} + 1)^2 - 8 \cdot (\rho_{nir} - \rho_{red})}}{2} \tag{5.3}$$

(Johnson, Tateishi, and Kobayashi, 2012)

$$SR = \frac{\rho_{nir}}{\rho_{red}} \tag{5.4}$$

(Schiffmann et al., 2008)

$$RSR = \frac{\rho_{nir}}{\rho_{rededge1}} \cdot \frac{\rho_{swir2}^{max} - \rho_{swir2}}{\rho_{swir2}^{max} - \rho_{swir2}^{min}} \tag{5.5}$$

(Schiffmann et al., 2008)

$$NDI_{B5-B4} = \frac{\rho_{rededge1} - \rho_{red}}{\rho_{rededge1} + \rho_{red}} \tag{5.6}$$

(Delegido, Verrelst, Alonso, et al., 2011)

5.2 Remote sensing of Albedo

To obtain albedo values, the method proposed by S. Liang, 2000 is chosen, as it is relatively easy to implement and applied to all preprocessed TOA-images. As described in chapter 2.1, Liang's method was developed for Landsat ETM+ data (as well as for other sensors). Therefore, promising results of applying the approach developed for Landsat to Sentinel-2 data are expected due to the comparable band widths of the two sensors, as can be seen in figure 5.5. The chosen method comprises a function of weighted bands, which is given as a weighted average function (by Smith, 2010) in equation 5.7.

$$\alpha = \frac{0.356 \cdot \rho_{blue} + 0.13 \cdot \rho_{red} + 0.373 \cdot \rho_{nir} + 0.084 \cdot \rho_{swir1} + 0.072 \cdot \rho_{swir2} - 0.0018}{0.356 + 0.13 + 0.373 + 0.084 + 0.072} \tag{5.7}$$

For Sentinel-2 products, at top of atmosphere and bottom of atmosphere level, the quantification value of 10000 needs to be kept in mind, resulting in applying a factor of $\frac{1}{10000}$ to the Digital Number (DN) values, to get actual reflectance values (Main-Knorn, Pflug, Louis, et al., 2017). The weighting function in equation 5.7 is applied to all 13 Level-1C images.

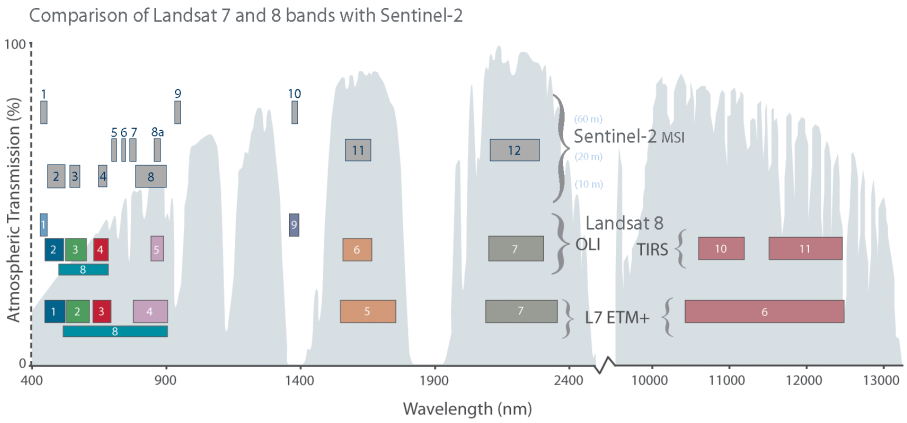

Figure 5.5: Comparison of Landsat 7 and 8 and Sentinel-2 bands

Source: Landsat, 2019

5.3 Remote sensing of Fraction of Vegetation Cover

The workflow for the calculation of FVC is shown in figure 5.6. In order to obtain Fraction of Vegetation Cover from the Sentinel-2 images, a linear regression-based approach is deployed. This scaled VI function (see equation 5.8) is relatively easy to implement with a range of different Vegetation Indices, but some considerations have to be put into determining VI_v (Vegetation Index of a fully vegetated pixel) and VI_s (Vegetation Index of a bare soil pixel).

$$FVC = \frac{VI - VI_s}{VI_v - VI_s} \tag{5.8}$$

Two regression based approaches for the remote sensing based retrieval of the FVC were considered in this thesis:

- Jiménez-Muñoz, J. A. Sobrino, Plaza, et al., 2009, who tested the GVI and NDVI (among other indices), and
- Johnson, Tateishi, and Kobayashi, 2012, who used the indices NDVI and MSAVI (Modified Soil-Adjusted Vegetation Index).

Theoretically, any Vegetation Index could be used for equation 5.8. NDVI was chosen, because it is the most commonly used index in linear regression methods to obtain FVC (e.g. Johnson, Tateishi, and Kobayashi, 2012; Jiménez-Muñoz, J. A. Sobrino, Plaza, et al., 2009; Barati et al., 2011; Buyantuyev, J. Wu, and Gries, 2007; Kaspersen, Fensholt, and Drews, 2015; Barlage and Zeng, 2004). The GVI was chosen, as this index performed only slightly inferior compared to Spectral Mixture Analysis and automated approaches (Jiménez-Muñoz, J. A. Sobrino, Plaza, et al., 2009), thus making it a promising candidate for the linear regression model. MSAVI was chosen as a third index because of its lower sensitivity to soil brightness compared to NDVI (Johnson, Tateishi, and Kobayashi, 2012), therefore a comparison to NDVI results intended to either confirm or refute this statement. Two aspects should be noted at this point. First, Johnson, Tateishi, and Kobayashi, 2012 used ASTER data for their study, which are comparable in band width at least in the visible and near infra-red wavelengths to Sentinel-2 data. Second, Jiménez-Muñoz, J. A. Sobrino, Plaza, et al., 2009 used CHRIS data, which is a hyperspectral dataset with entirely different band widths in comparison to Sentinel-2. Given the

formulation of the regression function, however, the applicability of indices tested with hyperspectral remote sensing images is also given for Sentinel-2 data, as long as the calculation method of the given index is adapted to the used sensor.

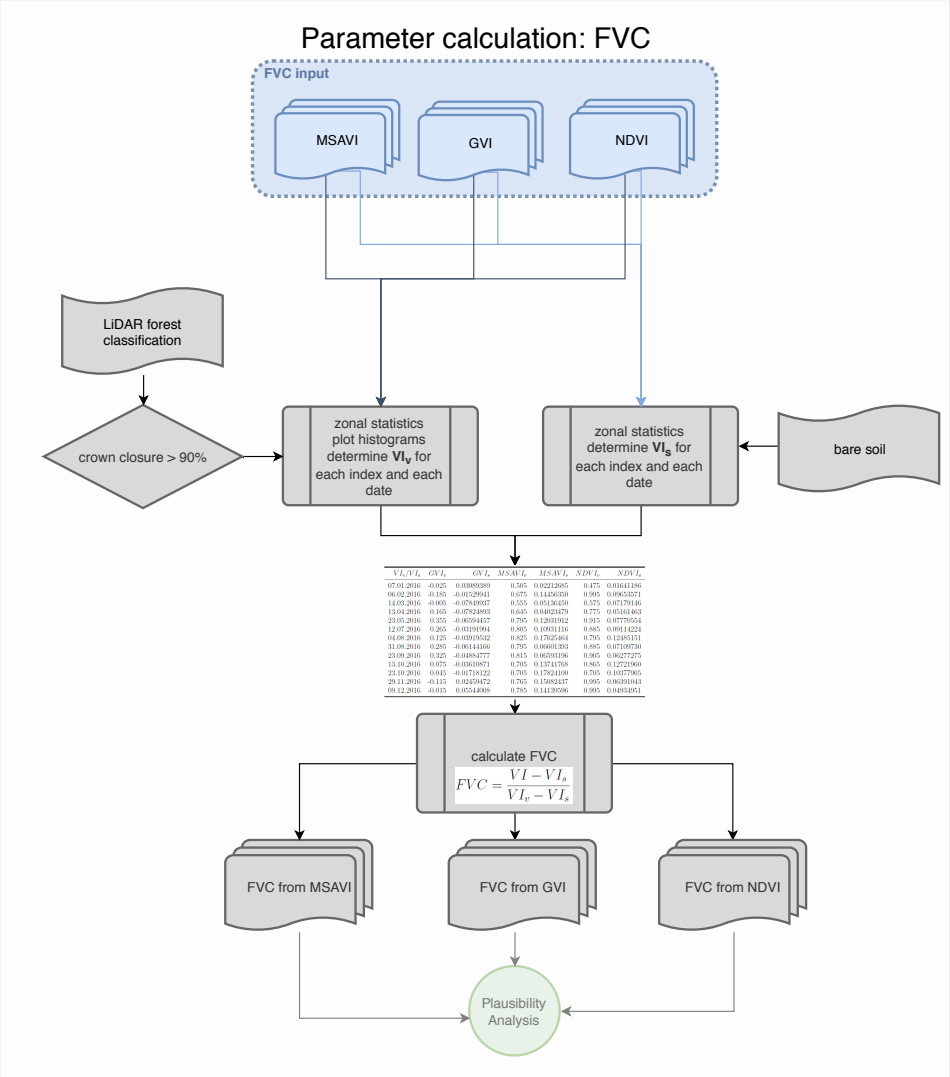

Figure 5.6: Workflow for the parameter FVC

Source: own illustration

To determine VI_v, data from the forest classification (see chapter 3.3.3) is used. To receive only polygons which are fully vegetated, the parameter *crown closure* is considered. All polygons from the forest classification with a crown closure greater than 90 % can be assumed to be *fully vegetated* and are exported into a separate shapefile, which is used to perform zonal statistics on the index raster files. The zonal statistics step calculates the mean of each of the approximately 292 000 forest polygons. Using R software, histograms are plotted with the mean values and maximum peaks are detected (see figure 5.7), as proposed by Jiménez-Muñoz, J. A. Sobrino, Plaza, et al., 2009. It is advised to use the peak for VI_v instead of the maximum of the histogram, because it is more robust than (possibly extreme) outliers.

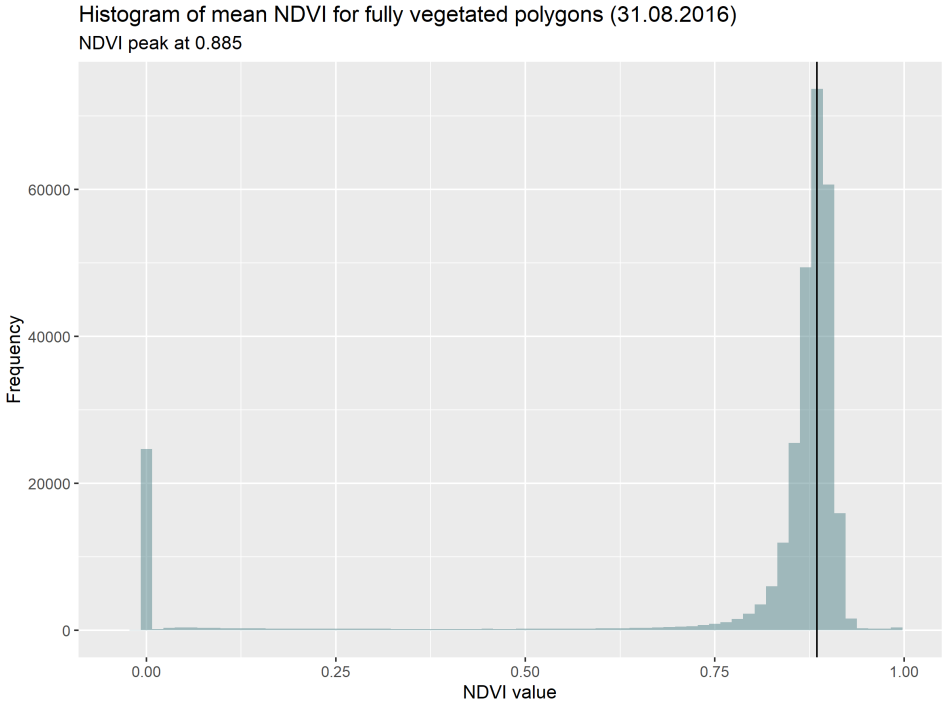

Figure 5.7: NDVI value histogram for scene 8 (31.08.2016)

Source: own illustration

To select suitable VI_s values, a similar procedure is applied. As no ground truth data on bare soil was available beforehand, a dataset needs to be generated

through visual interpretation of the Senitnel-2 data. Zonal statistics are performed to acquire the mean of each polygon. Contrary to VI_v, no histograms are plotted due to the lower number of available polygons. Instead, the mean of all values greater than 0 is determined for $NDVI_s$ and $MSAVI_s$ as Johnson, Tateishi, and Kobayashi, 2012 proposed to avoid negative values. For GVI_s, Jiménez-Muñoz, J. A. Sobrino, Plaza, et al., 2009 allowed negative values, so no constraint is used when determining this mean. Table 5.4 lists all acquired VI_v and VI_s for each investigated date and each of the three tested indices. With this information, equation 5.8 can be applied to the index raster files of each investigated date to obtain Fraction of Vegetation Cover. Only scenes 6 (12.07.2016) to 9 (23.09.2016) are used for this parameter.

Table 5.4: VI_v and VI_s per date of the three selected indices

VI_v/VI_s	GVI_v	GVI_s	$MSAVI_v$	$MSAVI_s$	$NDVI_v$	$NDVI_s$
12.07.2016	0.265	-0.03191994	0.805	0.10931116	0.885	0.09114224
04.08.2016	0.125	-0.03919532	0.825	0.17625464	0.795	0.12485151
31.08.2016	0.285	-0.06144166	0.795	0.06601393	0.885	0.07109730
23.09.2016	0.325	-0.04884777	0.815	0.06593196	0.905	0.06277275

5.4 Remote sensing of Leaf Area Index

As described in chapter 2.3 there are two main remote sensing techniques to retrieve Leaf Area Index:

1. empirical retrieval methods, establishing a (non-)linear regression between a VI and the LAI measured on the ground, and
2. physically-based retrieval methods via inversion of RTMs (Pasqualotto et al., 2019).

The aim of this thesis is to derive biogeophysical parameters from optical remote sensing data, therefore an emphasis is put on finding applicable empirical methods based on spectral VIs. Physically-based approaches require ancillary information on e.g. the canopy structure of the investigated surface for the parametrisation of the RTM (Pasqualotto et al., 2019), which is not available for this thesis.
The LAI is plant type dependent (e.g. Haboudane et al., 2004; González-Sanpedro et al., 2008), therefore it cannot be derived on pixel-level with one formula for an entire scene, like for FVC and albedo. Different plant cover types require different empirical relationships. As mentioned in previous chapters, information on land cover in the region of interest is available for forest (see chapter 3.3.3) and different crop types (see chapter 3.3.2), therefore LAI methods will be tested based on these two main classes.
The respective LAI formulas to be applied in the test region of the thesis were chosen from the literature according to their applicability to the study area and especially to the sensor-specific settings. Many studies use hyperspectral sensors to derive empirical relationships between a vegetation index and Leaf Area Index (Nguy-Robertson, Gitelson, et al., 2012; Nguy-Robertson, Peng, et al., 2014; Tanaka et al., 2015; Viña et al., 2011; Gong and J. R. Miller, 1995). Due to the differences in band widths between hyperspectral sensors and sensors like Sentinel-2, the derived vegetation indices from these sensors are not comparable and therefore an empirical relationship between a narrowband index (obtained from a hyperspectral image) and the LAI is not transferable to Sentinel-2 data.
For the available ground truth data (forest and crops) three approaches were chosen. Figure 5.8 depicts a structured overview of all these methods, which will be explained in the following two chapters, 5.4.1 and 5.4.2.

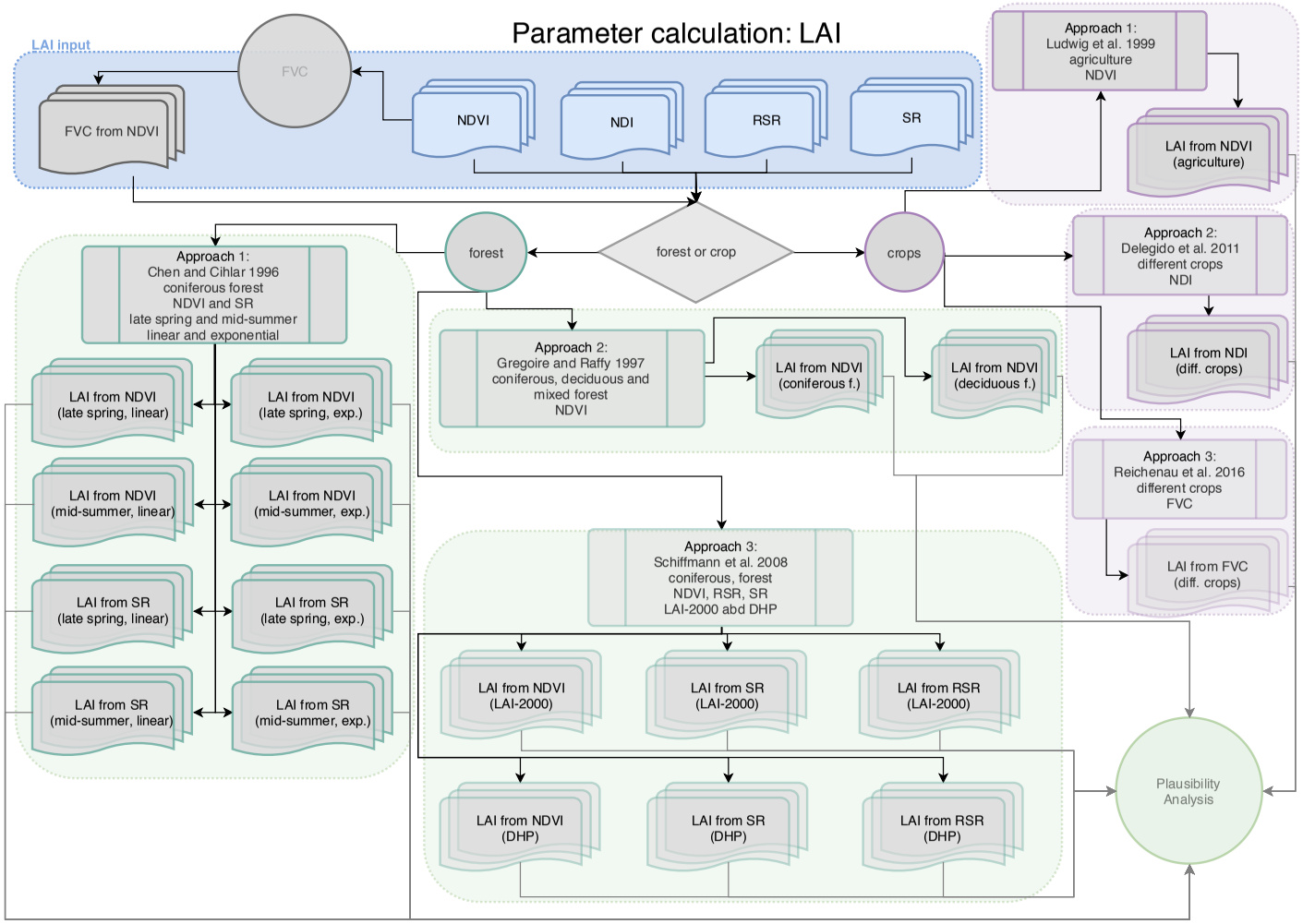

Figure 5.8: Workflow for the parameter LAI

Source: own illustration

5.4.1 LAI regression functions for forest

In order to retrieve Leaf Area Index for forest, three methods were chosen from the literature, which present empirical relationships between ground based LAI measurements and satellite data. The results will be validated using information on the ground covers coniferous and deciduous forest provided by the LiDAR-based forest map (chapter 3.3.3). Table 5.5 gives a summarised overview of the three methods, and their application to the present study area and data will be discussed in this chapter. (The abbreviations in column 1 are used for the authors of the cited studies; the other abbreviations will be described in following paragraphs).

Table 5.5: Structured summary of empirical LAI retrieval methods for *forest*

Approach	*Details*	*Number of equations*
Chen and Cihlar, 1996 (CC)	2 VIs (NDVI, SR), 2 models (linear, exponential), 2 dates (late spring, mid-summer)	8 (eq. 5.9 - 5.16)
Gregoire and Raffy, 1997 (GR)	2 classes (coniferous forest, deciduous forest	2 (eq. 5.17 - 5.18)
Schiffmann et al., 2008 (SM)	3 indices (NDVI, RSR, SR), 2 ground observation methods (LAI-2000, DHP)	6 (eq. 5.19 - 5.24)

Approach 1
Chen and Cihlar, 1996 (abbr. CC) used Landsat TM data from spring and summer of 1994 at two boreal coniferous forest test sites in central Canada. To acquire ground truth, they used the gap fraction estimator *LAI 2000 Plant Canopy Analyzer* to measure LAI in the beginning, middle and end of growing season in 1994. With two spectral indices, NDVI and SR (Simple Ratio), they formulated equations to express the empirical relationship between their ground truth measurements and the Landsat-derived indices. As no cloud-free Landsat images from the end of the growing season were available, only relationships for the beginning (late spring) and middle (mid-summer) of the growing season could be established. For each growing period and index, a linear and exponential regression function were developed:

$$LAI = \frac{NDVI - 0.519}{0.051} \quad (NDVI, late\ spring, linear) \tag{5.9}$$

$$LAI = \sqrt[0.1844]{\frac{NDVI}{0.552}} \quad (NDVI, late\ spring, exponential) \tag{5.10}$$

$$LAI = \frac{SR - 2.781}{0.842} (SR, late\ spring, linear) \tag{5.11}$$

$$LAI = \sqrt[0.3916]{\frac{SR}{3.437}} \quad (SR, late\ spring, exponential) \tag{5.12}$$

$$LAI = \frac{NDVI - 0.635}{0.032} \quad (NDVI, mid - summer, linear) \tag{5.13}$$

$$LAI = \sqrt[0.1057]{\frac{NDVI}{0.654}} \quad (NDVI, mid - summer, exponential) \tag{5.14}$$

$$LAI = \frac{SR - 3.637}{1.014} \quad (SR, mid - summer, linear) \tag{5.15}$$

$$LAI = \sqrt[0.3228]{\frac{SR}{4.711}} \quad (SR, mid - summer, exponential) \tag{5.16}$$

For the present thesis, NDVI and SR were derived from the atmospherically corrected Sentinel-2 images using equations 5.1 and 5.4, which in turn were used to calculate the LAI according to equations 5.9 - 5.16.

Approach 2

Approach 2 is taken from Bach et al., 2003, who applied a regression function established by Gregoire and Raffy, 1997 (abbr. GR). Unfortunately the original work was not accessible, so no information is available about the circumstances under which this empirical relationship was formed. Bach et al., 2003 apply the exponential regression functions to Landsat TM data from October 1994 and May 1996 for different LCLU classes in the Toce basin in Northern Italy, to use the produced LAI as an input parameter to improve their hydrological model. Their combination of sensor and study area suggest applicability to the used data and site of this thesis.

The following two equations describe the empirical relationships between LAI and the used Vegetation Index NDVI for coniferous forest (equation 5.17) and deciduous forest (equation 5.18):

$$LAI = 1.86 \cdot NDVI^{6.06} \quad (coniferous\ forest) \tag{5.17}$$

$$LAI = 1.63 \cdot NDVI^{4.7} \quad (deciduous\ forest) \tag{5.18}$$

Approach 3
Schiffmann et al., 2008 (abbr. SM) measured LAI in Yosemite National Park, USA from different coniferous tree types and established empirical relationships between them and three indices derived from a Landsat TM image from July 2007. For the ground measurements of LAI the plant canopy analyser LAI-2000 and Digital Hemispherical Photography (DHP) were used. The indices used for the regression analysis were NDVI, RSR (Reduced Simple Ratio), and SR. A regression function was formulated for each index and each of the two ground measuring methods separately:

$$LAI = 6.7537 \cdot NDVI - 0.8384 \quad (LAI - 2000) \tag{5.19}$$

$$LAI = 5.5465 \cdot NDVI - 0.7857 \quad (DHP) \tag{5.20}$$

$$LAI = 0.8213 \cdot RSR + 0.176 \quad (LAI - 2000) \tag{5.21}$$

$$LAI = 0.6789 \cdot RSR - 0.001 \quad (DHP) \tag{5.22}$$

$$LAI = 0.7879 \cdot SR - 0.5889 \quad (LAI - 2000) \tag{5.23}$$

$$LAI = 0.6471 \cdot SR - 0.6145 \quad (DHP) \tag{5.24}$$

5.4.2 LAI regression functions for crop types

For the retrieval of Leaf Area Index for crops, three methods from the literature are adapted. Although the crop-type dependency is highlighted in chapter 2, in the case of this thesis only those approaches are applicable, where the crop type was not considered. This is due to the sensors used, as many studies, which examine specific crop types for an empirical VI-LAI relationship use hyperspectral data (e.g. Viña et al., 2011; Tanaka et al., 2015; Nguy-Robertson, Gitelson, et al., 2012; Nguy-Robertson, Peng, et al., 2014). For the validation, information on crop type (chapter 3.3.2) will be used.

Approach 1
The first approach is also taken from Bach et al., 2003, who used an empirical relationship for the LCLU class *agriculture* to obtain LAI. The coefficients for this exponential function were found by Ludwig et al., 1999 (as cited in Bach et al., 2003) and, according to Bach et al., 2003, published for an EARSEL Workshop. Unfortunately this publication could not be retraced. Similar to Approach 2 in chapter 5.4.1, no information is available about the circumstances of Ludwig's study, but its application to Landsat TM data in Northern Italy are comparable to this thesis, therefore it was decided to try out this approach. The following equation 5.25 describes the relationship:

$$LAI = 1.6 \cdot NDVI^3 \tag{5.25}$$

Approach 2
Delegido, Verrelst, Alonso, et al., 2011 use Sentinel-2 red edge simulations obtained from hyperspectral CHRIS data. Ground measurements for different crop types were taken from three ESA campaigns (SPARC, AgriSAR, and CERES2), which were acquired between 2003 and 2007. Formulating a Normalised Difference Index (NDI, equation 5.26), two-band combinations with the most linear relationship to the LAI ground measurements were examined. Their results show, that the bands centred at 706 nm and 664 nm, which correspond to bands 5 (red edge 1) and 4 (red) of the Sentinel-2 satellite, deliver the best results. The following linear equation 5.27 is the best-fit function to calculate LAI according to Delegido, Verrelst, Alonso, et al., 2011.

$$NDI = \frac{\rho_b - \rho_a}{\rho_b + \rho_a} \tag{5.26}$$

$$LAI = 8.452 \cdot \frac{\rho_{706} - \rho_{664}}{\rho_{706} + \rho_{664}} \tag{5.27}$$

Approach 3
Approach 3 is adapted from Reichenau et al., 2016, who correlated ground-based LAI measurements of winter wheat, sugar beet and maize from the growing seasons of 2008 to 2012, taken in Western Germany, to RapidEye data. Although band widths of the RapidEye are slightly broader compared to Sentinel-2 (eoPortal, 2019), it was decided to apply this approach to the

test site. Reichenau et al., 2016 determined the FVC from the image data analogous to the approach used in this thesis (see chapter 5.3) also using the NDVI. $NDVI_s$ and $NDVI_v$ were obtained using histogram analysis of the land cover classes bare soil and broadleaf forest respectively. LAI is calculated from FVC using the following function (after Norman, 1979, as cited in Reichenau et al., 2016):

$$LAI = \frac{-ln(1 - FVC)}{k(\mu)} \tag{5.28}$$

The factor $k(\mu)$ describes the *light extinction coefficient for a solar zenith angle and is a measure of the attenuation of radiation in the canopy* (Reichenau et al., 2016). Following Aubin, Beaudet, and Messier, 2000, $k(\mu)$ can be assumed as 0.54. For the present thesis, the FVC results of chapter 5.3 obtained from NDVI were taken, to calculate the LAI.

5.5 Plausibility Analyses

To check the plausibility of the obtained results, several approaches are considered. When available, parameter values for certain types of ground cover, gained through non-remote sensing methods, are taken from the according literature and compared to the results of the tested methods. Information on ground cover, necessary for this approach, is taken from several available sources, which are described in chapter 3. The following three sub-chapters describe the used techniques to test the plausibility of each parameter separately.

5.5.1 Plausibility of Albedo results

In order to test the calculated albedo results for plausibility, typical albedo ranges for different ground cover types are adapted from Pielke and Avissar, 1990 (see table 5.6, columns 2 and 3). To extract information on the ground cover of the study area, the land cover and land use classification of the Urban Atlas layer (see chapter 3.3.1) as well as the LiDAR-based forest map (chapter

3.3.3) are used. Considering the occurrence within the study area and the investigated cover types in the literature and the Urban Atlas classification, the following classes (table 5.6) will be examined:

Table 5.6: Typical albedo ranges for different cover types, assigned to Urban Atlas classes (classes marked with (*) are taken from the forest classification (see chapter 3.3.3))

LC/LU class from Urban Atlas	*Cover type from Pielke and Avissar, 1990*	*albedo range*
11100: Continuous Urban fabric (S.L. >80%), 11210: Discontinuous Dense Urban Fabric (S.L.: 50% - 80%), 11220: Discontinuous Medium Density Urban Fabric (S.L.: 30% - 50%, 11230: Discontinuous Low Density Urban Fabric (S.L.: 10% - 30%)	urban area	0.15 - 0.27
21000: Arable land (annual crops)	agricultural crops	0.10 - 0.30
23000: Pastures	meadows	0.15 - 0.25
Coniferous forest(*)	coniferous forests	0.10 - 0.15
Deciduous forest(*)	deciduous forests	0.15 - 0.20

Source: Copernicus, 2019b; Pielke and Avissar, 1990

The available vector data of the Urban Atlas classes (the four classes on urban fabric are all combined to one class, referred to as *urban*) are reprojected to WGS84 (EPSG 32633) to match the projection of the satellite images and rasterised to use as masking layers for the albedo calculations. Additionally, a negative buffer of 10 m is applied to the Urban Atlas layers, which are delivered on the basis of 20 m spatial resolution data, to avoid mixed pixels at the borders of objects. For the classes *coniferous forest* and *deciduous forest*, the LiDAR-based forest map is used, as the Urban Atlas classification makes no distinction between those two cover types and only uses one class, *forests* (see figure 3.2). These datasets are delivered at a higher spatial resolution, therefore no negative buffer is necessary.
To validate the overall accuracy of the calculations, zonal statistics are computed, calculating the mean albedo value of each polygon within a class. To avoid distortion of the zonal statistics results from cloud cover, a cloud free area

within the study area with the size of approximately 190 km^2 is determined for this step. In this process, the two scenes from October (13.10. and 23.10.) had to be excluded because of their high cloud coverage. Following, all polygons are counted, which have a calculated mean albedo within the expected range (taken from table 5.6). This number is compared to the number of all polygons within the same class and date, resulting in the ratio of polygons with a correctly calculated mean albedo.
The mean value, however, cannot account for outliers and the distribution of values, therefore boxplots are visualised for the albedo calculations. Using the same ground truth as in the previous approach, all pixels within one class and date are grouped and depicted within a boxplot. For each ground truth class all dates are plotted in one graphics, also indicating the expected range taken from table 5.6.

5.5.2 Plausibility of FVC results

The soil sealing map of Graz (Graz, 2019) provides the basis of the plausibility analyses of FVC results. Imperviousness and Fraction of Vegetation Cover both describe a covered fraction per ground unit so they both complement each other to 100% per pixel (Kaspersen, Fensholt, and Drews, 2015). The soil sealing map delivers information on 100% sealed surfaces. The dataset is rasterised to a spatial resolution of 10 m to match the Sentinel-based FVC calculations (see black raster in figure 5.9). Additionally, the rasterised sealing map is shrunk by 1 pixel (see blue raster in figure 5.9). This step is necessary to avoid errors at the edges of objects due to Sentinel's geometric accuracy, which is report to lie between 11 m or 1.1 pixel (Clerk, 2019) and as low as 6 m or 0.6 pixel (Pandzic et al., 2016). As the accuracy can be above 1 pixel, a shrink and blow operation of 1 pixel is applied to the blue raster, to avoid the edge effect at lengthy but narrow objects, like streets. The result of this operation is the yellow raster in figure 5.9. This raster set is used to validate the FVC calculations. As it presents ground truth of 100% sealed surfaces, the FVC calculations are expected to have values close to 0, where they are covered by the yellow raster. The raster serves as a mask for the FVC calculations and the masked values are used to create density histograms to analyse the relative value distribution.

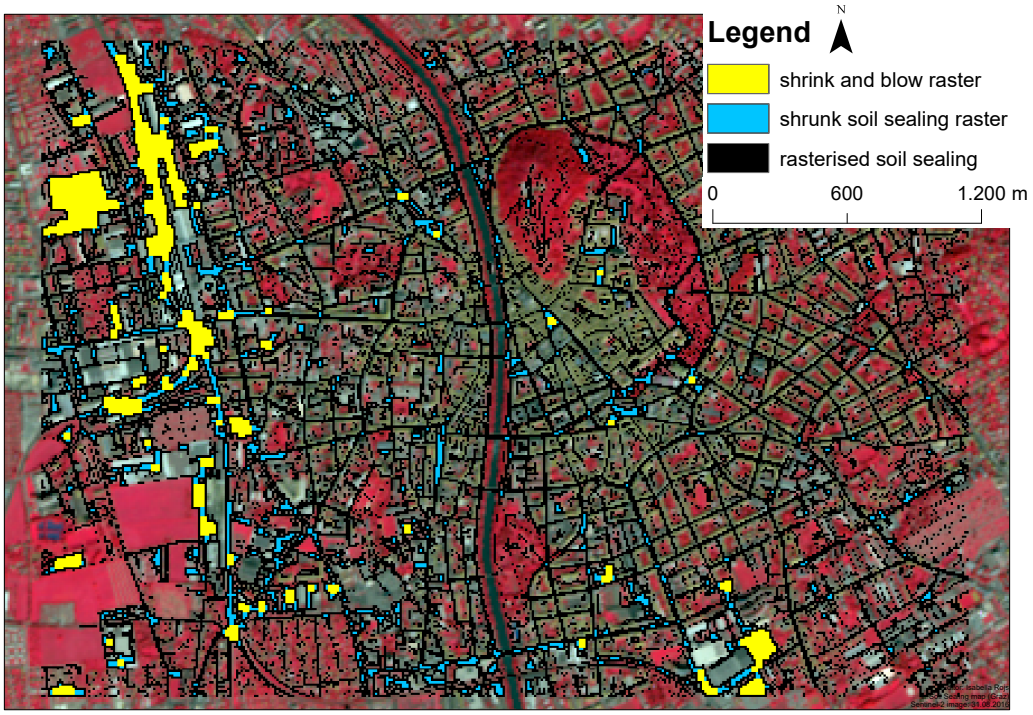

Figure 5.9: Rasterised soil sealing map of the (inner) city of Graz

Source: own illustration, data by Graz, 2019

5.5.3 Plausibility of LAI results

Leaf Area Index plausibility tests are performed using ground truth data from

- the LiDAR-based forest classification (see chapter 3.3.3), and
- the crop type ground truth dataset (see chapter 3.3.2).

From the large LiDAR dataset a subset is used to reduce computing time and ensure cloud-free conditions for all dates. Chen and Cihlar, 1996 differentiate between late spring and mid-summer in their regression formulas so scenes 5 (23.05.2016) and 6 (12.07.2016) are used to validate these results. Schiffmann et al., 2008 specify using a Landsat TM scene from July, so the according Sentinel-2 scene from July (scene 6) is used in this case. Bach et al., 2003 use several dates, so their approach will be tested on scenes 3, 4, 5, 6, 8, and 9.

Scene 7 had to be taken out of the validation due to cloud coverage in the area of interest. Reference data from the LAI database, published by Iio and Ito, 2014, will be used, to verify the results with boxplots, analogous to albedo plausibility tests. Additionally, a relation between the LAI of a forest and its age class is assumed. Statements from literature regarding the LAI of forests at different growing stages are used to analyse the LAI of the calculations based on the attribute age class, available from the LiDAR dataset.
To validate the chosen methods for crop-specific LAI, the two largest classes (most available cloud free polygons) are chosen from the dataset: *maize* (90 polygons) and *wheat* (53 polygons). The ground truth dataset is rasterised to use as a masking layer for the LAI calculation rasters. Expected ranges of LAI per crop classes *maize* and *wheat* (taken from Scurlock, Asner, and Gower, 2001) are used to analyse the calculated value distribution within each class. Depending on their growing cycle, scenes 3 to 8, and 9 are used. Also in this case, scene 7 had to be taken out of the validation due to cloud coverage in the area of interest.

6 Results and Discussion

This chapter will present the results of the plausibility analyses for each of the three parameters individually. Each presentation of results will be followed instantly by a discussion, for a more coherent reading.

6.1 Results and discussion of Albedo plausibility analysis

To validate the overall accuracy of the calculations, zonal statistics are computed, calculating the mean albedo value of each polygon within a class (column 2 in table 5.6) of the Urban Atlas dataset. All polygons within a class (for classes see table 5.6) with correctly calculated mean albedo, meaning the mean albedo lies within the expected range of the class (for ranges see table 5.6), are counted and compared to the overall number of polygons within that class. The resulting percentage of correctly calculated polygons is shown in table 6.1. The class water had to be excluded from this validation, because no adequate number of polygons within the cloud free area could be detected to obtain a meaningful result.
Looking at the overall mean, the classes *crops* and *pastures* scored the best results with an overall mean of 89.22% and 80.63% respectively, and *deciduous forest* has the poorest overall mean with 42.84%. Observing the dates individually, the January scene performs poorly for the classes *urban*, *crops*, *pastures*, and *deciduous forest* but at 59% mediocre for coniferous forest. In February, the classes *pastures* and *crops* deliver mediocre to good success rates while the remaining classes still perform poorly. From March to December a similar trend is visible in all classes: the rates of correctly calculated polygons increase during spring and summer and then decrease again towards the end of

the year. It can also be seen in table 6.1, that the highest success rate in nearly all classes (except *coniferous forest*) is reached between the months of April to September. Delimiting the overall mean to those months (April - September), the results reach close to 100% for the classes *urban*, *crops*, and *pastures*. The two forest classes *coniferous forest* and *deciduous forest* generally accomplish mostly mediocre results with a slight increase for the scenes from July and August.

Table 6.1: Ratio of polygons with a correctly calculated mean albedo per class and date

date	*urban*	*crops*	*pastures*	*conif. forest*	*decid. forest*
07.01.2016	0.1976	0.2541	0.0464	0.59	0.3082
06.02.2016	0.1948	0.8628	0.6783	0.1634	0.0286
14.03.2016	0.6976	0.9212	0.7667	0.5192	0.1855
13.04.2016	0.9747	1	0.9870	0.8079	0.6097
23.05.2016	0.9869	1	0.9899	0.5395	0.6504
12.07.2016	0.9934	1	0.9928	0.5061	0.8344
04.08.2016	0.9672	1	0.9913	0.8808	0.8256
31.08.2016	0.9607	1	0.9812	0.8413	0.7717
23.09.2016	0.7219	0.9973	0.9507	0.4932	0.2855
29.11.2016	0.3933	0.8886	0.7580	0.3113	0.1003
09.12.2016	0.3717	0.8899	0.7275	0.3005	0.1129
mean p. class	0.6782	0.8922	0.8063	0.5412	0.4284
mean p. class (Apr. - Sep.)	0.9341	0.9995	0.9821	0.6781	0.6629

The reason for the January scene falling out of alignment in all classes (except *coniferous forest*) is the snow cover, that was present during the acquisition time of this Sentinel-2 scene, as depicted in figure 6.1. It was described in chapter 2.1, that snow cover, as well as many atmospheric conditions, have an influence on the albedo of a surface (e.g. S. Wang and Davidson, 2007; Rautiainen, Stenberg, et al., 2011). Liang's method appears to be sensitive to snow cover, but the low success rate in correctly calculated means indicates,

that the ranges are not compatible with a present snow cover. Figure 6.1 shows, that the tree tops are not covered in snow, which might be an explanation for the better results in the class *coniferous forest* as opposed to the other classes in January. During the remaining dates no snow cover was present in the study area.

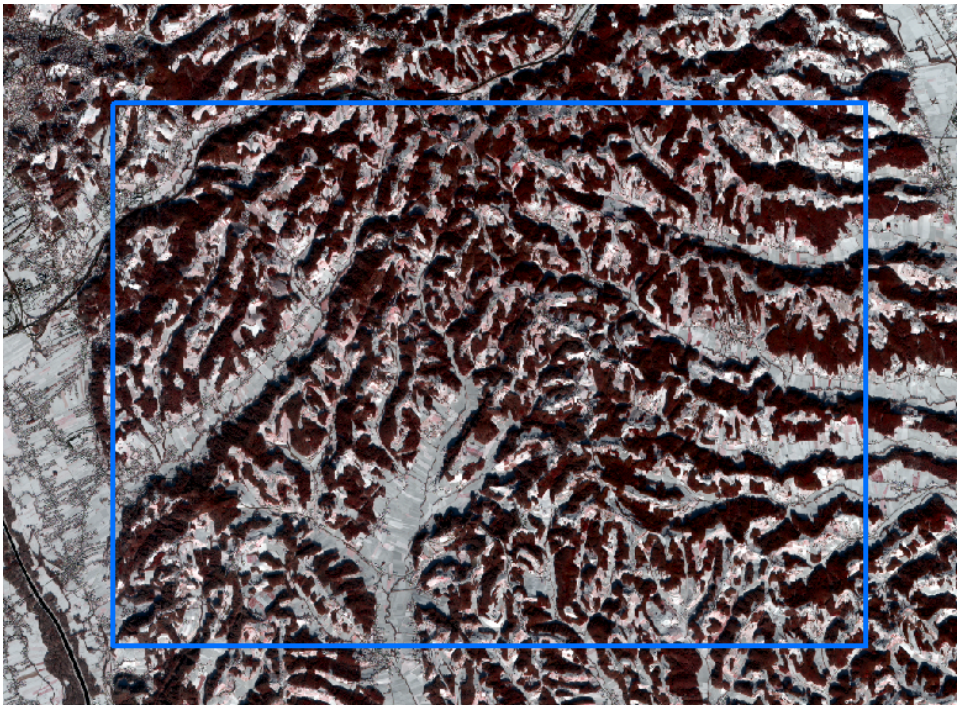

Figure 6.1: Snow cover in the Sentinel-2 scene from January, the blue rectangle indicates the investigated area

Source: own illustration

In February, results improved recognisably for the aforementioned classes *crops* and *pastures*, while they deteriorate for the other classes. One possible explanation can be found in the ranges used (table 5.6). The class *crops* has the widest range with a span of 0.2 and for *pastures* the span amounts to 0.1. With the ranges being set relatively wide, many pixels fall in between the maximum and minimum, thus leading to a generally higher success rate. To understand this and the rest of the results in table 6.1 better, the distribution of values per date within a class needs to be considered, as the used mean is not very sensitive towards variance and outliers. The following example illustrates this insensitivity of means.

Figure 6.2: Two polygons of the Urban Atlas class *crops*

Source: own illustration

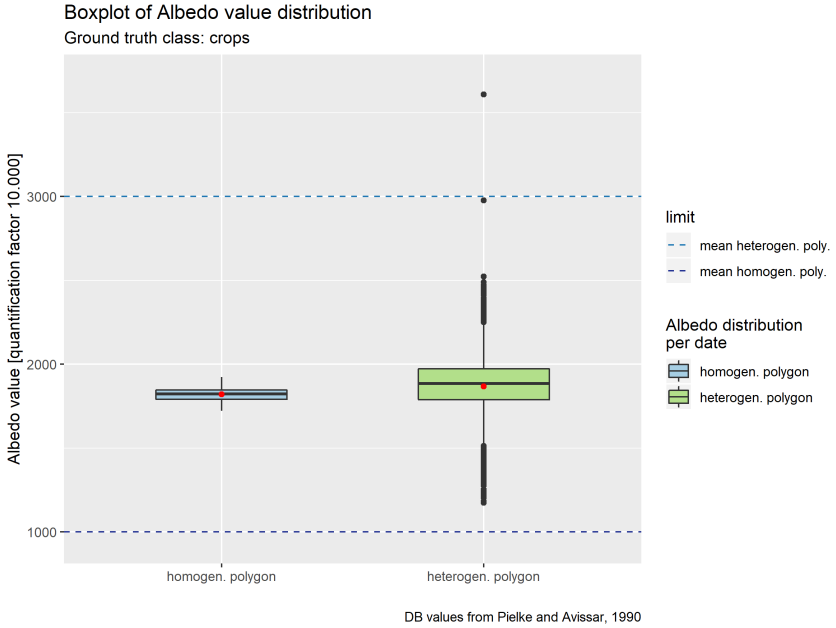

Figure 6.3: Value distribution and mean (red dot) of the two crop polygons from figure 6.2

Source: own illustration

Figure 6.2 shows two different polygons of the class *crops*. The left one is a large polygon, visibly covering several different agricultural fields. The smaller one (right one in the image), covers a single, spectrally homogeneous field. The distribution of albedo values within those two polygons is shown in figure 6.3. While the small, homogeneous polygon (left boxplot in figure 6.3) shows close to no dispersion in albedo values, the large, heterogeneous polygon (right boxplot) has prominently stronger dispersed albedo values. However, both means (indicated in the plot with a red dot) are almost identical and well within the given range from Pielke and Avissar, 1990. Therefore, in order to avoid the minor expressiveness of the mean, boxplots for all pixels per class and dates are created (figures 6.4 to 6.8) to interpret the distribution of values within a class. For better visual interpretation, in a second graphics each boxplot is limited on its y-axis.

The boxplots for the class *urban* (figure 6.4) show many upward outliers. The boxes (a box includes the middle 50% of the data) for the dates between April and August all lie within the expected range (see table 5.6), which is also in agreement with the results connected to the mean albedo in table 6.1. The albedo values from the January scene show the highest dispersion in this class as well as in all the other classes, due to the aforementioned snow cover (figure 6.1). Looking at the boxplot with the truncated y-axis (and disregarding the January scene), a slight seasonal variation in albedo values with lower ranges during winter time and increasing ranges through spring and summer becomes apparent. The boxpots also explain why there is no increase in correctly calculated mean albedo from January to February (table 6.1), despite the large span: while the snow covered polygons in January have values mostly above the maximum stated by Pielke and Avissar, 1990, their snow free albedo values in February are mostly below the minimum, according to the very low sun angle. From table 6.1 it can be seen, that for the class *urban* both dates have approximately 20% of correctly calculated polygons, but the distribution of values is very contrary, a fact which cannot be deducted from the mean alone.

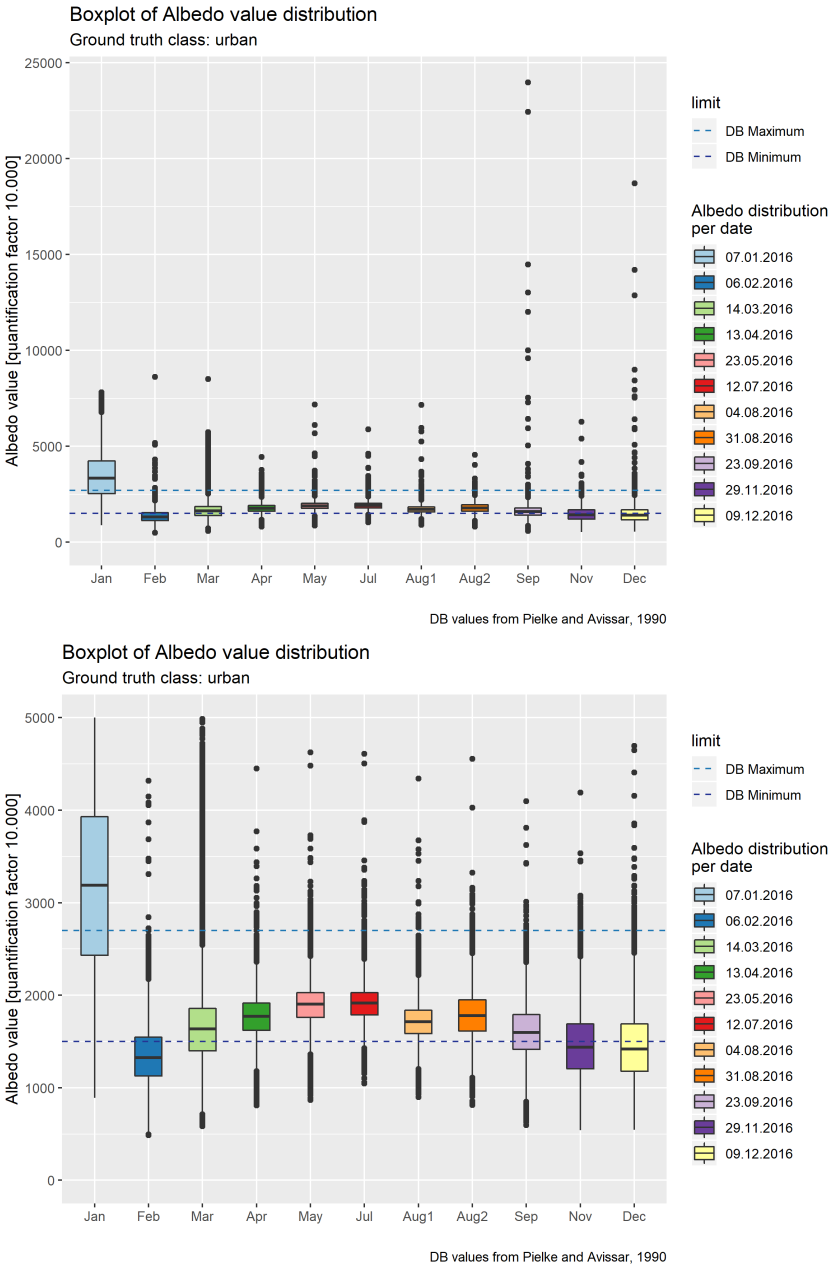

Figure 6.4: Albedo value distribution for the class *urban* without (top) and with (bottom) limited y-axis

Source: own illustration

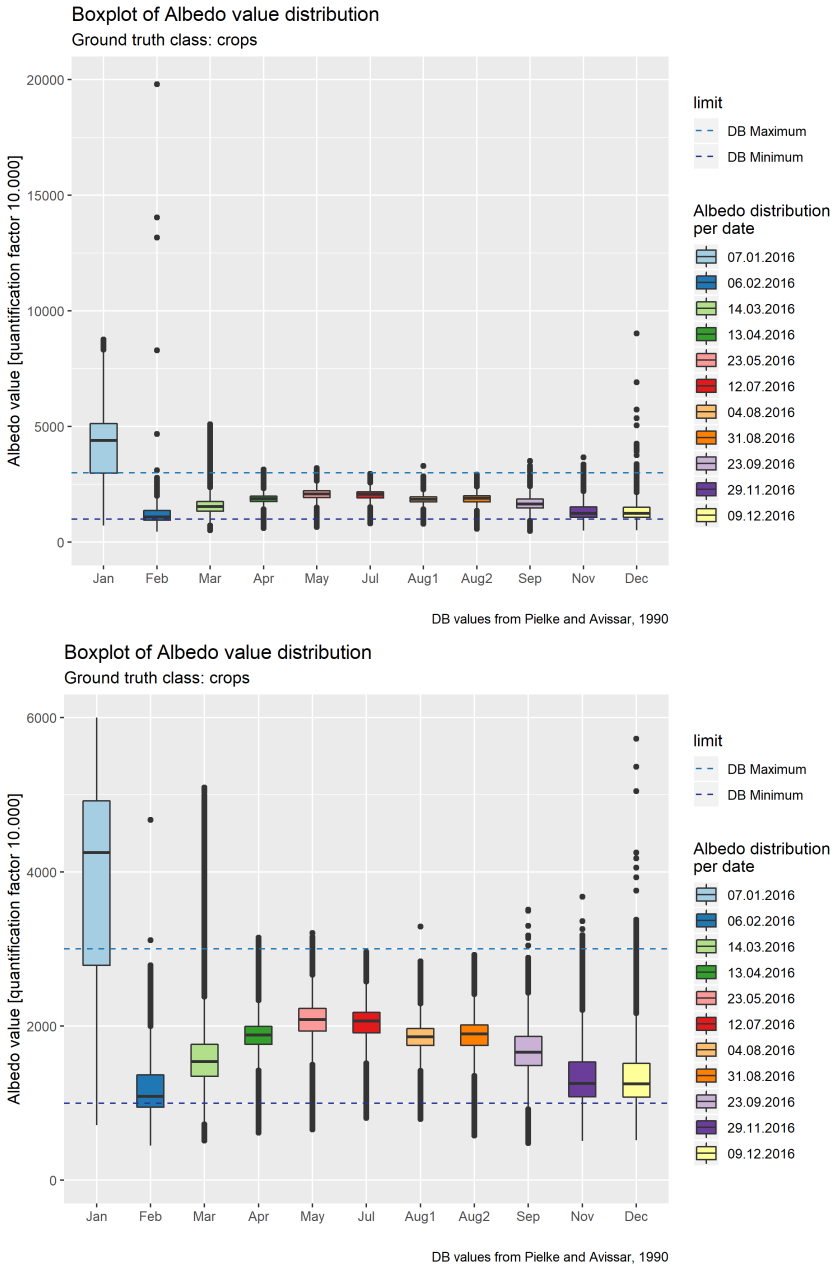

Figure 6.5: Albedo value distribution for the class *crops* without (top) and with (bottom) limited y-axis

Source: own illustration

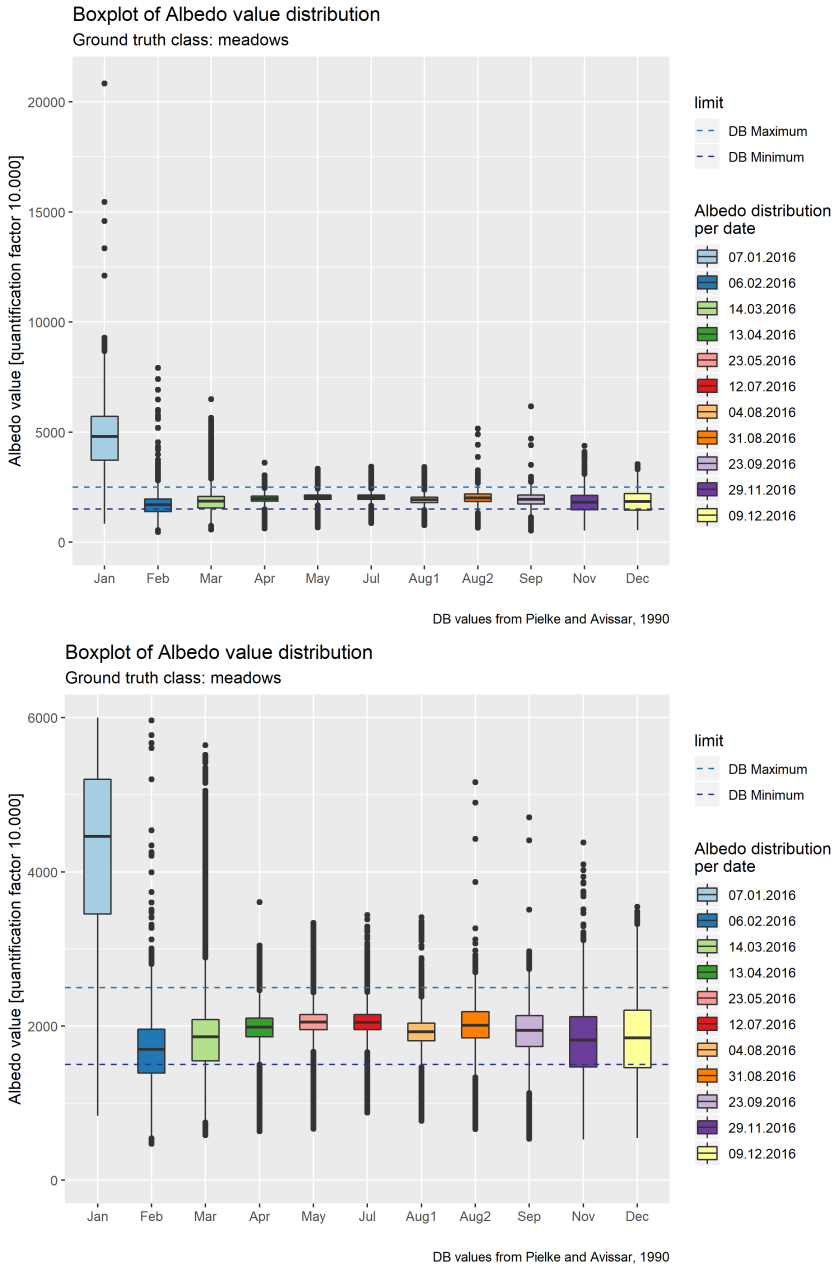

Figure 6.6: Albedo value distribution for the class *meadows* without (top) and with (bottom) limited y-axis

Source: own illustration

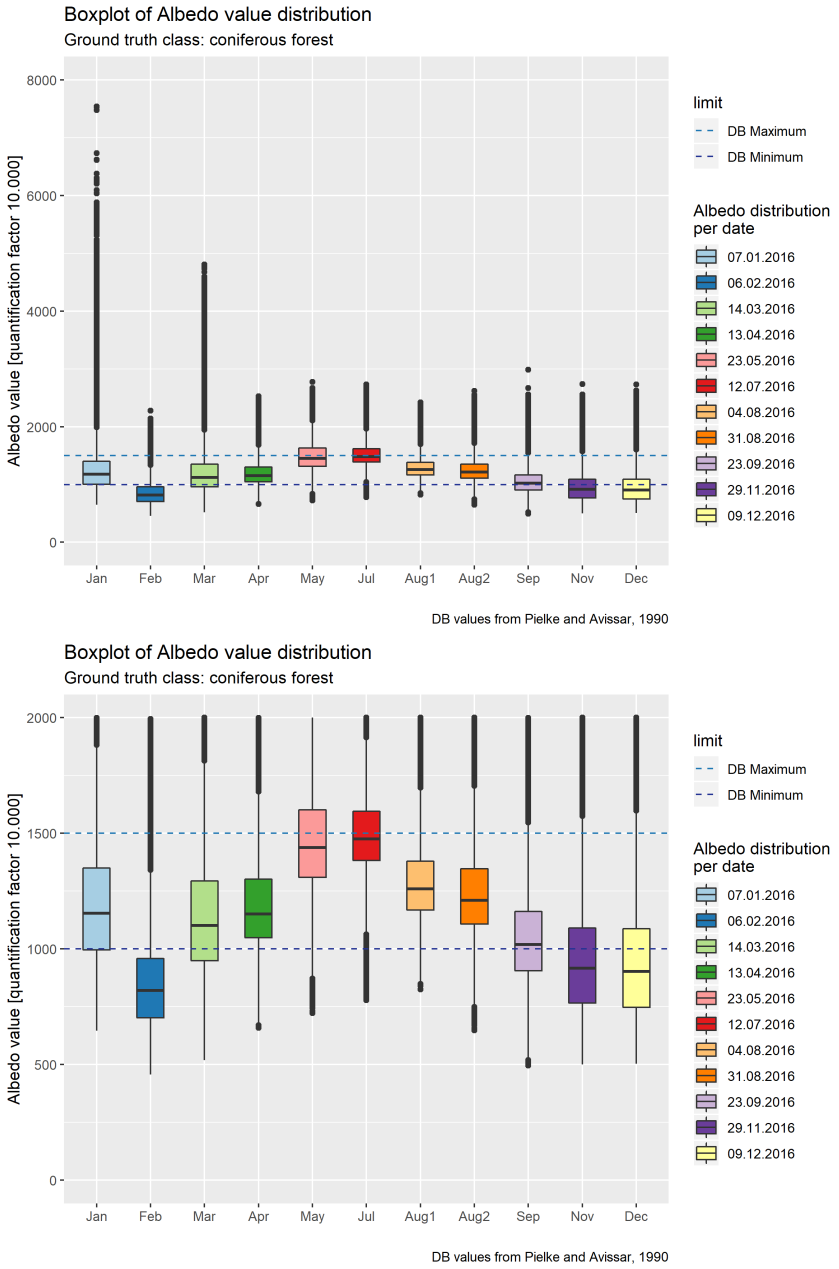

Figure 6.7: Albedo value distribution for the class *coniferous forest* without (top) and with (bottom) limited y-axis

Source: own illustration

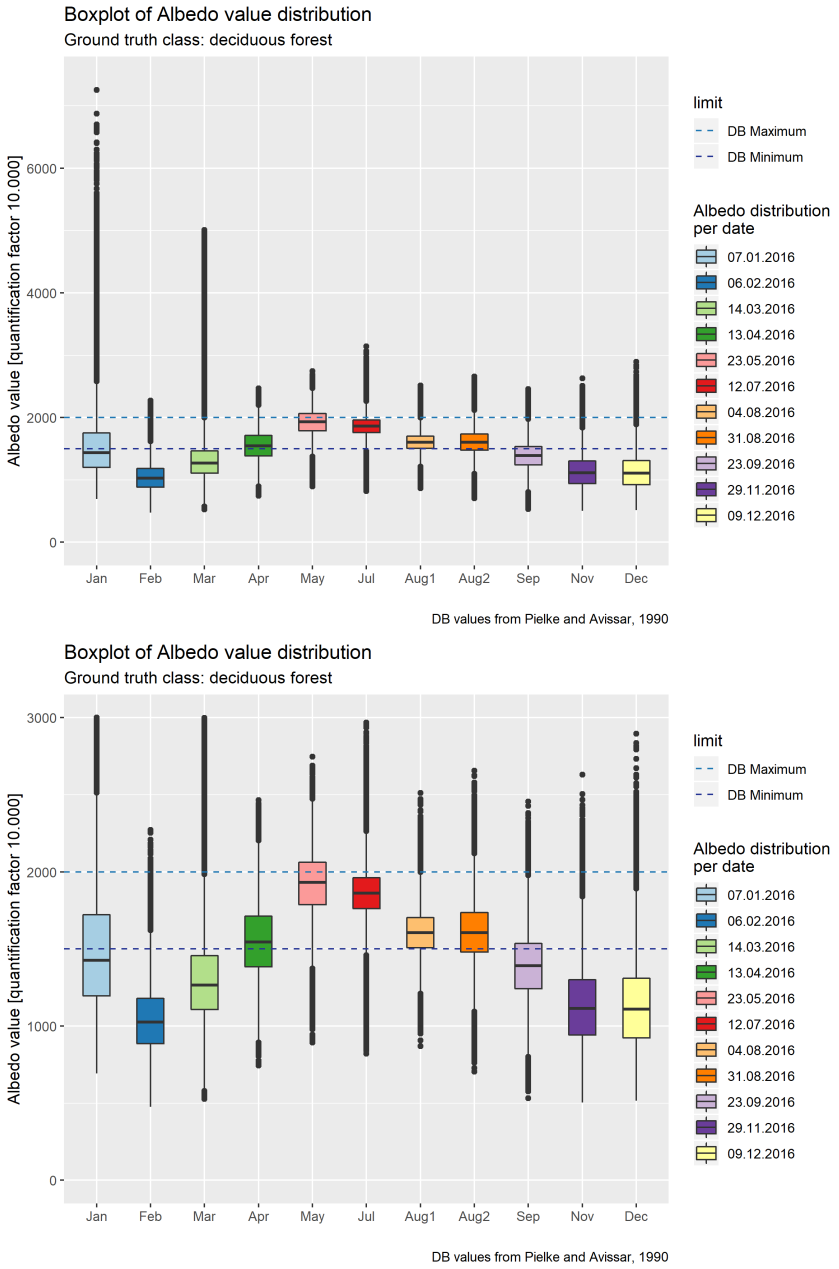

Figure 6.8: Albedo value distribution for the class *deciduous forest* without (top) and with (bottom) limited y-axis

Source: own illustration

The boxplots of the class *crops* (figure 6.5) lie almost entirely within the expected ranges from April up to September, with the dispersion increasing slightly for the September and November scenes. Also for the scenes from February, March, and December the boxplots are within the limits, but with a trend towards the lower end of the expected range and higher dispersion in general, whilst the January scene produces values mostly above the used maximum from Pielke and Avissar, 1990. For this ground truth class a seasonal variation is recognizable as well, when looking at the y-axis-limited boxplot. A very similar result with minimally stronger dispersions throughout the dates is delivered by the class *pastures* (figure 6.6). Examining the boxplot with the truncated y-axis (figure 6.6, bottom), a less pronounced seasonal variation in albedo values can be detected. From January to March and November to December a stronger dispersion of values is evident from larger boxes and a higher number of outliers.
In comparison to the previous three classes, the classes *coniferous forest* and *deciduous forest* (figures 6.7 and 6.8) both show a much stronger seasonal variation in albedo values. Disregarding the January scene, an increase through spring, reaching its highest values in summer above the given range from Pielke and Avissar, 1990, and a decrease through autumn and winter can be seen for both forest classes. This becomes even more apparent when looking at the two bottom boxplots with the truncated y-axes. They both have the most upward outliers in all the dates, especially in the March scene and *deciduous forest* has noticeably more downward outliers compared to *coniferous forest*.

Next to snow cover, other factors, such as the solar zenith angle or atmospheric conditions like water-vapour content and precipitation (Cescatti et al., 2012; Román et al., 2009; Ollinger et al., 2008, see chapter 2.1), have an influence on albedo measurements. All of these variables change throughout the course of a year and with them, the measured surface albedo changes. These seasonal variations are visible in all boxplots (figures 6.4 to 6.8). Typical ranges of albedo for a ground cover type, however, cannot portray this seasonal variation, when there is no information given on when which end of the range has to be used. Therefore they appear not to be a suitable tool, to validate the results of a time series covering all seasons, as it could not be retraced from Pielke and Avissar, 1990, for which time of year these albedo ranges apply. Generalising, it can be deducted, that the chosen method of calculating albedo is applicable for

the timespan of April to September for the classes *urban*, *crops*, and *meadows* and only for August for the classes *coniferous forest* and *deciduous forest*. Comparing the results within one date, the albedo is expected to be lowest for coniferous forest and increase with the classes deciduous forest, meadows and crops (valid for summer; Coakley, 2003). Figure 6.9 shows the albedo value distribution for these four classes for scene 6 (12.07.2016) and the mean increase from class to class is clearly visible (similar plots for different dates can be seen in the Appendix).

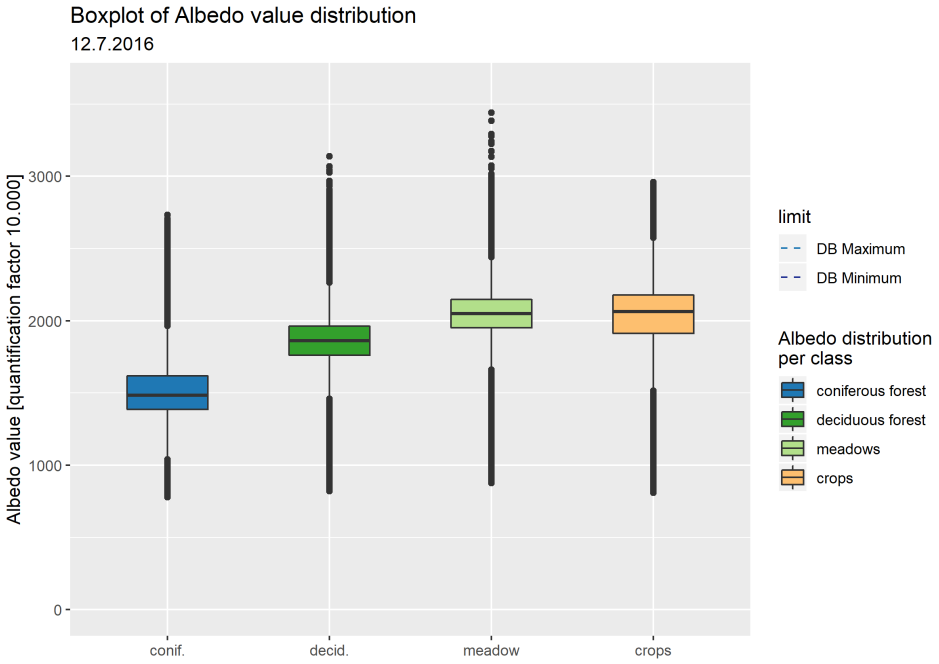

Figure 6.9: Comparison of albedo value distribution for different classes

Source: own illustration

Finally, the course of the variation needs to be examined. Consulting the literature, some sources describe higher albedos in winter than in summer, while other sources describe the opposite for the same cover type. Jong, 1973 states, that albedo changes with the altitude of the sun. At a lower sun altitude (such as in the morning and evening or generally in winter) the sun

rays supposedly penetrate less into the surface and a larger fraction of the incoming radiation is reflected, thus leading to a higher albedo, as opposed to lower albedo at higher sun altitudes (Jong, 1973). Considering, that a beam of solar radiation is subject to much higher scattering at lower sun angles and at the same time covers a larger area than at higher sun angles (Gebhardt et al., 2007), Jong's remarks should be treated with reserve. Coakley, 2003 also lists slightly higher albedo values for winter compared to summer albedo for the classes *evergreen forest (needle leaved)* and *deciduous forest* but vice versa for *short grassland, meadow and shrubland*. Other sources also attribute higher albedo values to the winter season for the classes *water* (Cogley, 1979) and *evergreen needleleaf forests, open shrublands, and barren or sparsely vegetated surfaces* (Zhou et al., 2003), or for global albedo (Stephens et al., 2015). These sources do not state clearly, if a present snow cover is responsible for higher winter albedos. Different sources indicate higher summer albedos (as opposed to snow-free winter albedos) for certain cover types, such as *deciduous and mixed forest*, but propose conversed albedo values for cover types like *crops/corn field* (Robinson and Kukla, 1984; Myhre, Kvalevag, and Schaaf, 2005), which is contradictory to Coakley, 2003. Rechid, Raddatz, and Jacob, 2008 propose generally higher albedo values for European land surfaces in summer contrary to snow-free winter. It is evident, that snow cover increases the albedo of a surface significantly (e.g. Kuusinen et al., 2014; Robinson and Kukla, 1984; Hovi et al., 2019), but if the albedo of the same surface is higher in snow-free conditions in winter is not unambiguously verifiable from the investigated sources. However, in the case of no snow cover present, the albedo of a surface is expected to be higher in summer than in winter, because of the changing incidence angle during the course of a year, and all boxplots reflect this behaviour.

A few comments also need to be addressed towards the used validation dataset, the Urban Atlas classification. Firstly, the time difference between the acquisition date of the satellite images the albedo values are calculated from and the date the validation dataset was generated has to be considered. The albedo was calculated from Sentinel-2 scenes of the year 2016 whereas the validation dataset is comprised of the Urban Atlas classification from 2012 (Copernicus, 2019b) and the LiDAR-derived forest map from 2015 (Bauer et al., 2015). Any changes, which might have occurred between the classifications and the time of collection of the scene are not accounted for and could therefore possibly lead to

a bias in the results. Additionally to the time difference, the spatial resolutions between the datasets deviate. The Sentinel-2 scenes come at a spatial resolution of 10 m, while the Urban Atlas classification is derived from 20 m resolution data and the LiDAR-based forest map from 20 cm resolution data.
Figure 6.10 illustrates this potential bias owed to time of data creation with two examples for the case of the Urban Atlas classes *crops* and *urban*. The polygon in the left extract, attributed to the class *crops*, covers a small water body. The example on the right shows a polygon of the class *urban* covering a vegetated area. Both changes possibly occurred between the time of the Urban Atlas classification (2012) and the Sentinel-2 data acquisition date (2016). An example for a possible spatial resolution bias is shown in figure 6.11. The highlighted polygons of the class *crops* overlap into some pixels of the ground cover forest. As the extent of those forest pixels might fall below the minimal mapping unit of the Urban Atlas classification, they are not gathered as a separate class, but rather included in a neighbouring class, following a chosen classification algorithm. These considerations need to be kept in mind when analysing the results derived from the Urban Atlas classification.

Coming back to the results of this thesis, the snow cover in January is clearly evident, and higher albedos due to the snow cover are easily accountable. It can be deducted, that the chosen method to calculate albedo is sensitive to snow cover and generally delivers higher albedos for snow covered surfaces. For the rest of the dates, the trend is reversed: calculated albedos in summer tend to be higher than in winter. This trend is expected, however, the findings in the technical literature concerning the seasonal variation in albedo are ambiguous. In conclusion, Liang's approach of a band weighting function produces results in agreement with cover type dependent albedo ranges found in literature when constricting the input data to summer scenes. The weighting function reflects the expected relationship of albedo between different classes correctly (see figure 6.9). In order to make a statement about the suitability of the method for winter or the seasonal variation of albedo, additional information, like ground based measurements and reference albedo values linked to a season, would be needed.

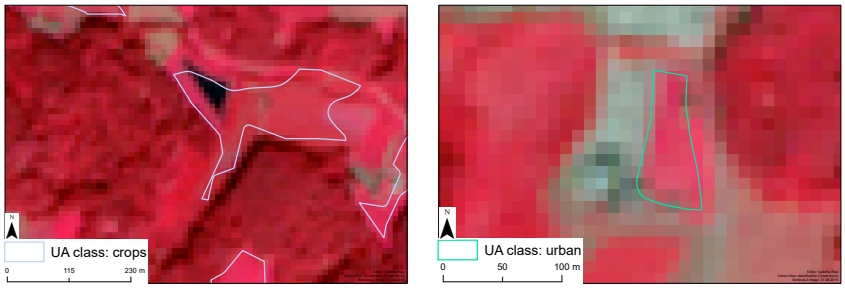

Figure 6.10: Time of data creation induced error between Sentinel-2 data (scene from 31.08.2016) and Urban Atlas classification

Source: own illustration

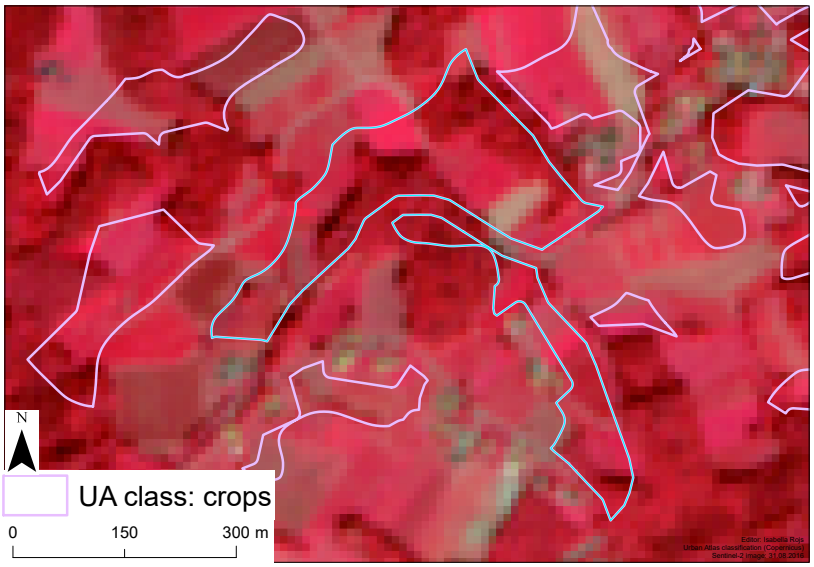

Figure 6.11: Spatial resolution difference induced error between Sentinel-2 data (scene from 31.08.2016) and Urban Atlas classification

Source: own illustration

6.2 Results and discussion of FVC plausibility analysis

With a mask representing 100% soil sealing, derived from the soil sealing map of Graz (Graz, 2019) as described in chapter 5.5.2, values are extracted from the FVC calculations. These values are plotted in density histograms with a bin width of 0.01 to visualise the relative frequency of value distribution. As the reference is a fully sealed surface, values in the calculations are expected to be 0, or as low as possible. Figures 6.12 to 6.15 show these histograms for each of the four investigated dates (12.07.2016, 04.08.2016, 31.08.2016, 23.09.2016) and the three used indices (GVI, MSAVI, NDVI). Additionally, the mean is also plotted into each histogram and all means are summarised in table 6.2. The mean is also expected to be as close to 0 as possible. Table 6.2 also includes the relative frequency of the first bin of the histogram. It describes the relative amount of values, compared to all values, with a calculated FVC of 0. As the bin width is set to 0.01, the value can be equated with the percentage of correctly calculated values.

Table 6.2: Mean FVC per index and date

index	*date*	*mean*	*ratio in first bin*
GVI	12.07.2016	0.0187	0.82
	04.08.2016	0.0865	0.39
	31.08.2016	0.0704	0.32
	23.09.2016	0.0516	0.45
MSAVI	12.07.2016	0.0371	0.80
	04.08.2016	0.0548	0.68
	31.08.2016	0.0737	0.58
	23.09.2016	0.0718	0.57
NDVI	12.07.2016	0.0285	0.85
	04.08.2016	0.0489	0.65
	31.08.2016	0.0491	0.70
	23.09.2016	0.0511	0.66

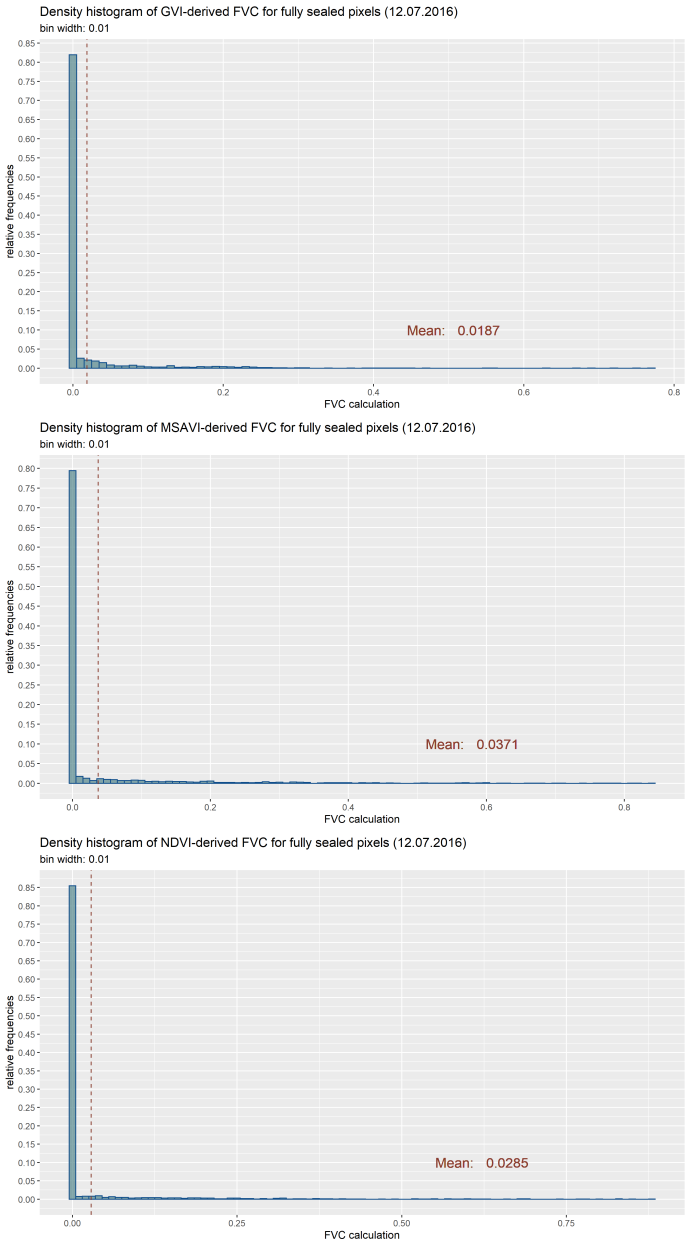

Figure 6.12: Density histogram for scene 6 (12.07.2016): FVC from GVI (top), MSAVI (center), and NDVI (bottom)

Source: own illustration

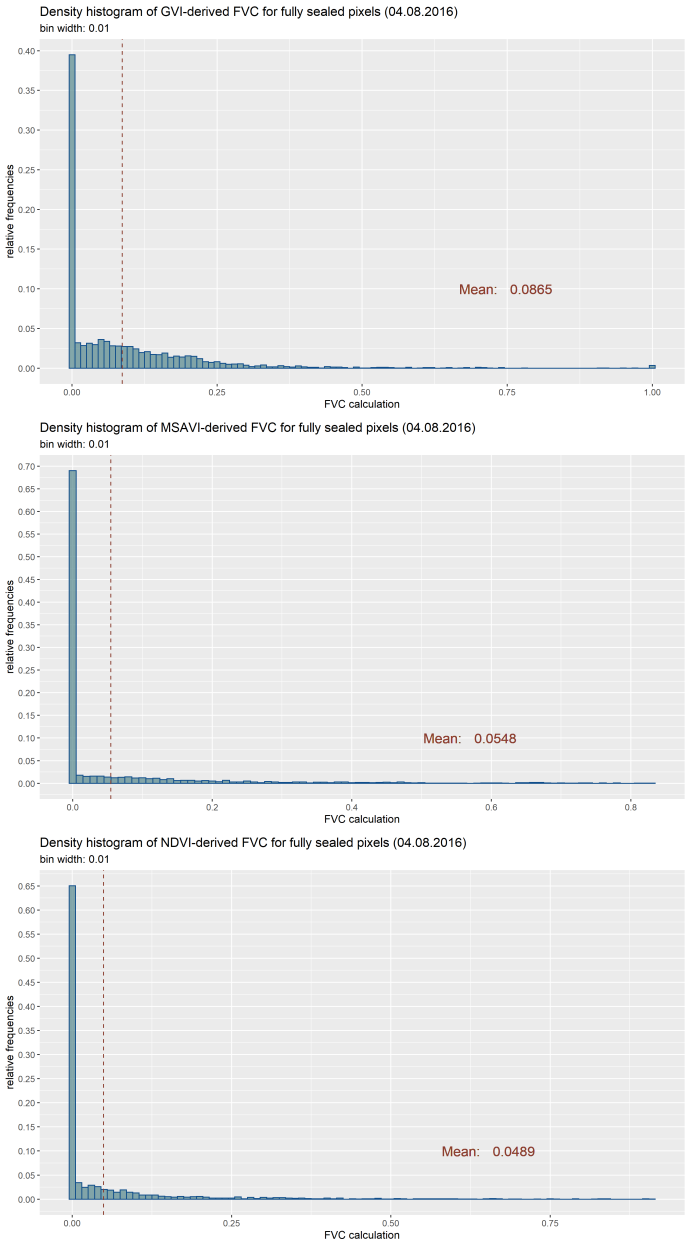

Figure 6.13: Density histogram for scene 7 (04.08.2016): FVC from GVI (top), MSAVI (center), and NDVI (bottom)

Source: own illustration

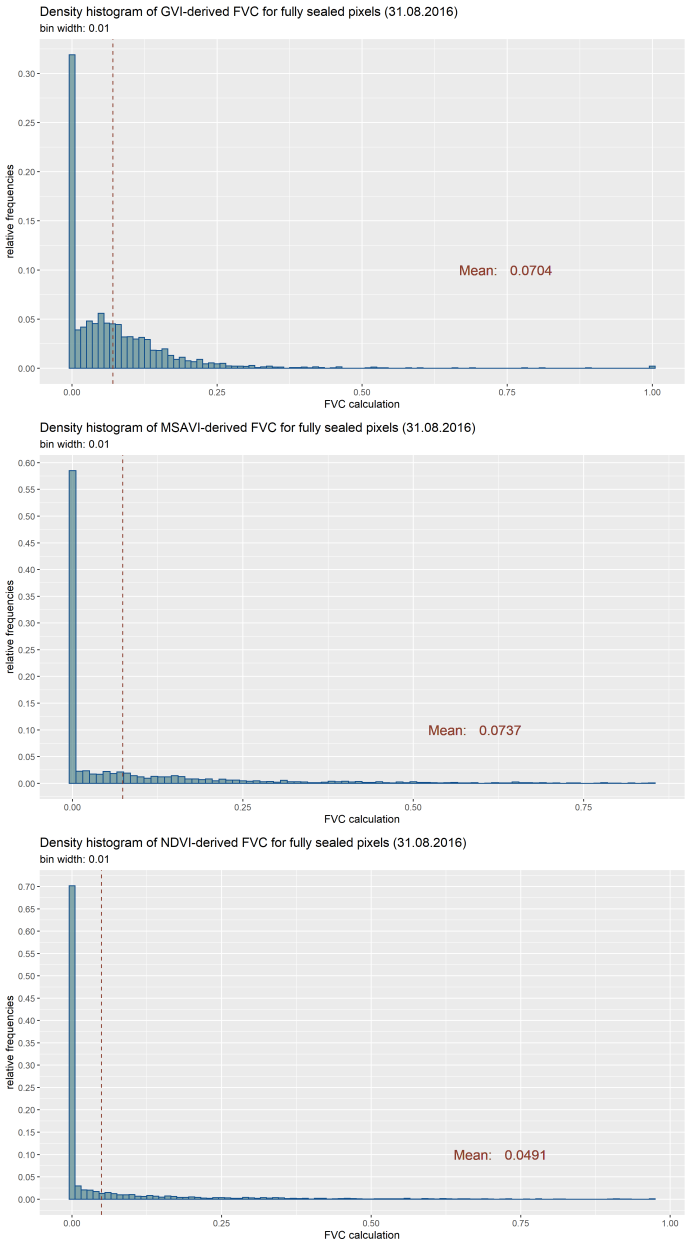

Figure 6.14: Density histogram for scene 8 (31.08.2016): FVC from GVI (top), MSAVI (center), and NDVI (bottom)

Source: own illustration

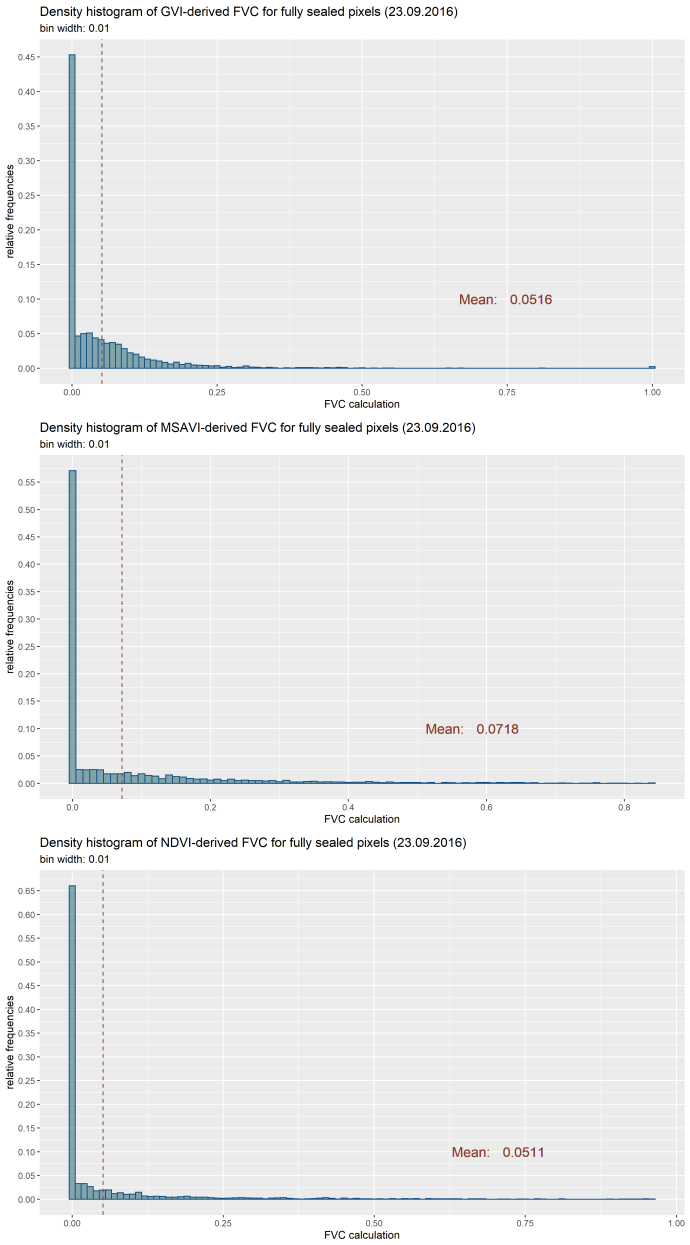

Figure 6.15: Density histogram for scene 9 (23.09.2016): FVC from GVI (top), MSAVI (center), and NDVI (bottom)

Source: own illustration

The best result is achieved with the GVI-derived FVC on scene 6 (12.07.2016) with 1.87% vegetation cover on average, while the poorest results are also achieved with GVI-derived FVC for scene 7 (04.08.2016) with 8.85%. NDVI has a higher percentage of correctly calculated values for scene 6 (85%) compared to GVI for the same date (82%) but a lower mean (2.85%). All results are well below a mean of 10% with scene 6 reaching the lowest mean per index. Scene 6 also has the highest percentage of correctly calculated values in all dates (above 80%). For all dates, apart from 12.07.2016 (scene 6), NDVI scores the best results with means at approximately 5% per date. Results for MSAVI and NDVI deteriorate (slightly) from scene to scene, while results for GVI drop to the lowest score for scene 7 and then improve again. Comparing the indices per date, MSAVI produces the lowest accuracy in all dates, except for scene 7 (04.08.2016), where GVI scores the poorest results. Overall, the achieved results look promising but their significance needs to be questioned.

The selection of the two scaling parameters in the regression method, VI_v and VI_s, is a crucial step in applying this approach, as described in chapter 2.2. The procedure for deriving VI_v, detailed in chapter 5.3, relies on the LiDAR-based forest mask. Based on the attribute *crown closure*, fully vegetated polygons are identified and their mean delivers VI_v for each scene. The choice of forest as a basis for VI_v determination can be problematic. Looking at the equation (5.8) to calculate FVC, the higher the value for VI_v, the lower the resulting FVC value. Grass, which can have a higher NDVI than forest, might produce a different result, if used for the determination of VI_v. As there is not a lot of forest present in the investigated extent of the scene (for extent see figure 5.9), this might distort the results. Also the fact, that there was no ground truth available for the selection of VI_s is a possible source of error. Ideally VI_v and VI_s would be selected from a field campaign during the same time of the acquisition dates of the sensor data, or through the aid of high resolution satellite or airborne images. When analysing time series, like in this thesis, it needs to be ensured that the selected areas are fully vegetated (VI_v) or completely free of vegetation (VI_s) for all investigated dates.

The reference data only gives information on 100% soil sealing, so merely the low end of value ranges of the calculations can be analysed. Following table 6.2, the regression method of scaling a Vegetation Index appears to be a suitable

tool to detect soil sealing. However, due to the lack of suitable reference data, no analysis can be conducted regarding the high end of values and the fraction of mixed pixels, which would be most interesting and crucial for a true verification of the method. The successful application of this method in various studies has been described in chapter 2.2, therefore adequate results for vegetated surfaces are expected for this thesis' Sentinel-2 data and study area, but further testing with more appropriate reference data is still needed.

6.3 Results and discussion of LAI plausibility analysis

Following the applied methods, this section will discuss the results for *forest* (chapter 6.3.1) and *crops* (chapter 6.3.2) separately. Similar to albedo, LAI values from databases are available for several land cover types. From Iio and Ito, 2014, all entries for spruce and pine (for coniferous forest) and beech and oak (for deciduous forest) from Austria and Germany are used, to determine the range of possible LAI values. Scurlock, Asner, and Gower, 2001 provide the data for the crop types maize and wheat. To perform plausibility tests, ground truth data is used as described in chapter 5.5.3. It was ensured that no cloud cover is present at any time of the used scenes in the area of interest.
In chapter 6.1 the limits of using a mean value for the plausibility analysis (of albedo results) was discussed. Therefore it was decided to focus only on value distribution in this chapter for LAI tests. As described in chapter 5.5.3, additional information from the forest mask on age class allow for further analysis of the LAI results.

6.3.1 Forest

In the first part of this chapter, the results for each of the three approaches are presented, discussed and compared. In a second part, the results for forest LAI are connected to the parameter age class.

Part I

Approach 1

Chen and Cihlar, 1996 established different empirical relationships (linear and exponential) between their LAI ground measurements of coniferous forest and two indices (NDVI and SR) for late spring and mid-summer (see equations 5.9 to 5.16). Their methods are applied to scenes 5 (23.05.2016) and 6 (12.07.2016) respectively. The results for these scenes can be seen in figure 6.16. In general, LAI derived from SR shows more strongly dispersed values compared to NDVI-derived results in both dates. The exponential relationships create higher LAI values on average, than the linear relationships and the effect is prominently visible in late spring (top figure). While the exponential relationship derived from SR for late spring lies mostly outside the given range, all the other combinations seem to match the database value ranges. For coniferous forest stands, the LAI throughout the year is expected to stay relatively constant on one level (Rautiainen, Heiskanen, and Korhonen, 2012), therefore value ranges from databases can be a suitable tool to verify coniferous LAI calculations.

Apart from the addressed SR-outlier, the results suggest that this approach by Chen and Cihlar, 1996 is applicable to the study area with the used sensor. It should be mentioned, however, that the best result in terms of R^2 by Chen and Cihlar, 1996 was accomplished with the exponential regression from SR for late spring, which performed the poorest in this setting.
Considering the seasonal variation of LAI and VIs, the strength of the method probably lies within the consideration of phenology status of forests (separate regression functions for spring and summer). However, further tests for multiple years would be necessary to confirm this statement. With the Sentinel-2 mission constellation of two satellites, cloud-free time series are more probable and facilitate additional testing in the future.

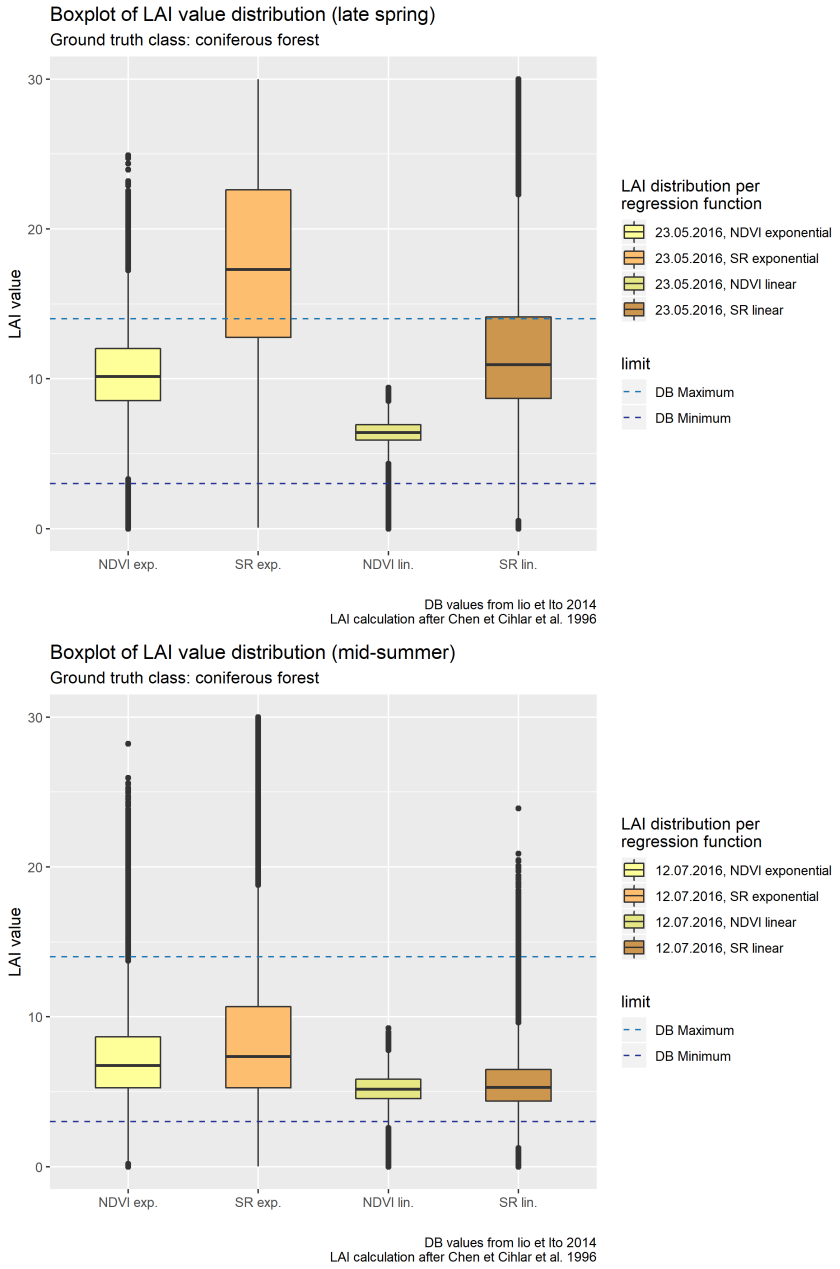

Figure 6.16: LAI value distribution for the class *coniferous forest* for late spring (left) and mid-summer (right), after Chen and Cihlar, 1996

Source: own illustration

Approach 2
Bach et al., 2003 used exponential regression functions (after Gregoire and Raffy, 1997) based on the NDVI for several land cover classes, considering *coniferous forest* (equation 5.17) and *deciduous forest* (equation 5.18). In their study, they applied these equations to a scene from May and one from October, so it was decided to test this method on scenes 3 (14.03.2016) (a scene before the leafing phase, to show the strong influence of the leaf production phase in deciduous forests) to 9 (23.09.2016) (with the October scenes being too clouded in most parts to use). Figure 6.17 (top figure) depicts the LAI value distribution as boxplots for the class *coniferous forest* calculated after Gregoire and Raffy, 1997 (as cited in Bach et al., 2003). The values show a strong dispersion between months and the regression formula highly overestimates for August and September and slightly for May, in relation to the limits taken from Iio and Ito, 2014. For the months March, April and July the values are in agreement with the proposed ranges found in literature related to terrestrial measurements. As stated above, the LAI for coniferous forest stands is expected to be relatively constant in the course of the seasons (Rautiainen, Heiskanen, and Korhonen, 2012), and method 2 does not reflect that. The method seems to be unsuitable for late summer and early autumn (scenes 8 and 9). As stated in chapter 5.4.1, Bach et al., 2003 merely applied the regression functions to improve their hydrological model, and did not perform any ground measurements of LAI to test their methods. The publication they refer to (Gregoire and Raffy, 1997) could not be accessed, so no statement can be made about the circumstances under which this empirical relationship was formed and the applicability to this thesis's settings. The results for May fall out of line with generally higher values compared to the previous and following scene.

One explanation for the irregular results in May could be some unexpected heterogeneous surfaces in the coniferous forest, discovered in the NIR band, which is used to calculate this LAI. In figure 6.18, an extract of coniferous forest is shown for scene 5 (23.05.2016) for the bands Red, NIR, Vegetation Red Edge and SWIR ((a)-(d)). While the surface looks homogeneous in the Red band (a), it is much more heterogeneous in the NIR (b) and Vegetation Red Edge band (c). The effect is less pronounced in the SWIR band (d). This could be attributed to cut or fallen trees, or other natural causes. Broadleaved trees among the coniferous stand could also be a possible cause for this effect,

which is visible throughout the entire scene over coniferous forest. It could also be an explanation for the upward outlier of Chen and Cihlar's method of the exponential regression from SR for late spring (figure 6.16, top).

For deciduous forest (figure 6.17, bottom) an increase in LAI from March to May is clearly visible. Between May and September the LAI is constant at approximately 6, with values being generally slightly higher in May. Also, the values in those four months lie mostly within the expected range. The increase of LAI of deciduous forest in spring is connected to the leaf production phase and is also noted by several publications (e.g. Rautiainen, Heiskanen, and Korhonen, 2012; Simpraga et al., 2011; Campioli et al., 2011). LAI values above 0 during that time can be accounted to understory vegetation, that is visible through the leaf-less trees. Rautiainen, Heiskanen, and Korhonen, 2012, Simpraga et al., 2011, and Campioli et al., 2011 describe a bell-shaped development of LAI values throughout the year, with a strong increase of LAI in the leaf production phase, constant LAI in the leaf maturity phase and a sharp drop in the phase of leaf senescence. This trajectory is also recognisable in figure 6.17 (bottom) up to the leaf maturity phase (May - September). The start and end of the phases differ between publications and are of course depending on tree species and biogeographical regions. In the publication of Campioli et al., 2011, a beech tree site in Hessen, Germany, is investigated and the start of the LAI increase as well as the values reached during leaf maturity phase (around 6) coincide with the obtained results in this thesis. The slightly higher values in May could be attributed to the same noise as described in the previous paragraph. However, the effect in deciduous forest is much less pronounced and does not distort the visual result as much as with coniferous forest. Summarising, the method appears to work well for deciduous forest, especially during leaf maturity phase.

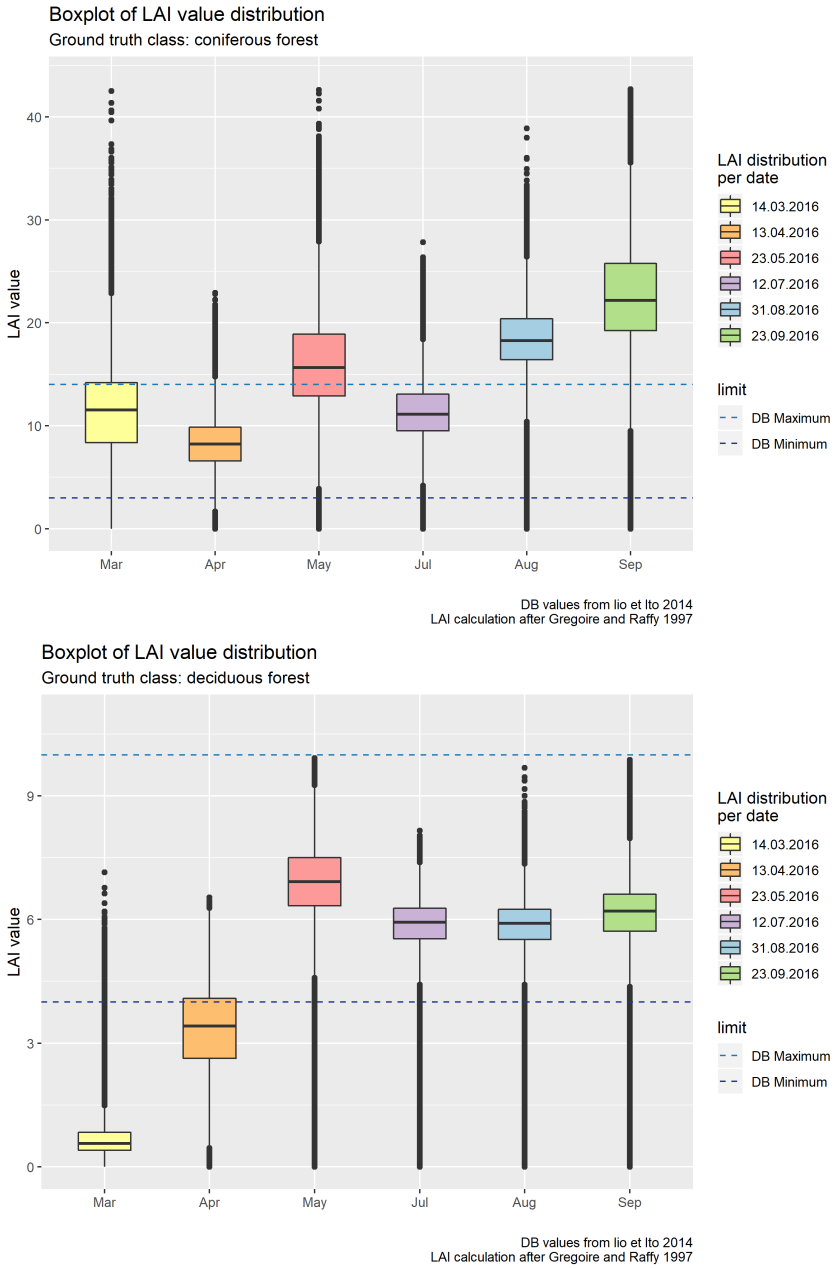

Figure 6.17: LAI value distribution for the class *coniferous forest* (top) and *deciduous forest* (bottom) after Gregoire and Raffy, 1997 (as cited in Bach et al., 2003)

Source: own illustration

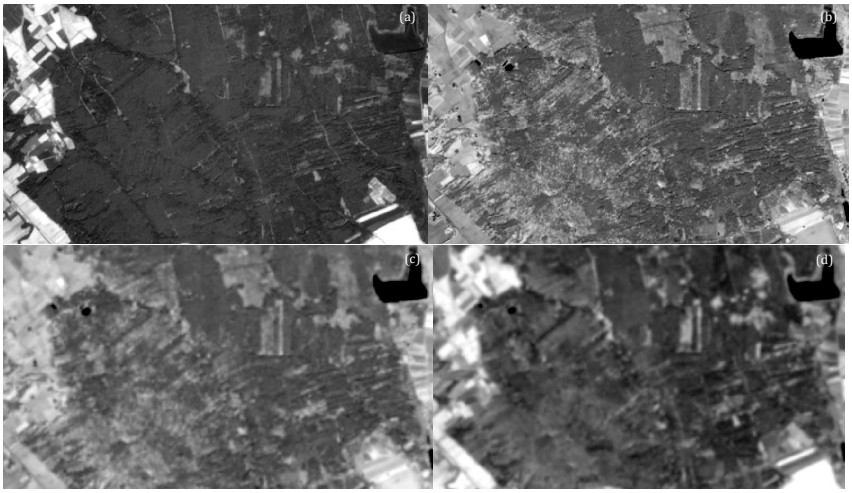

Figure 6.18: May scene: Band 3 - Red (a), Band 4 - NIR (b), Band 6 - Vegetation Red Edge 2 (c), Band 11 - SWIR 1 (d)

Source: own illustration

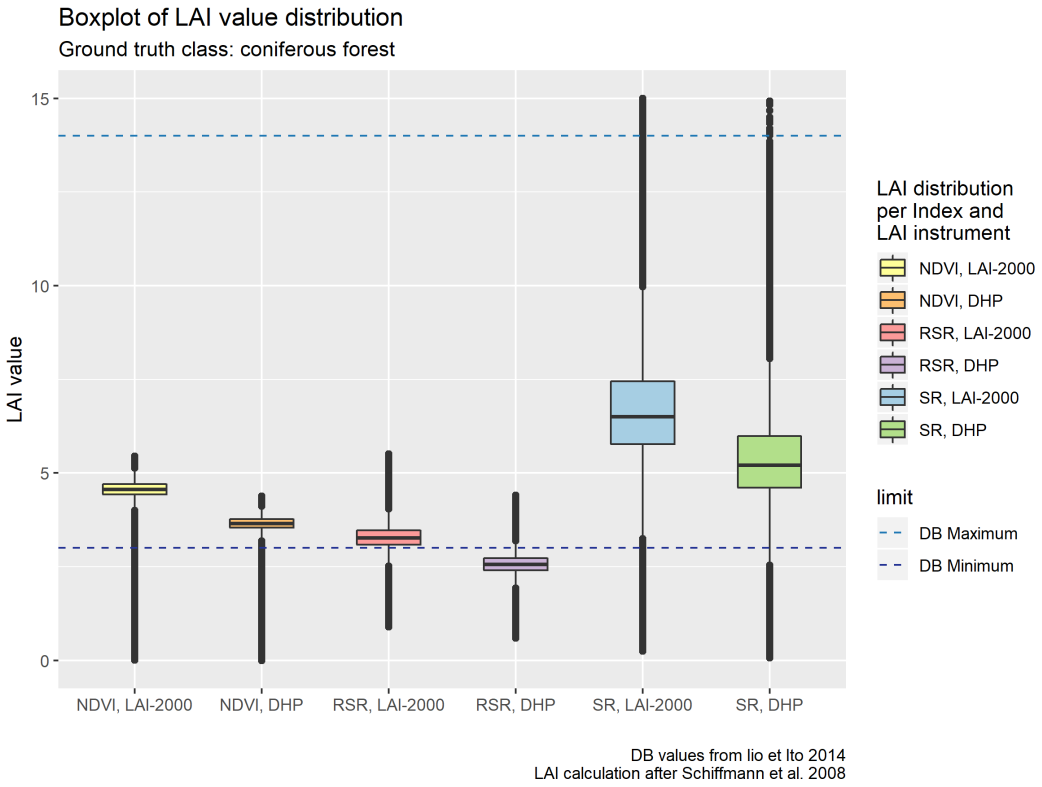

Figure 6.19: LAI value distribution for the class *coniferous forest* after Schiffmann et al., 2008

Source: own illustration

Approach 3
Schiffmann et al., 2008 compared three different indices with two different measurement methods for LAI (see chapter 5.4.1, equations 5.19 to 5.24). In their study, LAI derived from RSR compared to LAI measurements from DHP scored the best results in the regression analysis ($R^2 = 0.83, RMSE = 0.64$). The different regression functions established by Schiffmann et al., 2008 were applied to scene 6 (12.07.2016), as the publication used a Landsat TM scene from July, and the results are shown in figure 6.19. The y-axis was truncated for better visibility. As already observed for the method of Chen and Cihlar, 1996, the SR-derived LAI values are more strongly dispersed and delivers generally higher values in comparison to NDVI and also RSR. Overall, the regression functions based on the LAI-2000 plant canopy analyzer produce higher LAI than from DHP. Looking at the ranges, provided by terrestrial LAI measurements found in literature, LAI derived from RSR using DHP is the only one dropping below the minimal value of terrestrial measurements (Iio and Ito, 2014). This result is contrary to the findings of Schiffmann et al., 2008, who obtained the best results with this approach. For the remaining regression functions, no statement can be made about one being better suitable than the other, as they all lie within the very widely set range and no real ground truth measurements are available.

Figure 6.20 shows a comparison of all methods, applicable to calculate LAI for coniferous forest for summer. It combines all results from figures 6.16 (bottom), 6.17 (top), and 6.19. Again, the y-axis was limited for better visual interpretation. Apart from the RSR-derived LAI by Schiffmann et al., 2008, which falls below the minimum found in the database (Iio and Ito, 2014), all methods produce LAI values (mostly) within the expected range. Outliers can be attributed to the time difference between the ground truth data (2015 for forest) and the remote sensing data (2016), cloud cover or shadow, or mixed pixels at the border to other ground cover classes. Despite taking care to avoid pixels that could be affected by the mentioned conditions, errors in the automated selection process of ground truth data cannot be discarded. Again, no statement can be made about one method being superior to the other. It appears, however, that LAI values below 5, as produced through four of the six methods by Schiffmann et al., 2008 (boxplots F, G, H, I in figure 6.20), are to be expected in coniferous forest sites in boreal (e.g. Pope and Treitz,

2013; Aubin, Beaudet, and Messier, 2000) or mountainous (e.g. Kantor, Sach, and Cernohous, 2009; Sterba, Dirnberger, and Ritter, 2018) regions, and values above 5 in regions similar to this study area (e.g. DeRose and Seymour, 2010; Turner et al., 1999). Schiffmann et al., 2008 conducted their study in Yosemite National Park, which is located in the Sierra Nevada Mountains (USA), a highly mountainous site. Applying their methods to the study area of this thesis emphasises the strong study-specific dependency of regression functions.

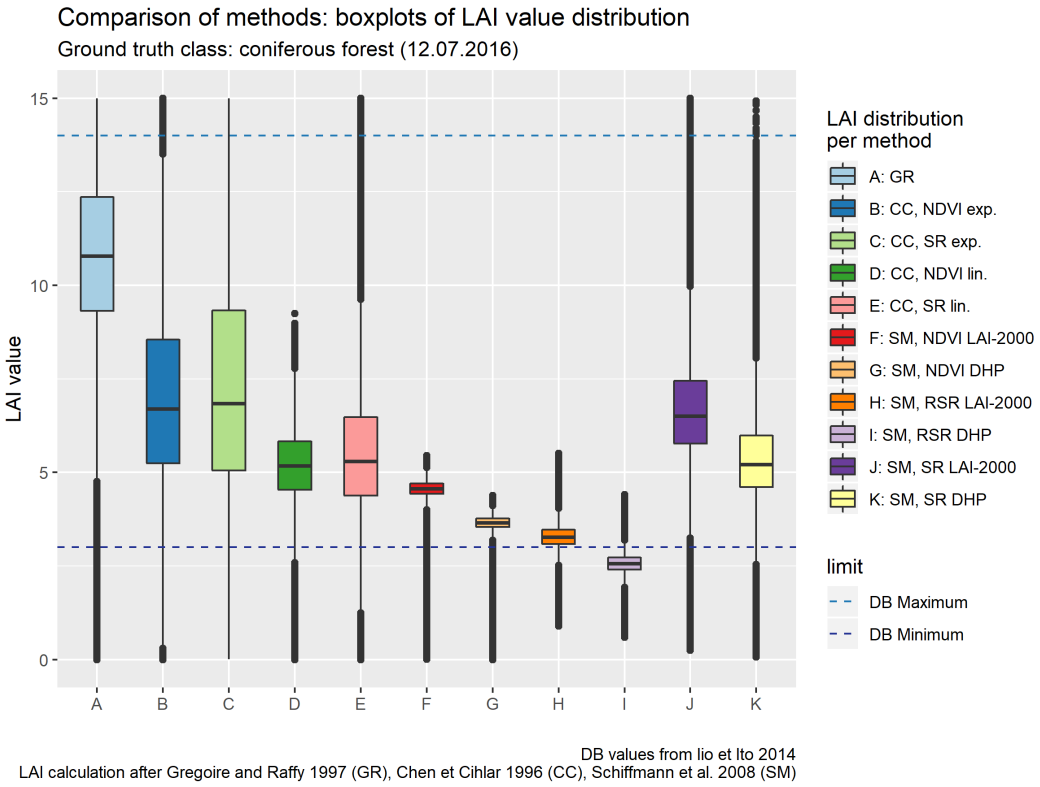

Figure 6.20: Comparison of all methods for coniferous forest for July scene

Source: own illustration

Part II

In this part the relationship between LAI and different age-related attributes of forest are investigated. The findings in the literature are connected to the available information on age class from the LiDAR-based forest map. The aim is to find out, if the tested methods reflect the expected behaviour of LAI in connection to age class.

In literature, the relationship between LAI and stand age is well documented. In the first period of growing the leaf area of a stand increases significantly until it reaches its peak (Leuschner et al., 2006; Pokorny and Stojnic, 2012; Kantor, Sach, and Cernohous, 2009; Ryan et al., 1997, as cited in Leuschner et al., 2006). While „fast-growing“ trees (such as Norway spruce) reach their maximum LAI at an age of 10 - 15 years (Pokorny and Stojnic, 2012), „slow-growing“ trees (such as certain pine species) peak between 20 and 40 years of age (Long an Smith, 1992, as cited in Vose et al., 1994; Schlerf, Atzberger, and Hill, 2005). After a stand reached its peak, LAI either slowly declines or fluctuates around a natural equilibrium value - this applies to coniferous as well as deciduous forest stands (Pokorny and Stojnic, 2012; Battaglia et al., 1998; Sonohat, Balandier, and Ruchaud, 2004; Köstner, Falge, and Tenhunen, 2002; Schlerf, Atzberger, and Hill, 2005; Leuschner et al., 2006). Ryan et al., 1997 (as cited in Battaglia et al., 1998) also state, that decline in LAI is the rule, whereas an equilibrium is the exception.

Multiple reasons for decreasing LAI with stand age are reported. Thinning, as a method in forest management to either improve site conditions in a younger stand, or remove dead trees in an older stand, or thinning as natural process in medium-aged to older ones leads to a variation or decline in LAI, depending on management practices (Schlerf, Atzberger, and Hill, 2005; Köstner, Falge, and Tenhunen, 2002). Logging in commercial forests leaves gaps, which also reduces LAI (Schlerf, Atzberger, and Hill, 2005). As soon as tree crowns reach a size, where they interact with each other, LAI starts to decrease because of crown abrasion (Ryan et al., 1997, as cited in Leuschner et al., 2006, Schlerf, Atzberger, and Hill, 2005). Other reported age-related causes for decreasing LAI include defoliation in older forest stands (Pokorny and Stojnic, 2012), decreasing nutrient availability (Leuschner et al., 2006), or higher mortality in older stands (Ryan et al., 1997, as cited in Leuschner et al., 2006).

As described in chapter 3.3.3, additional forest parameters are available for the LiDAR-based forest map. One of these parameters is the age class (in German *Wuchsklasse*, abbreviated with WKL). It is derived by Bauer et al., 2015 from crown closure and diameter at breast height (DBH) (see table 6.3).

Table 6.3: Age class of forest

age class	*WKL*
Blöße (seedling)	1
Jungwuchs/Dickung (sapling)	2
Stangenholz (pole)	3
Baumholz schwach (mature tree, weak wood)	4
Baumholt mittel (mature tree, middle wood)	5
Starkholz (mature tree, strong wood)	6

Source: adapted from Bauer et al., 2015

The age class is a more appropriate tool to describe the stage of development of a tree than the tree age alone. Many site conditions, like water and nutrient availability, soil, or aspect, as well as management practices influence tree growth (e.g. Ludlow, 1997), therefore trees of the same age can diverge strongly in their development. For this reason, the age class cannot be directly linked to stand age. However, on the basis of the age class, forest development stages like "first growing period" and management practices like "first thinning" can be derived. The first growing period is equivalent to age class 2 (WKL 2) and first thinning usually takes place when a stand is fully stocked (Kerr and Haufe, 2011), a measure which depends on stands per hectare and DBH (e.g. Edwards and Christie, 1981; Emmingham and Elwood, 1983), and can be compared to age class 3 (WKL 3).

In figure 6.21, LAI value distribution for coniferous (top) and deciduous (bottom) forest (after Gregoire and Raffy, 1997, as cited in Bach et al., 2003), is shown per age class. Coniferous forest (top in figure 6.21) shows highest LAI for WKL 2, after which it gradually declines up until WKL 4 and then increases

again through WKL 5 and 6. The results appear to be in agreement with the aforementioned relationship between LAI and tree development derived from age class. Coniferous forest stands in Austria are mostly made up of spruce (a „fast-growing“ tree (Pokorny and Stojnic, 2012)) so a peak LAI is expected in WKL 2. Also the steady decrease after that is well described in literature. The renewed increase after WKL 4 could be attributed to forestry management thinning (Schlerf, Atzberger, and Hill, 2005). LAI per age class after Chen and Cihlar, 1996 and Schiffmann et al., 2008 show the same trend as seen in figure 6.21, their plots can be seen in the appendix.
The LAI differences in age class for deciduous forest (bottom in figure 6.21) are less distinct than in coniferous forest but also in this case, LAI for WKL 2 is highest and gradually declines through the age classes 3 to 6. Contrary to coniferous forest, no renewed increase after WKL 4 is visible, which could be owed to a different forest management. The steady and slow decrease towards a possible equilibrium stage is also well reported for deciduous trees (He et al., 2012; Leuschner et al., 2006).

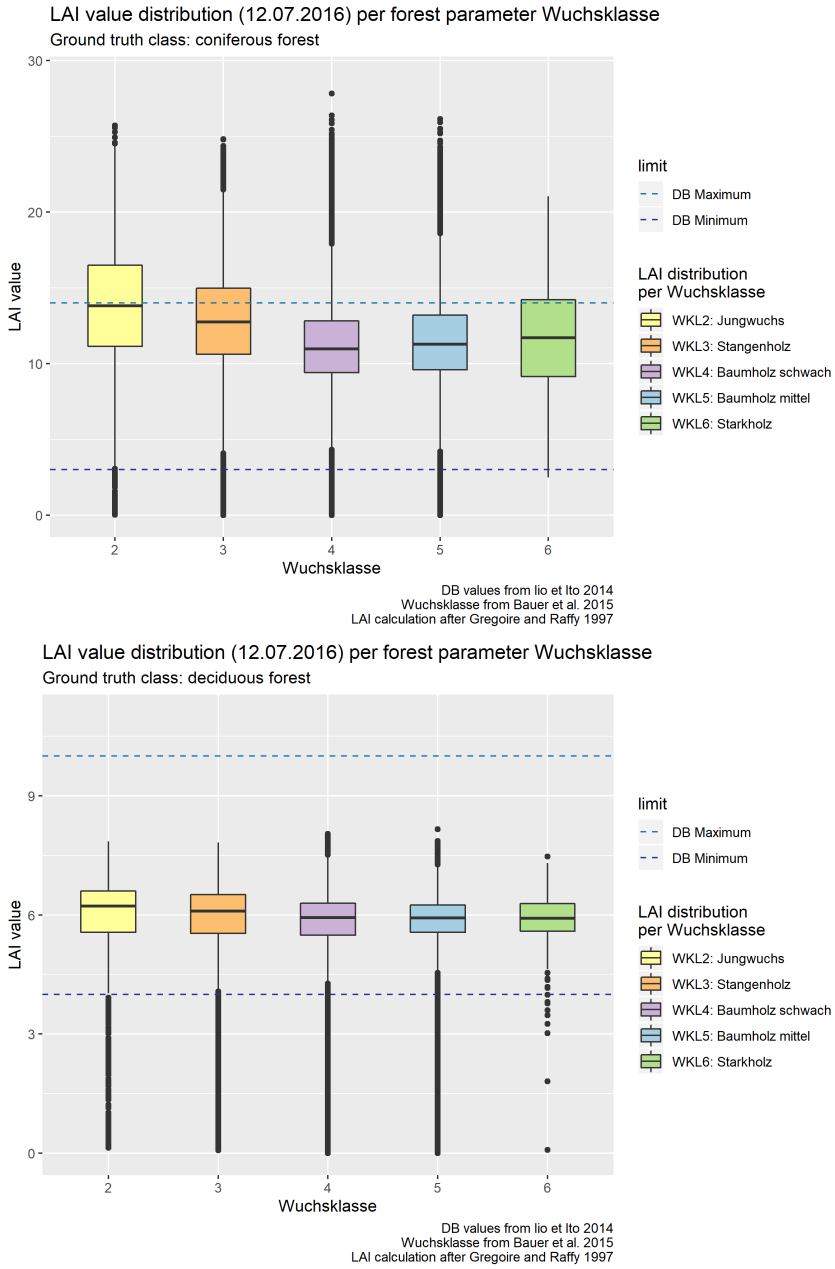

Figure 6.21: LAI value distribution per WKL for the class *coniferous forest* (top) and *deciduous forest* (bottom) after Gregoire and Raffy, 1997 (as cited in Bach et al., 2003)

Source: own illustration

6.3.2 Crops

Despite the very plant type specific nature of LAI (Haboudane et al., 2004; González-Sanpedro et al., 2008), only non-crop-type-specific regression functions were applicable for this study area and used satellite imagery, as described in chapter 5.4.2. Equations 5.25, 5.27, and 5.28 are used to calculate LAI from Sentinel-2 scenes. To exemplarily validate the results, ground truth about the crop types *maize* and *wheat* (chapter 3.3.2) are used, to compare the results to terrestrial LAI measurements (taken from Scurlock, Asner, and Gower, 2001). Analogous to chapter 6.3.1, boxplots are created for each used date.

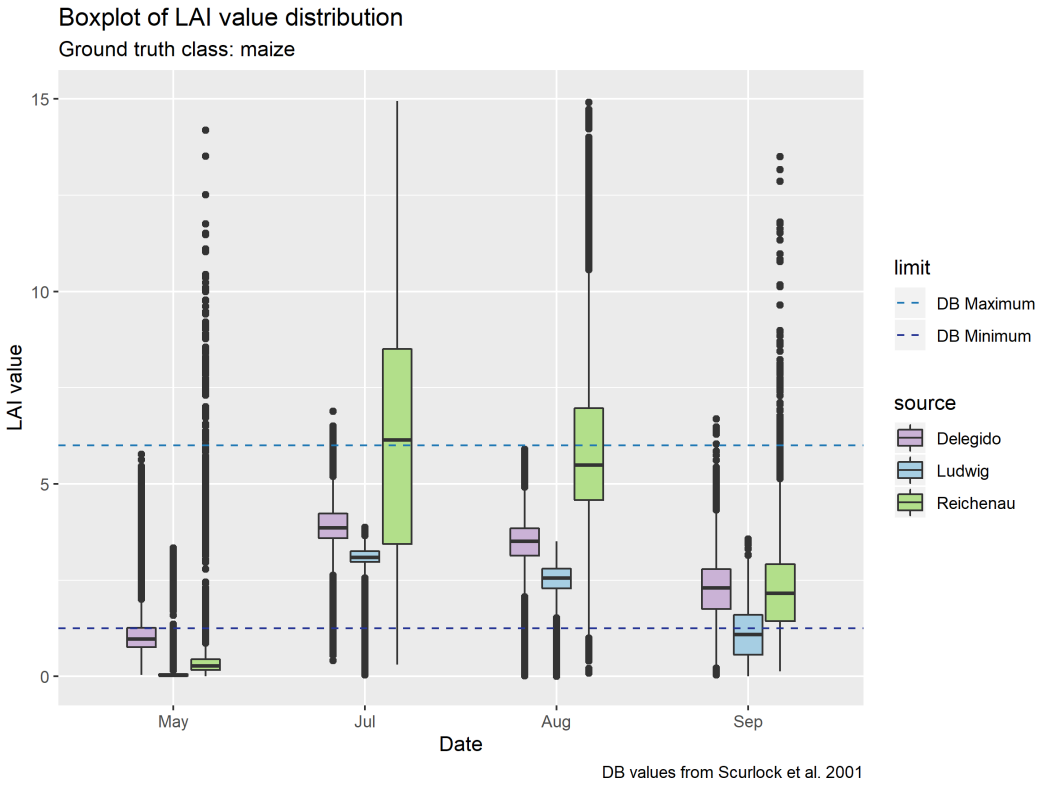

Figure 6.22: LAI value distribution for *maize*

Source: own illustration

Figure 6.22 depicts the boxplots for the class *maize* from May to September for all three applied methods. The dashed lines parallel to the x-axis symbolise the minimum and maximum taken from the LAI database (Scurlock, Asner, and Gower, 2001. The methods from Ludwig et al., 1999 (as cited in Bach et al., 2003) and Delegido, Verrelst, Alonso, et al., 2011 show a comparable trend, but differ slightly in degree of value dispersion and height of reached values. While Ludwig's method uses a polynomial function of degree three, applied in Northern Italy, Delegido's method comprises a linear function established for field data gathered in central Spain, Northern Germany, and Southwestern France. Both methods produce values predominantly below the found minimum in the database (Scurlock, Asner, and Gower, 2001) in May and a strong increase up to July. Unfortunately no Sentinel-2 scenes were available for June 2016, as described in chapter 3.1. After July, a decrease in LAI throughout August and September for these two methods occurs. The values obtained through Delegido's method are higher on average than Ludwig's values, with the highest mean LAI value at approximately 3.8 or 3 respectively.
Reichenau's method also delivers LAI values below the database minimum for May by a majority, however, for the remaining months their approach presents slightly different properties. The values disperse very strongly for July and August and have many more upward outliers, compared to Ludwig's and Delegido's methods. The produced LAI values for September are comparable to the ones obtained from Delegido but with stronger dispersion.
Consulting the literature on ground-based LAI measurements for maize through the course of a year, the start of increase in *green* LAI is reported for around DOY (day of year) 150 - 160 with a peak around DOY 180 - 215, depending on the publication (Bsaibes et al., 2009; Gitelson, Viña, et al., 2003; Kang et al., 2016; Heggenstaller, Liebman, and Anex, 2009). After that, LAI decreases, first gradually and then abruptly. Figure 6.23 shows the dynamics of maize LAI through the course of year after Bsaibes et al., 2009 (top) and Gitelson, Viña, et al., 2003 (bottom). In table 6.4, each date of the scene is matched with its DOY for 2016.

Following the trend of LAI values, Ludwig's and Delegido's methods appear to match the expected behaviour found in the literature. The May scene (DOY 144) is set before the expected increase in LAI at DOY 150 - 160 so values should be recognisably lower than in the following months. Highest LAI for these two methods are obtained in the July scene (DOY 194) and the decrease throughout August (DOY 244) and September (DOY 267) also fall in line with the findings in the publications. Bsaibes et al., 2009 conducted their study in Southern France, Kang et al., 2016 in Iowa, USA, and Gitelson, Viña, et al., 2003 used data from the previously described SPARC campaign (Spain). They report maximum LAI values for maize of approximately 3, 4, and 6 respectively, confirming the maximum values obtained from Ludwig's and Delegido's methods. Reichenau's approach also portrays this trend, but, as mentioned before, their values disperse considerably more. Concluding, all three methods appear to produce LAI values that are in agreement with the database (Scurlock, Asner, and Gower, 2001) and other publications, and match the expected behaviour through the course of a year, but the strong dispersion of values produced by Reichenau's method make their approach less reliable regarding correctness of calculated values. Partly, this could be attributed to the use of an already deficient product - the FVC calculated from NDVI (as discussed in chapter 6.2) - which is necessary to apply Reichenau's approach (see equation 5.28).

Table 6.4: DOY 2016

Date 2016	*DOY 2016*
14.03.	74
13.04.	104
23.05.	144
12.07.	194
31.08.	244
23.09.	267

Source: *Day-Of-Year Calendar* 2019

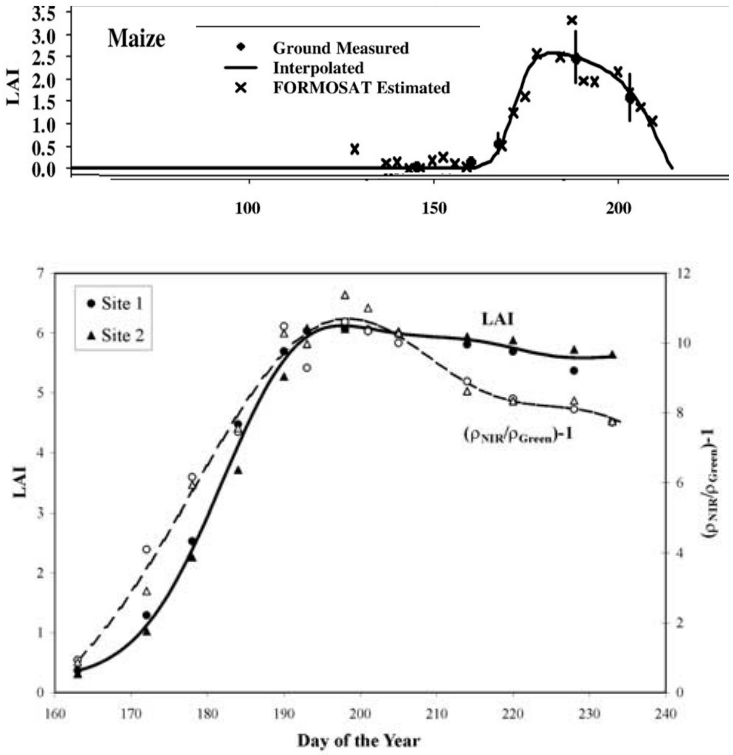

Figure 6.23: Dynamics of maize LAI after Bsaibes et al., 2009 and Gitelson, Viña, et al., 2003

Source: adapted after Bsaibes et al., 2009 (top), Gitelson, Viña, et al., 2003 (bottom)

The results for the class *wheat* from March to August for all three applied methods are shown in figure 6.24. All three methods show a similar trend from month to month and for each month the distribution of values is comparable to the class *maize*: Ludwigs's method delivers the lowest, and Reichenau's method again the highest and most strongly dispersed values.
According to literature and depending on the wheat variety (winter, spring, or summer), phenological development starts at around DOY 60 - 80 for winter wheat (Grünhage et al., 1999; Huang et al., 2016; Bsaibes et al., 2009) and at around DOY 100 for spring wheat (Grünhage et al., 1999). Maximum LAI values are reported around DOY 130 (Huang et al., 2016, study conducted in Heibei Province, China), 140 (Bsaibes et al., 2009, study conducted in Southern

France), and 165 (Grünhage et al., 1999, study conducted in Lower Saxony, Germany). After the peak, LAI declines and Grünhage et al., 1999 report harvest at approximately DOY 220.
Figure 6.24 illustrates the increase in LAI from March (DOY 74) to May (DOY 144) in all the tested methods, which is in agreement with the expected course described in the literature. While Ludwig's method produces values below the database minimum for March, all the others lie mainly in between the limits. Reichenau's method again delivers the most upward outliers and for May also a part of the third quartile is above the database maximum. From May to July the LAI decreases significantly, which could be attributed partly to browning leaves and partly to already harvested fields. From the ground truth data on crops (chapter 3.3.2) some information is available on whether a polygon has been already harvested or not at a certain field campaign date and all wheat polygons have been used for this boxplot. The repeated increase from July to August could be caused by crop rotation.
Maximum LAI values from the aforementioned studies reach 2.5 (Bsaibes et al., 2009), 4.5 (Grünhage et al., 1999), and up to 7 (Huang et al., 2016). All three tested methods seem to be in accordance with this, concerning maximum LAI values. Again, without ground-based LAI measurements of the tested area, no conclusive statement can be made about one method being more or less suitable than the other to determine LAI of wheat.

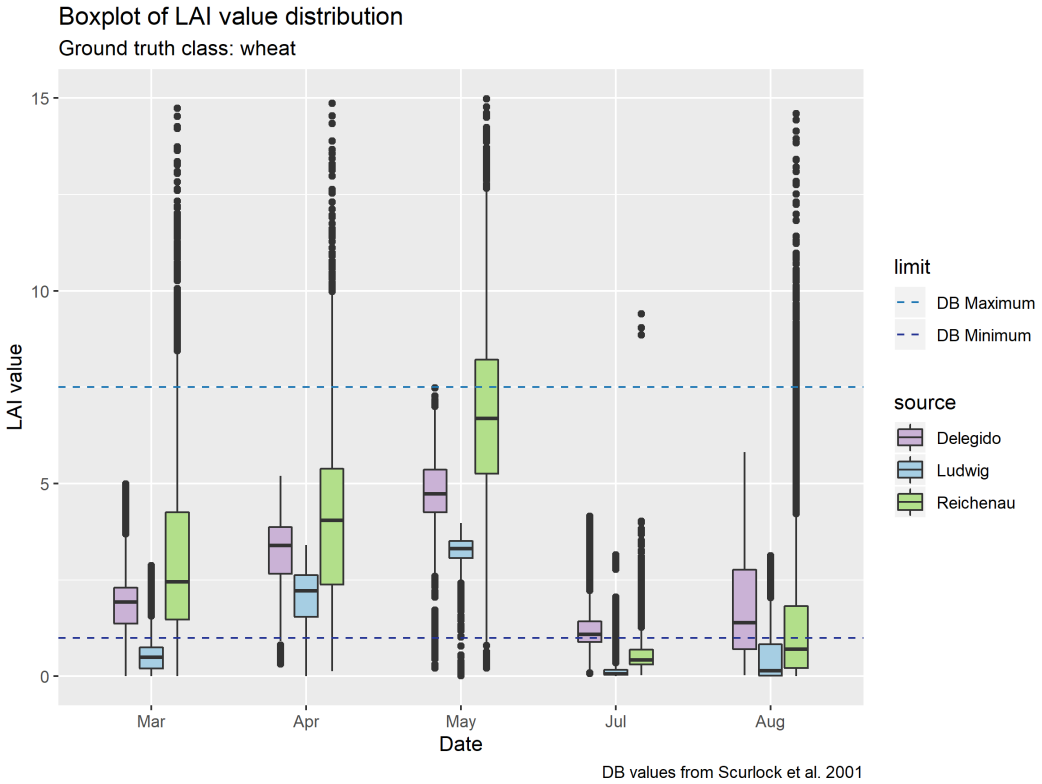

Figure 6.24: LAI value distribution for *wheat*

Source: own illustration

Although only those methods could be employed for crop LAI calculation, which did not specifically consider the crop type, they appear to be capable of reflecting the course of LAI throughout the vegetation period. Considering, that mostly these methods are adapted for green LAI only and are derived from NDVI or another VI, this result is not surprising and to be expected. With the higher temporal resolution reached through the constellation of Sentinel-2A and 2B, further investigations are possible about the yearly trend of LAI of different crop types. However, new ground truth data would need to be collected in field campaigns for the investigated year. To give a statement about the reached LAI values through calculation, ground-based LAI reference measurements would be beneficiary. The deficiencies of using values from available databases have already been discussed.

7 Conclusion and Outlook

This thesis applies different retrieving approaches for three biogeophysical parameters (albedo, FVC, LAI) to Sentinel-2A satellite images and analyses the plausibility of the remote sensing based obtained results through various steps. The plausibility analysis is conducted in different ways, depending on the availability of reference data. The applied approaches are chosen from an extensive literature review, according to their anticipated transferability, regarding used sensors and study site specific conditions of this thesis.

Albedo is calculated with a band weighting function after S. Liang, 2000 and the results are validated using Copernicus' Urban Atlas classification and albedo ranges for different ground cover types gained through non remote sensing methods (taken from Pielke and Avissar, 1990). At first sight, the results look promising, but ample limitations regarding the reliability of these test results have to be considered. The inadequacy of the Urban Atlas classification as a validation dataset as well as the inaccuracy of derived statements from using ranges as reference are two of the main drawbacks in performing plausibility analyses with the given data. Liang's method proves to be sensitive to a present snow cover and to seasonal variations of albedo in the study area, using Sentinel-2 imagery. However, without ground-based measurements in the study area, ideally synchronised with the overfly time of the satellite, the correctness of the calculated values cannot be verified accurately.

Three different vegetation indices (GVI, MSAVI, NDVI) are used within a scaling function (equation 5.8) to calculate Fraction of Vegetation Cover. The results are validated using a soil sealing map provided by Graz, 2019 indicating, that the method is well suited for the scaling of FVC from Vegetation Indices for the tested Sentinel-2 data at different dates. NDVI scores the lowest error in

three out of four dates and GVI delivers the best result with a mean of 0.0187. GVI also delivers the poorest result (mean: 0.0865) for one date. The initially anticipated better performance of MSAVI over NDVI and GVI could not be confirmed. On the contrary, MASVI produces the poorest results for three out of four dates.
Limitations were addressed regarding the selection process of the scaling parameters VI_v and VI_s, as well as the validation data set. Better suitable reference data and ground truth data would be required to validate the FVC results for the used satellite data and study area.

Leaf Area Index is ground cover type dependent (González-Sanpedro et al., 2008), therefore different empirical regression functions are applied to two different cover types: forest and crops. To validate the results, databases containing non remote sensing based LAI measurements (Scurlock, Asner, and Gower, 2001 and Iio and Ito, 2014) are used.
For coniferous forest, Chen and Cihlar's method, which provides different regression functions (linear and exponential) for two indices (NDVI and SR) and different seasons (spring and summer), produces results mostly within the expected range, apart from one upward outlier (exponentially SR-derived LAI for spring). The strength of this approach lies most likely within the separate functions for different seasons, with which also LAI changes (Jonckheere et al., 2004). Gregoire's regression formulas appear to work well for deciduous forest but produce too much variation between dates for coniferous forest. Results from the regression functions taken from Schiffmann et al., 2008 underline the study-specific dependency of regression functions. Their study was conducted in a mountainous area in the USA, and LAI produced through their method is tendentially lower (and in some cases below the expected minimum) compared to the other approaches. Concerning LAI and its relation to age class, all three tested methods confirm the expectations of constant to slightly declining LAI with increasing age class. Although all methods (with the aforementioned exceptions) meet the criterion of producing LAI values within an expected range, no qualitative comparison of methods is possible without reference measurements.
To calculate LAI for crops, three generic crop functions, which do not differentiate between crop types, are used. They are verified regarding their capability to produce fitting results of phenological behaviour for two different crop plants: maize and wheat. For both crop types, the results suggest partial to good

agreement with the findings in literature, regarding (a) the maximum values reached and (b) the course of LAI during the growing period. While Ludwig's method generally produces the lowest LAI values on average per month, Delegido's method shows a comparable trend with tendentially slightly higher values. Reichenau's FVC-based approach delivers the highest and most strongly dispersed values during the growing period. With the high dynamics of crop LAI, more input data would be necessary, to better analyse the trajectory. Especially the Sentinel-2 data gap in June could provide vital information. Analogous to forest, also in this case reference measurements are indispensable to qualitatively compare the tested methods.

Coming back to the main study objectives outlined at the beginning of this thesis, the literature review revealed a large spectrum of available optical remote sensing based approaches for the retrieval of the three investigated biogeophysical parameters. Mainly those studies, which are using Landsat data to derive empirical relationships for the variables, are chosen for this research, due to comparable band widths with the Sentinel-2 satellite, but also other studies, using RapidEye or Sentinel-2 simulations obtained from hyperspectral data are applied. A great number of the tested approaches show plausible results in general, whilst some approaches appear better suited than others. Finally, all deduced statements about the plausibility of results are derived on the basis of freely available reference data. With ground truth measurements for each parameter, a more accurate analysis of the transferability of techniques would be possible. In the future, more publications about empirical relationships for biogeophysical variables based on Sentinel-2 are expected, which will allow for further transferability analyses between different study settings. The constellation of the Sentinel-2A and 2B satellite will increase the availability of more cloud free data, thus enabling a more coherent stream of data input, especially for crop analysis.

Bibliography

Aschbacher, J. and M. P. Milagro-Pérez (2012). "The European Earth monitoring (GMES) programme: Status and perspectives." In: *Remote Sensing of Environment* 120, pp. 3–8. DOI: 10.1016/j.rse.2011.08.028 (cit. on pp. 19, 20).

Aubin, I., M. Beaudet, and C. Messier (2000). "Light extinction coefficients specific to the understory vegetation of the southern boreal forest, Quebec." In: *Canadian Journal of Forest Research* 30, pp. 168–177. DOI: 10.1139/x99-185 (cit. on pp. 52, 86).

Auer, I., R. Böhm, and W. Schöner (2001). "Austrian long-term climate 1767-2000." In: *Österreichische Beiträge zu Meteorologie und Geophysik* 25, p. 147. ISSN: 1016-6254 (cit. on p. 30).

Bach, H. et al. (2003). "Use of remote sensing for hydrological parameterisation of Alpine catchments." In: *Hydrology and Earth System Sciences Discussions* 7, pp. 862–876 (cit. on pp. 16, 39, 49, 51, 55, 81, 83, 88, 90, 92).

Baldocchi, D. D. and T. Meyers (1998). "On using eco-physiological, micrometeorological and biogeochemical theory to evaluate carbon dioxide, water vapor and trace gas fluxes over vegetation: a perspective." In: *Agricultural and Forest Meteorology* 90, pp. 1–25. DOI: 10.1016/S0168-1923(97)00072-5 (cit. on p. 14).

Barati, S. et al. (2011). "Comparison the accuracies of different spectral indices for estimation of vegetation cover fraction in sparse vegetated areas." In: *The Egyptian Journal of Remote Sensing and Space Science* 14, pp. 46–56. DOI: 10.1016/j.ejrs.2011.06.001 (cit. on pp. 11, 12, 41).

Barlage, M. and X. Zeng (2004). "The impact of fractional vegetation cover and leaf area index on warm season precipitation variability in global ensemble simulations." In: *Arizona Journal of Hydrometeorology*, pp. 823–830 (cit. on pp. 9, 41).

Battaglia, M. et al. (Aug. 1998). "Prediction of leaf area index in eucalypt plantations: effects of water stress and temperature." In: *Tree Physiology* 18, pp. 521–528. DOI: 10.1093/treephys/18.8-9.521 (cit. on p. 87).

Bauer, C. et al. (2015). *Ableitung forstlicher Parameter aus Laserscanner Daten und Erstellung von Gefahrenhinweiskarten für die Steiermark*. Tech. rep. Joanneum Research, p. 70 (cit. on pp. 27, 69, 88).

Berger, M. et al. (2012). "ESA's sentinel missions in support of Earth system science." In: *Remote Sensing of Environment* 120, pp. 84–90. DOI: 10.1016/j.rse.2011.07.023 (cit. on pp. 19, 20).

Brovkin, V. et al. (2013). "Evaluation of vegetation cover and land-surface abedo in MPI-ESM CMIP5 simulations." In: *Journal of Advances in Modeling Earth Systems* 5, pp. 48–57. DOI: 10.1029/2012MS000169 (cit. on pp. 1, 2).

Bsaibes, A. et al. (Apr. 2009). "Albedo and LAI estimates from FORMOSAT-2 data for crop monitoring." In: *Remote Sensing of Environment* 113, pp. 716–729. DOI: 10.1016/j.rse.2008.11.014 (cit. on pp. 92–95).

Burakowski, E. A. et al. (2015). "Spatial scaling of reflectance and surface albedo over a mixed-use, temperate forest landscape during snow-covered periods." In: *Remote Sensing of Environment* 158, pp. 465–477. DOI: 10.1016/j.rse.2014.11.023 (cit. on p. 7).

Buyantuyev, A., J. Wu, and C. Gries (2007). "Estimating vegetation cover in an urban environment based on Landsat ETM+ imagery: a case study in Phoenix, USA." In: *International Journal of Remote Sensing* 28, pp. 269–291. DOI: 10.1080/01431160600658149 (cit. on pp. 9, 11–13, 41).

Campioli, M. et al. (Sept. 2011). "Temporal variability of the NPP-GPP ratio at seasonal and interannual time scales in a temperate beech forest." In: *Biogeosciences* 8, pp. 2481–2492. DOI: 10.5194/bg-8-2481-2011 (cit. on p. 82).

Carlson, T. N. and D. A. Ripley (1997). "On the Relation between NDVI, Fractional Vegetation Cover, and Leaf Area Index." In: *Remote Sensing of Environment* 62, pp. 241–252 (cit. on pp. 11–13, 17).

Cescatti, A. et al. (2012). "Intercomparison of MODIS albedo retrievals and in situ measurements across the global FLUXNET network." In: *Remote Sensing of Environment* 121, pp. 323–334. DOI: 10.1016/j.rse.2012.02.019 (cit. on pp. 6–8, 67).

Chason, J. W., D. D. Baldocchi, and M. A. Huston (1991). "A comparison of direct and indirect methods for estimating forest canopy leaf area." In:

Agricultural and Forest Meteorology 57, pp. 107–128. DOI: 10.1016/j.isprsjprs.2013.04.007 (cit. on pp. 14, 18).

Chen, J. M. and T. A. Black (1992). "Defining Leaf Area Index for non-flat leaves." In: *Plant, Cell and Environment* 15, pp. 421–429. DOI: 10.1111/j.1365-3040.1992.tb00992.x (cit. on p. 14).

Chen, J. M. and J. Cihlar (1996). "Retrieving leaf area index of boreal conifer forests using Landsat TM images." In: *Remote Sensing of Environment* 55, pp. 153–162. DOI: 10.1016/0034-4257(95)00195-6 (cit. on pp. 14–16, 39, 48, 55, 79, 80, 85, 89).

Clerk, S. (2019). *S2 MPC L1C Data Quality Report*. Ref. S2-PDGS-MPC-DQR. Tech. rep. 44. European Space Agency, p. 46. URL: https://sentinel.esa.int/documents/247904/685211/Sentinel-2_L1C_Data_Quality_Report (cit. on p. 54).

Clevers, J. G. P. W., L. Kooistra, and M. M. M. van den Brande (2017). "Using Sentinel-2 Data for Retrieving LAI and Leaf and Canopy Chlorophyll Content of a Potato Crop." In: *Remote Sensing* 9, pp. 1–15. DOI: 10.3390/rs9050405 (cit. on p. 15).

Österreichischer Sachstandsbericht Klimawandel 2014 (2014). *Austrian Assessment Report 2014 (AAR14)*. Verlag der Österreichischen Akademie der Wissenschaften, p. 1096. ISBN: 978-3-7001-7699-2 (cit. on p. 30).

Coakley, J. A. (2003). "Reflectance and albedo, surface." In: *Encyclopedia of the Atmosphere*, pp. 1914–1923 (cit. on pp. 5–7, 68, 69).

Cogley, J. G. (1979). "The albedo of water as function of latitude." In: *Monthly Weather Review* 107, pp. 775–781 (cit. on p. 69).

Colombo, R. et al. (2003). "Retrieval of leaf area index in different vegetation types using high resolution satellite data." In: *Remote Sensing of Environment* 86, pp. 120–131. DOI: 10.1016/S0034-4257(03)00094-4 (cit. on pp. 15, 16).

Copernicus (Nov. 2, 2018). *Copernicus Global Land Service Products: FVC*. URL: https://land.copernicus.eu/global/products/fcover (cit. on p. 8).

Copernicus (June 5, 2019a). *Copernicus Land Monitoring Service*. URL: https://land.copernicus.eu/ (cit. on p. 25).

Copernicus (Apr. 4, 2019b). *Copernicus Local Component: Urban Atlas, 2012*. URL: https://land.copernicus.eu/local/urban-atlas/urban-atlas-2012 (cit. on pp. 25, 26, 53, 69).

Curran, P. J. and A. M. Hay (1986). "The importance of measurement error for certain procedures in remote sensing at optical wavelengths." In: *Photogrammetric Engineering And Remote Sensing* 52, pp. 229–241 (cit. on p. 13).

Day-Of-Year Calendar (Sept. 30, 2019). National Oceanic and Atmospheric Administration. URL: https://www.esrl.noaa.gov/gmd/grad/neubrew/Calendar.jsp?view=DOY&year=2016&col=4 (cit. on p. 93).

Delegido, J., J. Verrelst, L. Alonso, et al. (2011). "Evaluation of Sentinel-2 Red-Edge bands for empirical estimation of green LAI and Chlorophyll content." In: *Sensors* 11, pp. 7063–7081. DOI: 10.3390/s110707063 (cit. on pp. 14–16, 18, 39, 51, 92).

Delegido, J., J. Verrelst, J. P. Rivera, et al. (Mar. 2015). "Brown and green LAI mapping through spectral indices." In: *International Journal of Applied Earth Observation and Geoinformation* 35, pp. 350–358. DOI: 10.1016/j.jag.2014.10.001 (cit. on pp. 14, 18).

DeRose, R. J. and R. S. Seymour (Apr. 2010). "Patterns of leaf area index during stand development in even-aged balsam fir - red spruce stands." In: *Canadian Journal of Forest Research* 40, pp. 629–637. DOI: 10.1139/x10-018 (cit. on p. 86).

Deutsches Zentrum für Luft- und Raumfahrt (Mar. 27, 2019). *Strahlungsgrößen der Erdoberfläche: Albedo*. Deutsches Zentrum für Luft- und Raumfahrt. URL: https://www.dlr.de/eoc/desktopdefault.aspx/tabid-9140/19508_read-45421 (cit. on p. 5).

Dorigo, W. A. et al. (May 2007). "A review on reflective remote sensing and data assimilation techniques for enhanced agroecosystem modeling." In: *International Journal of Applied Earth Observation and Geoinformation* 9, pp. 165–193. DOI: 10.1016/j.jag.2006.05.003 (cit. on p. 1).

Drusch, M. et al. (2012). "Sentinel-2: ESA's Optical High-Resolution Mission for GMES Operational Services." In: *Remote Sensing of Environment* 120, pp. 25–36. DOI: 10.1016/j.rse.2011.11.026 (cit. on pp. 19–21).

Edwards, P. N. and J. M. Christie (1981). *Yield models for forest management*. Forestry Commission (cit. on p. 88).

Emde, C. et al. (May 2016). "The libRadtran software package for radiative transfer calculations (version 2.0.1)." In: *Geoscientific Model Development* 9, pp. 1647–1672. DOI: 10.5194/gmd-9-1647-2016 (cit. on p. 36).

Emmingham, W. H. and N. E. Elwood (1983). *Thinning: An important timber management tool*. Tech. rep. Pacific Northwest Extension Publication 184 (cit. on p. 88).

eoPortal (Mar. 27, 2019). *RapidEye Earth Observation Constellation*. Ed. by Earth Observation Portal. URL: https://directory.eoportal.org/web/eoportal/satellite-missions/r/rapideye (cit. on p. 51).

ESA (2005). *SPARC Data Acquisition Report 2004*. Tech. rep. European Space Agency (cit. on p. 16).

ESA (2015). *The story of Sentinel-2. ESA Bulletin 161*. Tech. rep. ESA, p. 9. URL: https://esamultimedia.esa.int/docs/EarthObservation/Sentinel-2_ESA_Bulletin161.pdf (cit. on p. 21).

ESA (Oct. 17, 2018a). *Observing the earth: Copernicus*. URL: http://www.esa.int/Our_Activities/Observing_the_Earth/Copernicus (cit. on pp. 19, 22).

ESA (Oct. 17, 2018b). *Sentinel Mission Overview*. URL: https://earth.esa.int/web/sentinel/missions (cit. on p. 19).

Flanner, M. G. (Jan. 2009). "Integrating anthropogenic heat flux with global climate models." In: *Geophysical Research Letters* 36, pp. 1–4. DOI: 10.1029/2008gl036465 (cit. on p. 3).

Fletcher, K. (2012). "Sentinel-2: ESA's Optical High-Resolution Mission for GMES Operational Services (ESA SP-1322/2 March 2012)." In: *ESA*. Ed. by K. Fletcher, p. 70 (cit. on pp. 19, 21, 22).

Frampton, W. J. et al. (2013). "Evaluating the capabilities of Sentinel-2 for quantitative estimation of biophysical variables in vegetation." In: *ISPRS Journal of Photogrammetry and Remote Sensing* 82, pp. 83–92. DOI: 10.1016/j.isprsjprs.2013.04.007 (cit. on pp. 15, 16).

GCOS (Mar. 27, 2019). *The GCOS Essential Climate Variable (ECV) Data Access Matrix*. Ed. by Global Observing System for Climate. URL: https://www.ncdc.noaa.gov/gosic/gcos-essential-climate-variable-ecv-data-access-matrix (cit. on p. 7).

Gebhardt, H. et al. (2007). *Geographie: Physische Geographie und Humangeographie*. München: Elsevier, p. 1096 (cit. on p. 69).

Gent, P. R. (2013). "Coupled Models and Climate Projections." In: *International Geophysics*. Vol. 103. Elsevier, pp. 609–623. DOI: 10.1016/b978-0-12-391851-2.00023-4 (cit. on p. 1).

Gitelson, A. A., Y. J. Kaufman, et al. (2002). "Novel algorithms for remote estimation of vegetation fraction." In: *Remote Sensing of Environment* 80, pp. 76–87 (cit. on pp. 8, 9, 11–13).

Gitelson, A. A., A. Viña, et al. (Mar. 2003). "Remote estimation of leaf area index and green leaf biomass in maize canopies." In: *Geophysical Research Letters* 30, pp. 1–4. DOI: 10.1029/2002gl016450 (cit. on pp. 92–94).

Gong, P. and R. Pu aand J. R. Miller (1995). "Coniferous Forest Leaf Area Index Estimation along the Oregon Transect Using Compact Airborne Spectrographic lmager Data." In: *Photogrammetric Engineering and Remote Sensing* 61, pp. 1107–1117 (cit. on pp. 14–16, 46).

Gong, P., R. Pu, et al. (2003). "Estimation of Forest Leaf Area Index Using Vegetation Indices Derived From Hyperion Hyperspectral Data." In: *IEEE Transactions on Geoscience and Remote Sensing* 41, pp. 1355–1362. DOI: 10.1109/TGRS.2003.812910 (cit. on pp. 15, 16).

González-Sanpedro, M. C. et al. (2008). "Seasonal variations of leaf area index of agricultural fields retrieved from Landsat data." In: *Remote Sensing of Environment* 112, pp. 810–824. DOI: 10.1016/j.rse.2007.06.018 (cit. on pp. 15, 17, 18, 46, 91, 98).

Gratton, D., P. Howarth, and D. Marceau (Mar. 1993). "Using Landsat-5 thematic mapper and digital elevation data to determine the net radiation field of a Mountain Glacier." In: *Remote Sensing of Environment* 43, pp. 315–331. DOI: 10.1016/0034-4257(93)90073-7 (cit. on p. 8).

Graz, Stadt (2019). "Soil Sealing Map of Graz" (cit. on pp. 28, 32, 54, 55, 72, 97).

Grünhage, L. et al. (May 1999). "The European critical levels for ozone: improving their usage." In: *Environmental Pollution* 105, pp. 163–173. DOI: 10.1016/s0269-7491(99)00029-9 (cit. on pp. 94, 95).

Gutman, G. and A. Ignatov (1998). "The derivation of the green vegetation fraction from NOAA/AVHRR data for use in numerical weather prediction models." In: *International Journal of Remote Sensing* 19, pp. 1533–1543. DOI: 10.1080/014311698215333 (cit. on pp. 9, 11, 12).

Haboudane, D. et al. (2004). "Estimation of Leaf Area Index using ground spectral measurements over agriculture crops: Prediction capability assessment of optical indices." In: *XXth ISPRS Congress: "Geo-Imagery Bridging Continents". Istanbul, Turkey* (cit. on pp. 15–18, 46, 91).

Hajnsek, I. et al. (2007). "AgriSAR 2006—Airborne SAR and optics campaigns for an improved monitoring of agricultural processes and practices." In: *Geophys. Res. Abstr.* (Cit. on p. 16).

He, L. et al. (Aug. 2012). "Relationships between net primary productivity and forest stand age in U.S. forests." In: *Global Biogeochemical Cycles* 26, pp. 1–19. DOI: 10.1029/2010gb003942 (cit. on p. 89).

Heggenstaller, A. H., M. Liebman, and R. P. Anex (2009). "Growth Analysis of Biomass Production in Sole-Crop and Double-Crop Corn Systems." In: *Crop Science* 49, pp. 2215–2224. DOI: 10.2135/cropsci2008.12.0709 (cit. on p. 92).

Herrmann, I. et al. (2011). "LAI assessment of wheat and potato crops by VENuS and Sentinel-2 bands." In: *Remote Sensing of Environment* 115, pp. 2141–2151. DOI: 10.1016/j.rse.2011.04.018 (cit. on pp. 14, 15).

Hovi, A. et al. (Apr. 2019). "Seasonal dynamics of albedo across European boreal forests: Analysis of MODIS albedo and structural metrics from airborne LiDAR." In: *Remote Sensing of Environment* 224, pp. 365–381. DOI: 10.1016/j.rse.2019.02.001 (cit. on p. 69).

Huang, J. et al. (Jan. 2016). "Assimilating a synthetic Kalman filter leaf area index series into the WOFOST model to improve regional winter wheat yield estimation." In: *Agricultural and Forest Meteorology* 216, pp. 188–202. DOI: 10.1016/j.agrformet.2015.10.013 (cit. on pp. 94, 95).

Iio, A. and A. Ito (2014). *A Global Database of Field-observed Leaf Area Index in Woody Plant Species, 1932-2011*. DOI: 10.3334/ornldaac/1231. URL: http://daac.ornl.gov/cgi-bin/dsviewer.pl?ds_id=1231 (cit. on pp. 24, 56, 78, 81, 85, 98).

Jiang, Z. et al. (2006). "Analysis of NDVI and scaled difference vegetation index retrievals of vegetation fraction." In: *Remote Sensing of Environment* 101, pp. 366–378. DOI: 10.1016/j.rse.2006.01.003 (cit. on p. 11).

Jiménez-Muñoz, J. C., J. A. Sobrino, L. Guanter, et al. (2005). "Fractional vegetation cover estimation from PROBA/CHRIS data: Methods, analysis of angular effects and application to the land surface emissivity retrieval." In: *Proc. 3rd Workshop CHRIS/Proba* (cit. on pp. 9, 13).

Jiménez-Muñoz, J. C., J. A. Sobrino, A. Plaza, et al. (2009). "Comparison between Fraction Vegetation Cover Retrievals from Vegetation Indices and Spectral Mixture Analysis: Case Stufx of PROBA/CHRIS Data Over an Agricultural Area." In: *Sensors* 9, pp. 768–793. DOI: 10.3390/s90200768 (cit. on pp. 1, 8–13, 39, 41, 44, 45).

Johnson, B., R. Tateishi, and T. Kobayashi (2012). "Remote Sensing of Fractional Green Vegetation Cover Using Spatially-Interpolated Endmembers." In: *Remote Sensing* 4, pp. 2619–2634. DOI: 10.3390/rs4092619 (cit. on pp. 9–12, 39, 41, 45).

Jonckheere, I. et al. (2004). "Review of methods for in situ leaf area index determination Part I. Theories, sensors and hemispherical photography." In: *Agricultural and Forest Meteorology* 121, pp. 19–35. DOI: 10.1016/j.agrformet.2003.08.027 (cit. on pp. 14–16, 98).

Jong, B. de (1973). *Net radiation by a horizontal surface at the earth*. Delft University Press. ISBN: 90-298-3001-8 (cit. on pp. 68, 69).

Kabas, T. (2012). "WegenerNet Klimastationsnetz Region Feldbach: Experimenteller Aufbau und hochauflösende Daten für die Klima- und Umweltforschung." PhD thesis. Wegener Zentrum für Klima und Globalen Wandel und Institutsbereich Geophysik, Astrophysik und Meteorologie/Institut für Physik, Karl-Franzens-Universität Graz, p. 177 (cit. on p. 29).

Kang, Y. et al. (July 2016). "How Universal Is the Relationship between Remotely Sensed Vegetation Indices and Crop Leaf Area Index? A Global Assessment." In: *Remote Sensing* 8, pp. 1–29. DOI: 10.3390/rs8070597 (cit. on pp. 92, 93).

Kantor, P., F. Sach, and V. Cernohous (Feb. 2009). "Development of foliage biomass of young spruce and beech stands in the mountain water balance research area." In: *Journal of Forest Science* 55, pp. 51–62. DOI: 10.17221/72/2008-jfs (cit. on pp. 86, 87).

Kaspersen, P. S., R. Fensholt, and M. Drews (2015). "Using Landsat vegetation indices to estimate impervious surface fractions for European cities." In: *Remote Sensing* 7, pp. 8224–8249. DOI: 10.3390/rs70608224 (cit. on pp. 11, 12, 28, 41, 54).

Kerr, G. and J. Haufe (2011). "Thinning practice: a silvicultural guide." In: *Forestry Comission*, p. 54 (cit. on p. 88).

Keshava, N. and J. F. Mustard (2002). "Spectral unmixing." In: *IEEE signal processing magazine* 19, pp. 44–57 (cit. on pp. 9–11).

Kirchengast, G. (Feb. 16, 2018). "Landwirtschaft im Klimawandel – unter welchen klimatischen Voraussetzungen werden wir in Zukunft im südoststeirischen Raum produzieren?" In: (cit. on p. 29).

Köstner, B., E. Falge, and J. D. Tenhunen (June 2002). "Age-related effects on leaf area/sapwood area relationships, canopy transpiration and carbon gain of Norway spruce stands (Picea abies) in the Fichtelgebirge, Germany."

In: *Tree Physiology* 22, pp. 567–574. DOI: 10.1093/treephys/22.8.567 (cit. on p. 87).

Kuusinen, N. et al. (2014). "Measured and modelled albedos in Finnish boreal forest stands of different species, structure and understory." In: *Ecological Modelling* 284, pp. 10–18. DOI: 10.1016/j.ecolmodel.2014.04.007 (cit. on pp. 7, 69).

Landsat (Mar. 27, 2019). *Comparison of Landsat 7 and 8 bands with Sentinel-2.* URL: https://landsat.gsfc.nasa.gov/wp-content/uploads/2015/06/Landsat.v.Sentinel-2.png (cit. on p. 40).

Laurent, V. C. E. et al. (Jan. 2014). "Bayesian object-based estimation of LAI and chlorophyll from a simulated Sentinel-2 top-of-atmosphere radiance image." In: *Remote Sensing of Environment* 140, pp. 318–329. DOI: 10.1016/j.rse.2013.09.005 (cit. on pp. 15, 18).

Leuschner, C. et al. (Mar. 2006). "Variation in leaf area index and stand leaf mass of European beech across gradients of soil acidity and precipitation." In: *Plant Ecology* 186, pp. 247–258. DOI: 10.1007/s11258-006-9127-2 (cit. on pp. 87, 89).

Li, Y., H. Wang, and X.-B. Li (2015). "Fractional vegetation cover estimation based on an improved selective endmember spectral mixture model." In: *PloS one* 10, pp. 1–15. DOI: 10.1371/journal.pone.0124608 (cit. on pp. 9, 10).

Liang, S. (2000). "Narrowband to broadband conversions of land surface albedo I: Algorithms." In: *Remote Sensing of Environment* 76, pp. 213–238 (cit. on pp. 7, 8, 35, 40, 97).

Liang, S. (Oct. 2007). "Recent developments in estimating land surface biogeophysical variables from optical remote sensing." In: *Progress in Physical Geography: Earth and Environment* 31, pp. 501–516. DOI: 10.1177/0309133307084626 (cit. on p. 1).

Liang, S. et al. (2003). "Estimation and Validation of Land Surface Broadband Albedos and Leaf Area Index From EO-1 ALI Data." In: *IEEE Transactions on Geoscience and Remote Sensing* 41, pp. 1260–1267. DOI: 10.1109/TGRS.2003.813203 (cit. on pp. 7, 15, 17).

Liang, Z. et al. (2008). "A study on fast estimation of vegetation fraction in three Gorges emigration area by using SPOT5 imagery." In: *The International Archives of the Photogrammetry, Remote Sensing and Spatial Information Sciences* 37, pp. 987–992 (cit. on p. 11).

Lieb, G. K. (1991). *Eine Gebietsgliederung der Steiermark aufgrund naturräumicher Gegebenheiten*. Abteilung für Botanik am Landesmuseum Joanneum (cit. on p. 29).

Ludlow, A. (Apr. 1997). "Some factors influencing the increment of forests." In: *Forestry* 70, pp. 381–388. DOI: 10.1093/forestry/70.4.381 (cit. on p. 88).

Lukeš, P. et al. (2014). "Geographical gradients in boreal forest albedo and structure in Finland." In: *Remote Sensing of Environment* 152, pp. 526–535. DOI: 10.1016/j.rse.2014.06.023 (cit. on pp. 7, 8).

Luterbacher, J. et al. (2004). "European seasonal and annual temperature variability, trends, and extremes since 1500." In: *Science Mag.* 303, pp. 1499–1503. DOI: 10.1126/science.1093877 (cit. on p. 30).

Main-Knorn, M., B. Pflug, V. Debaecker, et al. (2015). "Calibration and Validation Plan for the L2A Processor and Products of the Sentinel-2 Mission." In: *International Archives of the Photogrammetry, Remote Sensing and Spatial Information Sciences* XL-7/W3, pp. 1249–1255. DOI: 10.5194/isprsarchives-XL-7-W3-1249-2015 (cit. on p. 21).

Main-Knorn, M., B. Pflug, J. Louis, et al. (2017). "Sen2Cor for Sentinel-2." In: *Image and Signal Processing for Remote Sensing XXIII*. Vol. 10427. International Society for Optics and Photonics. DOI: 10.1117/12.2278218 (cit. on pp. 35, 36, 40).

Malenovský, Z. et al. (2012). "Sentinels for science: Potential of Sentinel-1, -2 and -3 missions for scientific observations of ocean, criysphere and land." In: *Remote Sensing of Environment* 120, pp. 91–101. DOI: 10.1016/j.rse.2011.09.026 (cit. on p. 19).

Martimort, P. et al. (2007). "Sentinel-2 Optical High Resolution Mission for GMES Operational Services." In: *Geoscience and Remote Sensing Symposium, 2007. IGARSS 2007. IEEE International*. IEEE, pp. 2677–2680 (cit. on pp. 20, 21).

Mattar, C. et al. (2014). "Impacts of the broadband albedo on actual evapotranspiration estimated by S-SEBI model over an agricultural area." In: *Remote Sensing of Environment* 147, pp. 23–42. DOI: 10.1016/j.rse.2014.02.011 (cit. on pp. 5–7).

MODIS (Mar. 27, 2019). *MODIS user guide v006*. URL: https://www.umb.edu/spectralmass/terra_aqua_modis/v006 (cit. on p. 8).

Müller-Wilm, U., O. Devignot, and L. Pessiot (2017). *Sen2Cor Configuration and User Manual. Ref. S2-PDGS-MPC-L2A-SUM-V2.4*. ESA, p. 53 (cit. on p. 36).

Myhre, G., M. M. Kvalevag, and C. B. Schaaf (2005). "Radiative forcing due to anthropogenic vegetation change based on MODIS surface albedo data." In: *Geophysical Research Letters* 32, pp. 1–4. DOI: 10.1029/2005gl024004 (cit. on p. 69).

Myneni, R. B. et al. (1997). "Estimation of global leaf area index and absorbed PAR using radiative transfer models." In: *IEEE Transactions on Geoscience and Remote Sensing* 35, pp. 1380–1393. DOI: 10.1109/36.649788 (cit. on p. 18).

NASA (Mar. 27, 2019). *Radiative Transfer*. URL: https://atmospheres.gsfc.nasa.gov/climate/?section=139 (cit. on p. 7).

Nguy-Robertson, A., A. A. Gitelson, et al. (2012). "Green Leaf Area Index Estimation in Maize and Soybean: Combining Vegetation Indices to Achieve Maximal Sensitivity." In: *Agronomy Journal* 104, pp. 1336–1347. DOI: 10.2134/agronj2012.0065 (cit. on pp. 15–17, 46, 50).

Nguy-Robertson, A., Y. Peng, et al. (2014). "Estimating green LAI in four crops: Potential of determining optimal spectral bands for a universal algorithm." In: *Agricultural and Forest Meteorology* 192, pp. 140–148. DOI: 10.1016/j.agrformet.2014.03.004 (cit. on pp. 16, 17, 46, 50).

Nicholas, F. W. and J. E. Lewis (1980). *Relationships between aerodynamic roughness and land use and land cover in Baltimore, Maryland*. DOI: 10.3133/pp1099c (cit. on p. 3).

Nicodemus, F. E. et al. (1977). *Geometrical Considerations and Nomenclature for Reflectance*. U. S. Department of Commerce, National Bureau of Standards (cit. on pp. 6, 7).

Ollinger, S. V. et al. (2008). "Canopy nitrogen, carbon assimilation, and albedo in temperate and boreal forests: Functional relations and potential climate feedbacks." In: *Proceedings of the National Academy of Sciences* 105, pp. 19336–19341. DOI: 10.1073/pnas.0810021105 (cit. on pp. 6, 67).

Pandzic, M. et al. (June 2016). "Assessment of the geometric quality of Sentinel-2 data." In: *ISPRS - International Archives of the Photogrammetry, Remote Sensing and Spatial Information Sciences* XLI-B1, pp. 489–494. DOI: 10.5194/isprs-archives-xli-b1-489-2016 (cit. on p. 54).

Pasqualotto, N. et al. (Feb. 2019). "Multi-Crop Green LAI Estimation with a New Simple Sentinel-2 LAI Index (SeLI)." In: *Sensors* 19, pp. 1–19. DOI: 10.3390/s19040904 (cit. on pp. 14, 46).

Perez, P. J., F. Castellvi, and A. Martínez-Cob (Jan. 2008). "A simple model for estimating the Bowen ratio from climatic factors for determining latent and sensible heat flux." In: *Agricultural and Forest Meteorology* 148, pp. 25–37. DOI: 10.1016/j.agrformet.2007.08.015 (cit. on p. 3).

Pielke, R. A. and R. Avissar (1990). "Influence of landscape structure on local and regional climate." In: *Landscape Ecology* 4, pp. 133–155 (cit. on pp. 24, 52, 53, 61, 67, 97).

Pinty, B. and M. M. Verstraete (1992). "On the Design and Validation of Surface Bidirectional Reflectance and Albedo Models." In: *Remote Sensing of Environment* 41, pp. 155–167. DOI: 10.1016/0034-4257(92)90075-U (cit. on pp. 6, 7).

Pokorny, R. and S. Stojnic (2012). "Leaf area index of Norway spruce stands in relation to age and defoliation." In: *Beskydy* 5, pp. 173–180. DOI: 10.11118/beskyd201205020173 (cit. on pp. 87, 89).

Pope, G. and P. Treitz (2013). "Leaf Area Index (LAI) Estimation in Boreal Mixedwood Forest of Ontario, Canada Using Light Detection and Ranging (LiDAR) and WorldView-2 Imagery." In: *Remote Sensing* 5, pp. 5040–5063. DOI: 10.3390/rs5105040 (cit. on pp. 15, 85).

Rautiainen, M., J. Heiskanen, and L. Korhonen (2012). "Seasonal changes in canopy leaf area index and MODIS vegetation products for a boreal forest site in central Finland." In: *Boreal Environment Research* 17, pp. 72–84. ISSN: 1797-2469 (cit. on pp. 79, 81, 82).

Rautiainen, M., P. Stenberg, et al. (2011). "Radiative transfer simulations link boreal forest structure and shortwave albedo." In: *Boreal environment research* 16, pp. 91–100 (cit. on pp. 7, 8, 58).

Rechid, D., T. J. Raddatz, and D. Jacob (Apr. 2008). "Parameterization of snow-free land surface albedo as a function of vegetation phenology based on MODIS data and applied in climate modelling." In: *Theoretical and Applied Climatology* 95, pp. 245–255. DOI: 10.1007/s00704-008-0003-y (cit. on p. 69).

Reichenau, T. G. et al. (2016). "Spatial Heterogeneity of Leaf Area Index (LAI) and Its Temporal Course on Arable Land: Combining Field Measurements, Remote Sensing and Simulation in a Comprehensive Data Analysis Approach (CDAA)." In: *PloS one* (cit. on pp. 14, 17, 18, 51, 52).

Richter, K., C. Atzberger, et al. (2011). "Evaluation of Sentinel-2 Spectral Sampling for Radiative Transfer Model Based LAI Estimation of Wheat, Sugar Beet, and Maize." In: *IEEE Journal of Selected Topics in Applied Earth Observations and Remote Sensing* 4, pp. 458–464. DOI: 10.1109/JSTARS.2010.2091492 (cit. on pp. 16, 18).

Richter, K., T. B. Hank, et al. (2012). "Optimal Exploitation of the Sentinel-2 Spectral Capabilities for Crop Leaf Area Index Mapping." In: *Remote Sensing* 4, pp. 561–582. DOI: 10.3390/rs4030561 (cit. on pp. 15, 17, 18).

Robinson, D. A. and G. Kukla (1984). "Albedo of a dissipating snow cover." In: *Journal of Climate and Applied Meteorology* 23, pp. 1626–1634. DOI: 10.1175/1520-0450(1984)023<1626:AOADSC>2.0.CO;2 (cit. on p. 69).

Román, M. O. et al. (2009). "The MODIS (Collection V005) BRDF/albedo product: Assessment of spatial representativeness over forested landscapes." In: *Remote Sensing of Environment* 113, pp. 2476–3498. DOI: 10.1016/j.rse.2009.07.009 (cit. on pp. 6–8, 67).

Salimi-Kouchi, H. et al. (2013). "Fractional Vegetation Cover Estimation in Urban Environments." In: *ISPRS-International Archives of the Photogrammetry, Remote Sensing and Spatial Information Sciences* XL-1/W3, pp. 357–360 (cit. on p. 9).

Sauer, T. J. and R. Horton (2005). "Soil Heat Flux." In: *Micrometeorology in Agricultural Systems*. Ed. by J. L. Hatfield and J. M. Baker. Vol. 47. American Society of Agronomy, Crop Science Society of America, and Soil Science Society of America, pp. 131–154. DOI: 10.2134/agronmonogr47.c7 (cit. on p. 3).

Schaepman-Strub, G. et al. (2006). "Reflectance quantities in optical remote sensing—Definitions and case studies." In: *Remote Sensing of Environment* 103, pp. 27–42. DOI: 10.1016/j.rse.2006.03.002 (cit. on pp. 5–8).

Schiffmann, B. et al. (2008). "Estimation of Leaf Area Index (LAI) through the acquisition of ground truth data in Yosemite national park." In: *ASRPS 2008 Annual Conference, Portland, Oregon* (cit. on pp. 15, 16, 39, 48, 50, 55, 84–86, 89, 98).

Schlerf, M., C. Atzberger, and J. Hill (Mar. 2005). "Remote sensing of forest biophysical variables using HyMap imaging spectrometer data." In: *Remote Sensing of Environment* 95, pp. 177–194. DOI: 10.1016/j.rse.2004.12.016 (cit. on pp. 87, 89).

Scire, J. S. et al. (2000). *A user's guide for the CALMET meteorological model (version 5.0). (Version 5.0)*. Tech. rep. Eartch Tech, Inc. 196 Baker Avenue Concord, MA 01742, p. 332 (cit. on p. 2).

Scurlock, J. M. O., G. P. Asner, and S. T. Gower (2001). "Global leaf area index from field measurements, 1932-2000." In: *ORNL DAAC*. DOI: 10.3334/ORNLDAAC/584 (cit. on pp. 24, 56, 78, 91–93, 98).

Sellers, P. J., F. G. Hall, et al. (1997). "BOREAS in 1997: Experiment overview, scientific results, and future directions." In: *Journal of Geophysical Research* 102, pp. 731–769. DOI: 10.1029/97JD03300 (cit. on p. 7).

Sellers, P. J., S. O. Los, et al. (1996). "A revised land surface parameterization (SiB2) for atmospheric GCMs. Part II: The generation of global fields of terrestrial biophysical parameters from satellite data." In: *Journal of Climate* 9, pp. 706–737 (cit. on p. 9).

Settle, J. J. and N. A. Drake (1993). "Linear mixing and the estimation of ground cover proportions." In: *International Journal of Remote Sensing* 14, pp. 1159–1177 (cit. on p. 10).

Silva, B. B. da et al. (2016). "Procedures for calculation of the albedo with OLI-Landsat 8 images: Application to the Brazilian semi-arid." In: *Revista Brasileira de Engenharia Agrícola e Ambiental* 20, pp. 3–8. DOI: 10.1590/1807-1929/agriambi.v20n1p3-8 (cit. on p. 7).

Simpraga, M. et al. (2011). "Seasonal variation of LAI in the footprint of a flux measurement tower." In: *Starters in het Bosonderzoek 2011*. Brussel (cit. on p. 82).

Smith, R. B. (2010). "The heat budget of the earth's surface deduced from space." In: *Yale University Center for Earth Observation: New Haven, CT, USA* (cit. on p. 40).

Sobrino, J. et al. (2008). "Land surface emissivity retrieval from different VNIR and TIR sensors." In: *IEEE Transactions on Geoscience and Remote Sensing* 46 (316-327). DOI: 10.1109/TGRS.2007.904834 (cit. on p. 9).

Solomon, S. et al. (2007). *Climate change 2007-the physical science basis: Working group I contribution to the fourth assessment report of the IPCC*. Vol. 4. Cambridge university press (cit. on p. 30).

Somers, B. et al. (2011). "Endmember variability in spectral mixture analysis: A review." In: *Remote Sensing of Environment* 115, pp. 1603–1616. DOI: 10.1016/j.rse.2011.03.003 (cit. on pp. 9–11, 13).

Sonohat, G., P. Balandier, and F. Ruchaud (Oct. 2004). "Predicting solar radiation transmittance in the understory of even-aged coniferous stands

in temperate forests." In: *Annals of Forest Science* 61, pp. 629–641. DOI: 10.1051/forest:2004061 (cit. on p. 87).

Souza, J. D. de, J. C. Ceballos, and B. B. da Silva (2014). "Surface albedo obtained with MODIS images in cases of low and high aerosol loading in the atmosphere." In: *Brasilian Journal of Geophysics* 32, pp. 5–20. DOI: 10.22564/rbgf.v32i1.421 (cit. on p. 7).

Stauffer, P. et al. (2007). "Impact of vegetation cover estimates on regional climate forecasts." In: (cit. on p. 1).

Stephens, G. L. et al. (Mar. 2015). "The albedo of Earth." In: *Reviews of Geophysics* 53, pp. 141–163. DOI: 10.1002/2014rg000449 (cit. on p. 69).

Sterba, H., G. Dirnberger, and T. Ritter (July 2018). "The Contribution of Forest Structure to Complementarity in Mixed Stands of Norway Spruce (Picea abies L. Karst) and European Larch (Larix decidua Mill.)" In: *Forests* 9, pp. 1–17. DOI: 10.3390/f9070410 (cit. on p. 86).

Strengers, B. J. et al. (Apr. 2010). "Assessing 20th century climate-vegetation feedbacks of land-use change and natural vegetation dynamics in a fully coupled vegetation-climate model." In: *International Journal of Climatology* 30, pp. 2055–2065. DOI: 10.1002/joc.2132 (cit. on p. 1).

Suhet (2015). *Sentinel-2 User Handbook*. ESA (cit. on pp. 20–22).

Tanaka, S. et al. (2015). "Spectral Index for Quantifying Leaf Area Index of Winter Wheat by Field Hyperspectral Measurements: A Case Study in Gifu Prefecture, Central Japan." In: *Remote Sensing* 7, pp. 5329–5346. DOI: 10.3390/rs70505329 (cit. on pp. 14, 16, 17, 46, 50).

Tasumi, M., R. G. Allen, and R. Trezza (2008). "At-Surface Reflectance and Albedo from Satellite for Operational Calcualtion of Land Surface Energy Balance." In: *Journal of Hydrologic Engineering* 13, pp. 51–63 (cit. on p. 8).

Tian, X. et al. (Sept. 2011). "Estimating zero-plane displacement height and aerodynamic roughness length using synthesis of LiDAR and SPOT-5 data." In: *Remote Sensing of Environment* 115, pp. 2330–2341. DOI: 10.1016/j.rse.2011.04.033 (cit. on p. 3).

Turner, D. P. et al. (1999). "Relationships between leaf area index and Landsat TM spectral vegetation indices across three temperate zone sites." In: *Remote Sensing of Environment* 70, pp. 52–68. DOI: 10.1016/S0034-4257(99)00057-7 (cit. on pp. 13, 14, 16, 86).

Verrelst, J. et al. (Oct. 2015). "Optical remote sensing and the retrieval of terrestrial vegetation bio-geophysical properties - A review." In: *ISPRS*

Journal of Photogrammetry and Remote Sensing 108, pp. 273–290. DOI: 10.1016/j.isprsjprs.2015.05.005 (cit. on p. 1).

Viña, A. et al. (2011). "Comparison of different vegetation indices for the remote assessment of green leaf area index of crops." In: *Remote sensing of Environment* 115, pp. 3468–3478. DOI: 10.1016/j.rse.2011.08.010 (cit. on pp. 14–18, 46, 50).

Vose, J. M. et al. (1994). "Factors influencing the amount and distribution of leaf area of pine stands." In: *Ecological Bulletins* 43, pp. 102–114 (cit. on p. 87).

Wakonigg, H. (1967). "Witterungsklimatologie der Steiermark." PhD thesis. Universität Graz, p. 255 (cit. on p. 30).

Wakonigg, H. (1978). *Witterung und Klima in der Steiermark*. dbv-Verlag für die Technische Universität Graz, p. 473 (cit. on p. 30).

Wakonigg, H. and A. Podesser (Oct. 31, 2018). *Klimaatlas Steiermark*. URL: http://www.umwelt.steiermark.at/cms/ziel/16178332/DE/ (cit. on pp. 30, 31).

Wang, G. et al. (2002). "Improvement in mapping vegetation cover factor for the universal soil loss equation by geostatistical methods with Landsat Thematic Mapper images." In: *International Journal of Remote Sensing* 23, pp. 3649–3667. DOI: 10.1080/01431160110114538 (cit. on p. 9).

Wang, Q. et al. (2005). "On the relationship of NDVI with leaf area index in a deciduous forest site." In: *Remote Sensing of Environment* 94, pp. 244–255. DOI: 10.1016/j.rse.2004.10.006 (cit. on pp. 14, 17).

Wang, S. and A. Davidson (2007). "Impact of climate variations on surface albedo of a temperate grassland." In: *Agricultural and Forest Meteorology* 142, pp. 133–142. DOI: 10.1016/j.agrformet.2006.03.027 (cit. on pp. 6, 7, 58).

Wang, Weiguo et al. (June 2008). "An Evaluation of a Diagnostic Wind Model (CALMET)." In: *Journal of Applied Meteorology and Climatology* 47, pp. 1739–1756. DOI: 10.1175/2007jamc1602.1 (cit. on p. 2).

Wegehenkel, M. (Aug. 2009). "Modeling of vegetation dynamics in hydrological models for the assessment of the effects of climate change on evapotranspiration and groundwater recharge." In: *Advances in Geosciences* 21, pp. 109–115. DOI: 10.5194/adgeo-21-109-2009 (cit. on p. 1).

Weier, J. and D. Herring (2000). *Measuring Vegetation (NDVI and EVI). NASA Earth Observatory*. URL: https://earthobservatory.nasa.gov/features/MeasuringVegetation (visited on 12/06/2018) (cit. on p. 16).

Weiss, M. et al. (2004). "Review of methods for in situ leaf area index (LAI) determination Part II. Estimation of LAI, errors and sampling." In: *Agricultural and Forest Meteorology* 121, pp. 37–53. DOI: 10.1016/j.agrformet.2003.08.001 (cit. on pp. 14, 16).

Wittich, K.-P. (1997). "Some simple relationships between land-surface emissivity, greenness and the plant cover fraction for use in satellite remote sensing." In: *International Journal of Biometeorology* 41, pp. 58–64. DOI: 10.1007/s004840050054 (cit. on p. 13).

Wu, C. and A. T. Murray (2003). "Estimating impervious surface distribution by spectral mixture analysis." In: *Remote Sensing of Environment* 84, pp. 493–505. DOI: 10.1016/S0034-4257(02)00136-0 (cit. on p. 10).

Xavier, A. C. and C. A. Vettorazzi (2004). "Monitoring leaf area index at watershed level through NDVI from Landsat-7/ETM+ data." In: *Scientia Agricola* 61, pp. 243–252. DOI: 10.1590/S0103-90162004000300001 (cit. on pp. 15, 16).

Zeng, X. et al. (2000). "Derivation and evaluation of global 1-km fractional vegetation cover data for land modeling." In: *Journal of Applied Meteorology* 39, pp. 826–839. DOI: 10.1175/1520-0450(2000)039<0826:DAEOGK>2.0.CO;2 (cit. on p. 1).

Zheng, G. and L. M. Moskal (2009). "Retrieving Leaf Area Index (LAI) Using Remote Sensing: Theories, Methods and Sensors." In: *Sensors* 9, pp. 2719–2745. DOI: 10.3390/s90402719 (cit. on pp. 15, 16).

Zhou, L. et al. (2003). "Comparison of seasonal and spatial variations of albedos from Moderate-Resolution Imaging Spectroradiometer (MODIS) and Common Land Model." In: *Journal of Geophysical Research* 108, pp. 1–15. DOI: 10.1029/2002jd003326 (cit. on p. 69).

Zhu, Z. et al. (2013). "Global Data Sets of Vegetation Leaf Area Index (LAI)3g and Fraction of Photosynthetically Active Radiation (FPAR)3g Derived from Global Inventory Modeling and Mapping Studies (GIMMS) Normalized Difference Vegetation Index (NDVI3g) for the Period 1981 to 2011." In: *Remote Sensing* 5, pp. 927–948. DOI: 10.3390/rs5020927 (cit. on p. 15).

Appendix

List of Acronyms

AISA	Aircraft-mounted hyperspectral imaging spectroradiometer
ASTER	Advanced Spaceborne Thermal Emission and Reflection Radiometer
AVHRR	Advanced Very High Resolution Radiometer
BHR	Bihemispherical Reflectance
BRDF	Bidirectional Reflectance Distribution Function
CALMET	California Meteorological Model
CHRIS	Compact High Resolution Imaging Spectrometer
DHP	Digital Hemispherical Photography
DN	Digital Number
DOY	Day of Year
ECV	Essential Climate Variables
ESA	European Space Agency
ETM+	Enhanced Thematic Mapper Plus
FVC	Fraction of Vegetation Cover
GCOS	Global Climate Observing System
GMES	Global Monitoring for Environment and Security
GBVI	Green Blue Vegetation Index
GVI	Green Vegetation Index
IMD	Imperviousness Density
IPCC	International Panel on Climate Change
LAI	Leaf Area Index
LCLU	Land Cover / Land Use
LiDAR	Light Detection and Ranging
LUT	Look-Up Table
MODIS	Moderate Resolution Imaging Spectroradiometer
MODTRAN	MODerate resolution atmospheric TRANsmission
MSAVI	Modified Soil-Adjusted Vegetation Index
MSI	MultiSpectral Instrument
MTVI	Modified Triangulation Vegetation Index

NDI	Normalised Difference Index
NDVI	Normalised Difference Vegetation Index
NIR	Near-Infrared
OLS	Ordinary Least Squares
RMA	Reduced Major Axis
RSR	Reduced Simple Ratio
RTM	Radiative Transfer Model
RTR	Raabtal Region
RUSLE	Revised Universal Soil Loss Equation
SAR	Synthetic-aperture radar
SAVI	Soil-Adjusted Vegetation Index
SES	South-East Styria
SMA	Spectral Mixture Analysis
SPOT	Satellite Pour l'Observation de la Terre
SR	Simple Ratio
SVI	Spectral Vegetation Index
SWIR	Short-Wave Infra-Red
TM	Thematic Mapper
TOA	Top Of Atmosphere
USLE	Universal Soil Loss Equation
VARI	Variable Atmospherically Resistant Index
VI	Vegetation Index
VNIR	Visible and Near Infra-Red
WDRVI	Wide Dynamic Range Vegetation Index

Boxplots

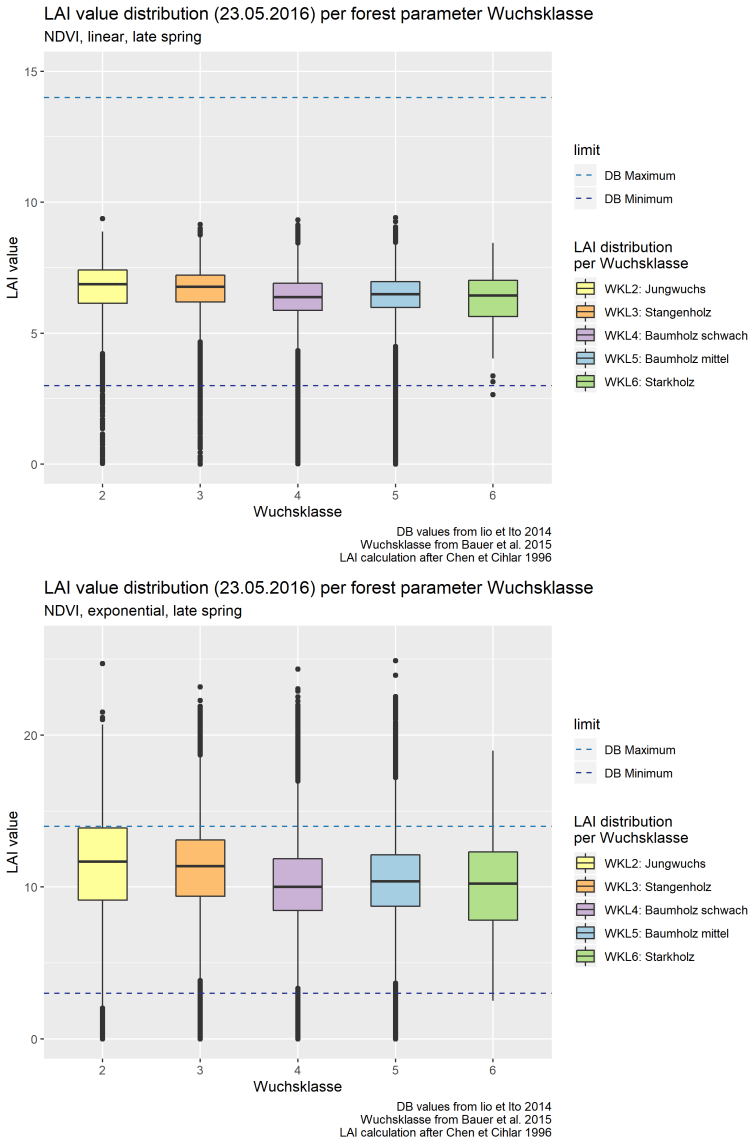

Figure B.1: LAI value distribution per WKL for linear NDVI-derived LAI in spring (top) and exponential NDVI-derived LAI in spring (bottom) after Chen and Cihlar, 1996

Source: own illustration

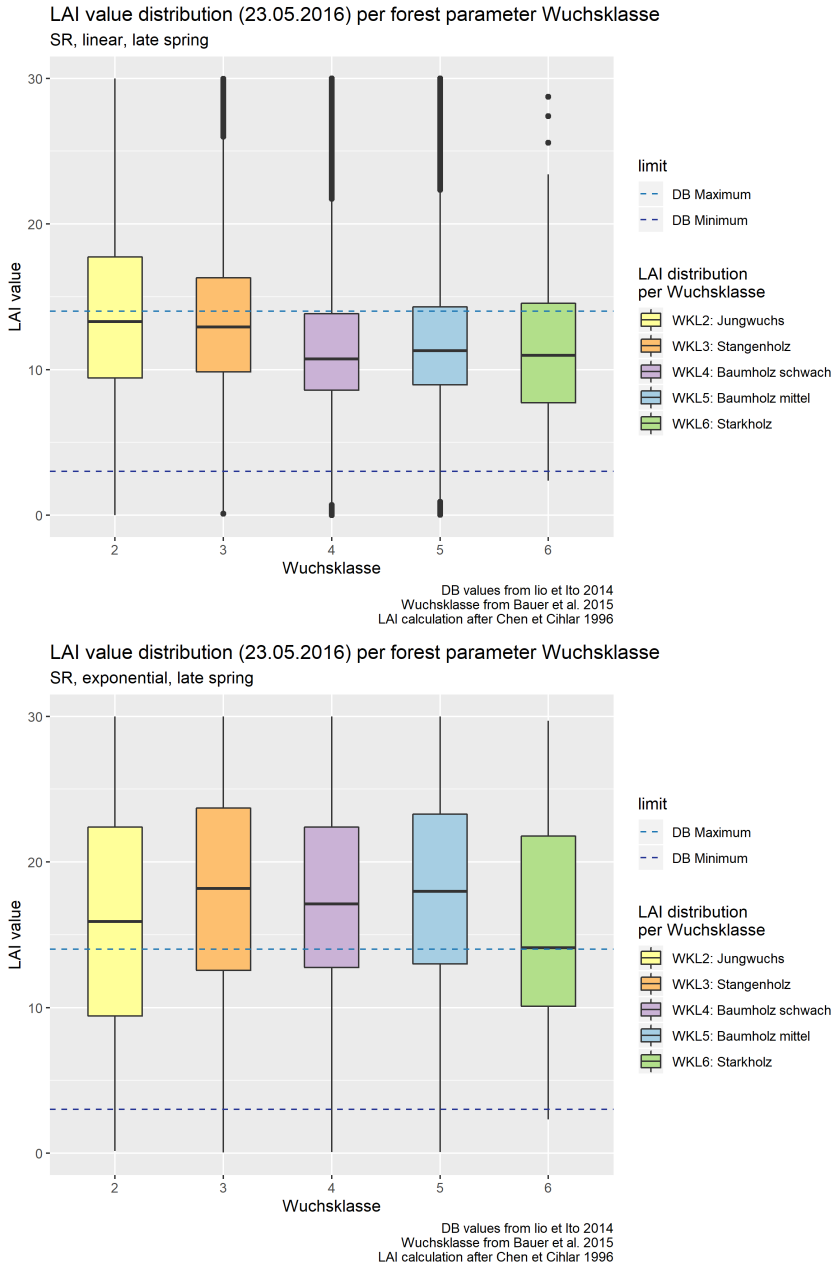

Figure B.2: LAI value distribution per WKL for linear SR-derived LAI in spring (top) and exponential SR-derived LAI in spring (bottom) after Chen and Cihlar, 1996

Source: own illustration

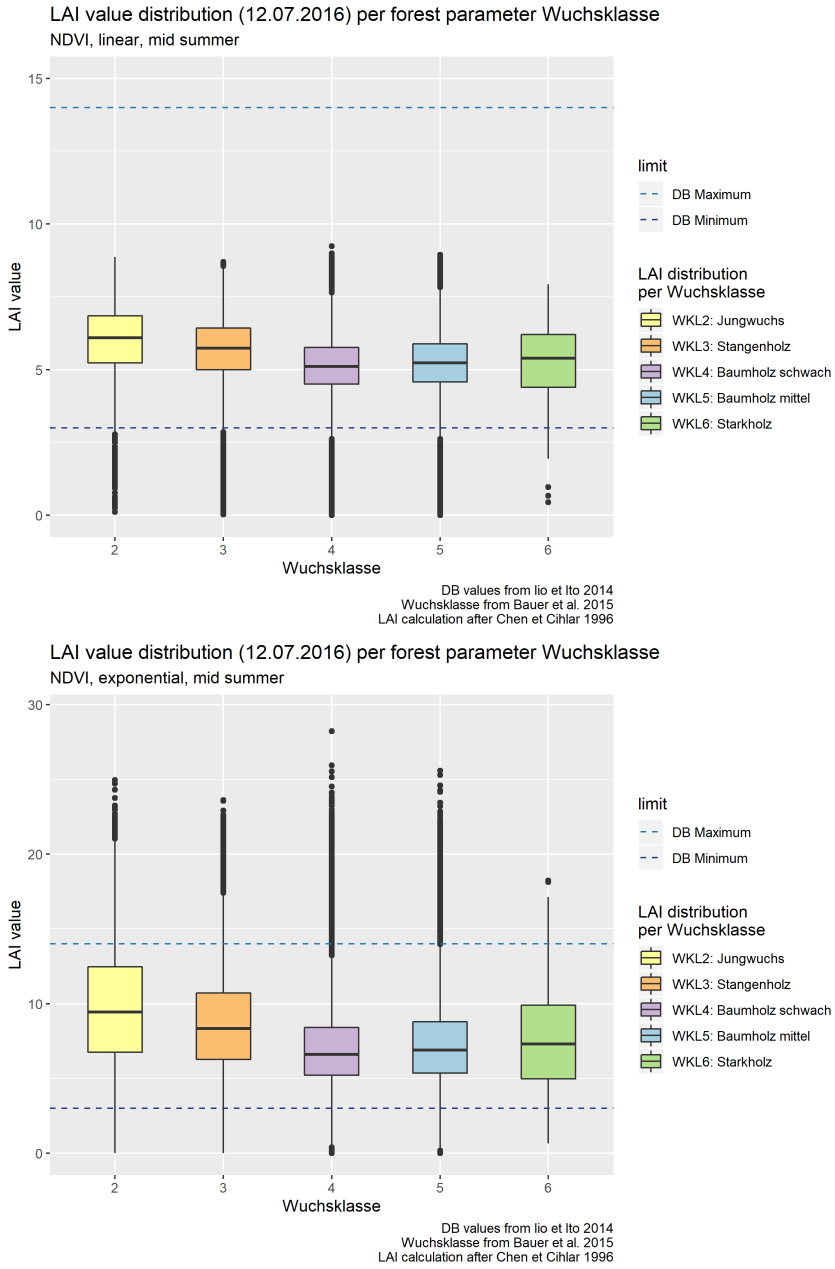

Figure B.3: LAI value distribution per WKL for linear NDVI-derived LAI in summer (top) and exponential NDVI-derived LAI in summer (bottom) after Chen and Cihlar, 1996

Source: own illustration

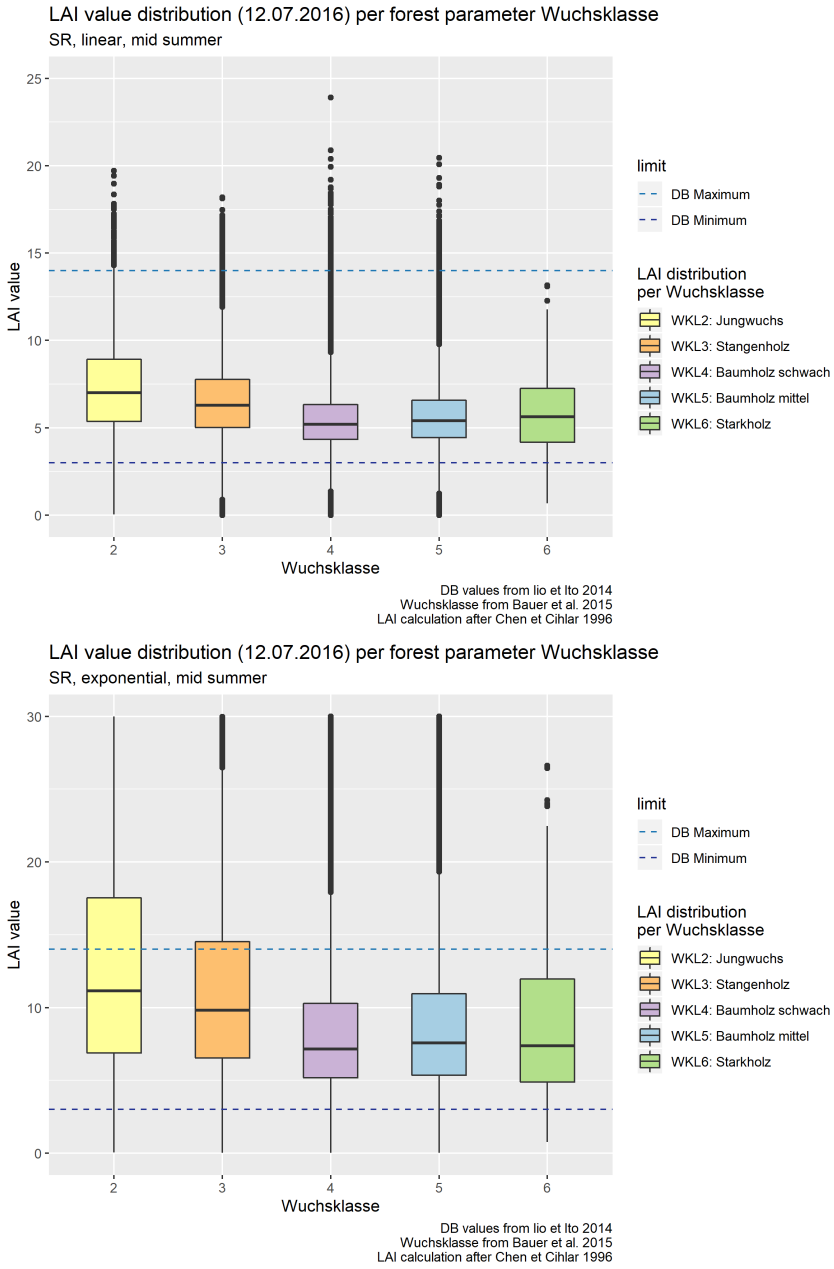

Figure B.4: LAI value distribution per WKL for linear SR-derived LAI in summer (top) and exponential SR-derived LAI in summer (bottom) after Chen and Cihlar, 1996

Source: own illustration

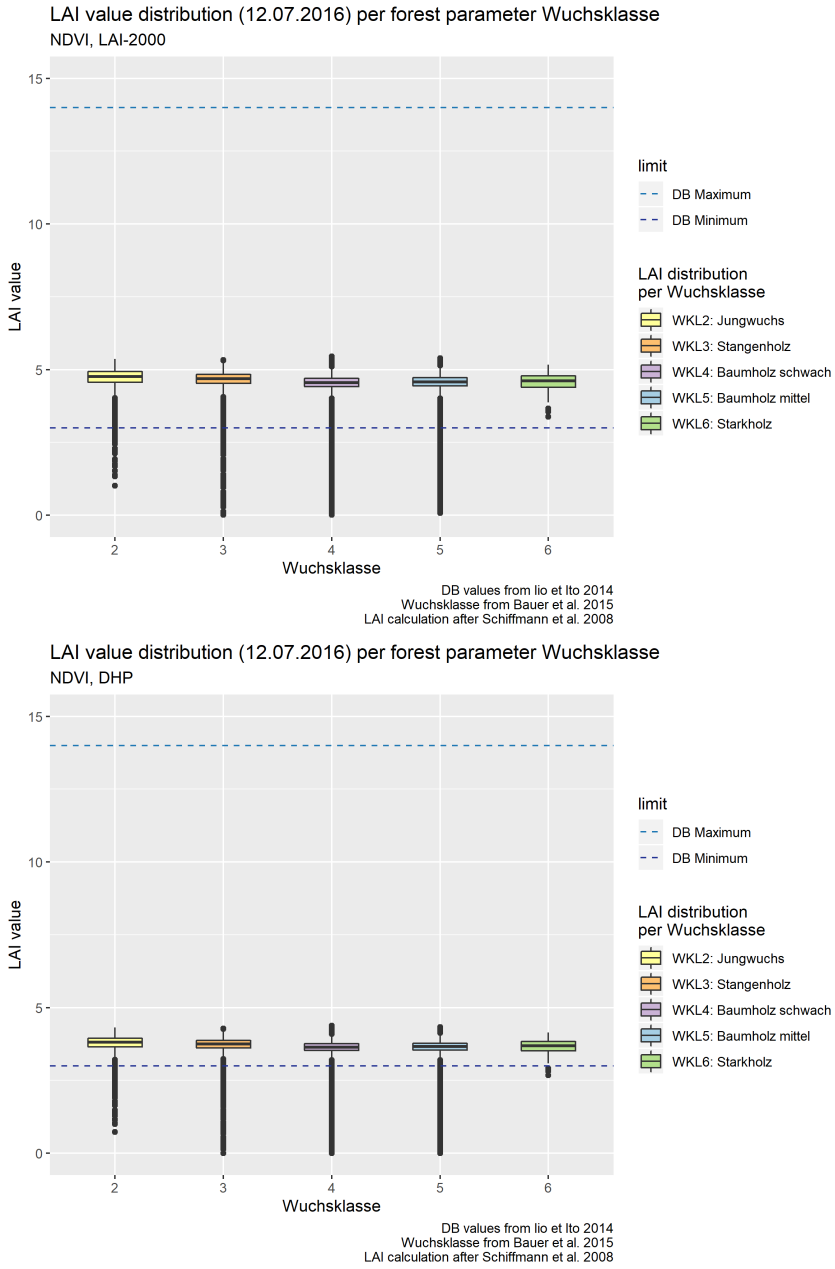

Figure B.5: LAI value distribution per WKL for NDVI-derived LAI in correlation with LAI-2000 (top) and DHP (bottom) after Schiffmann et al., 2008

Source: own illustration

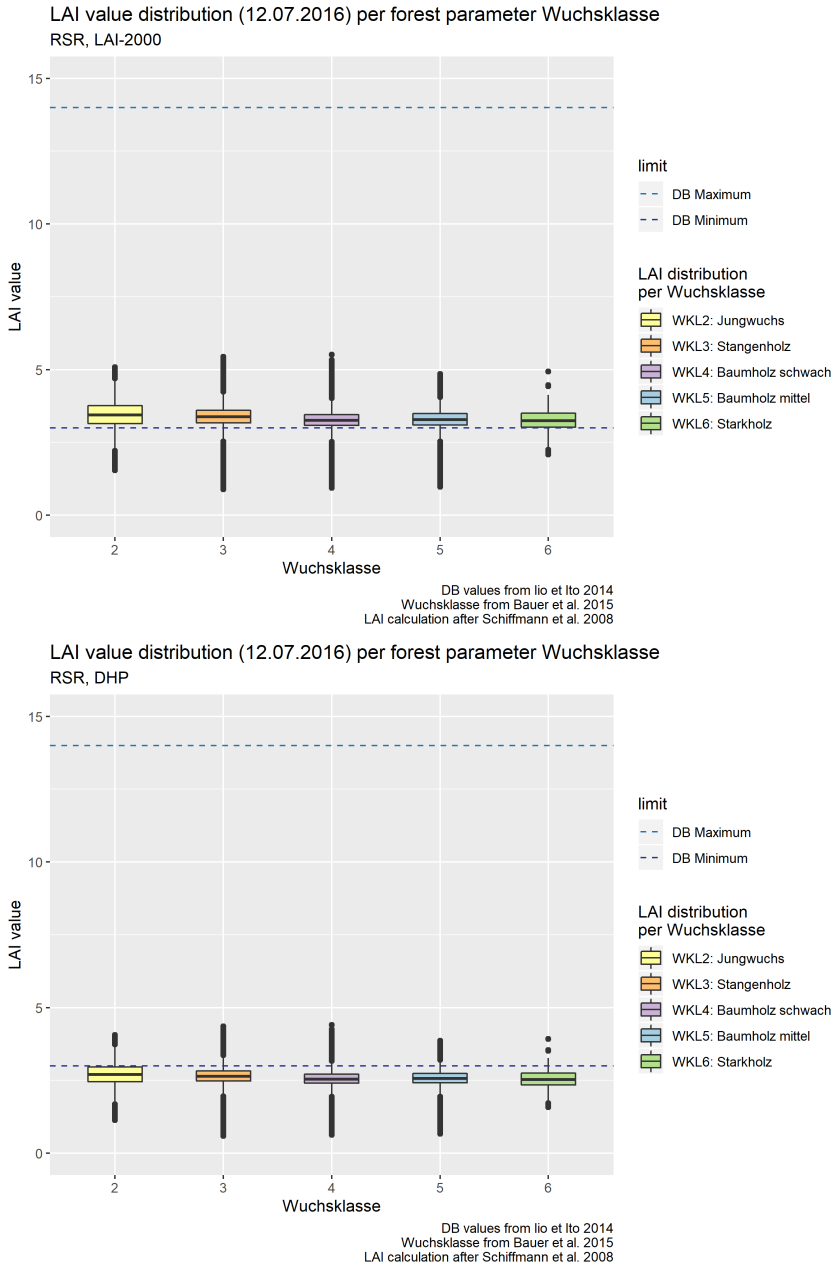

Figure B.6: LAI value distribution per WKL for RSR-derived LAI in correlation with LAI-2000 (top) and DHP (bottom) after Schiffmann et al., 2008

Source: own illustration

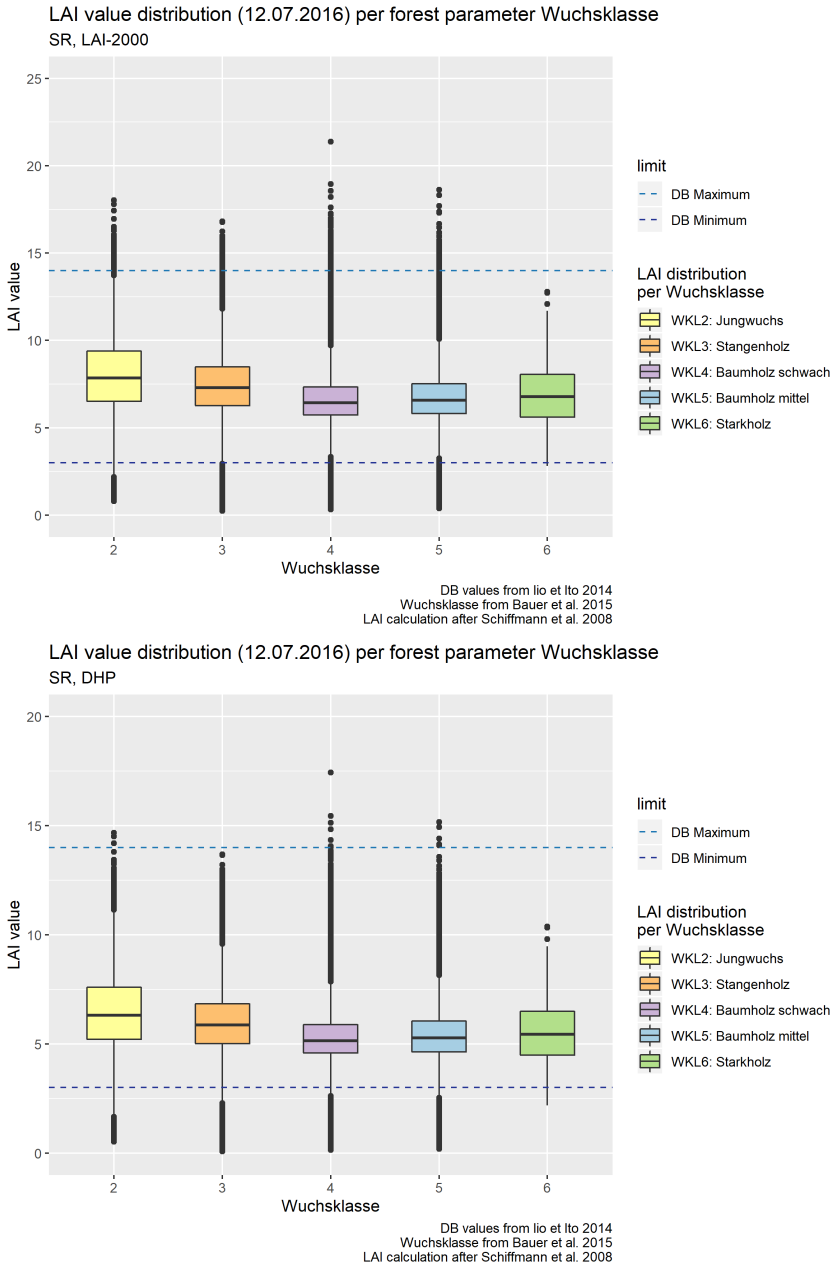

Figure B.7: LAI value distribution per WKL for SR-derived LAI in correlation with LAI-2000 (top) and DHP (bottom) after Schiffmann et al., 2008

Source: own illustration

Acknowledgements

The trouble with having an open mind, of course, is that people will insist on coming along and trying to put things in it.

- Terry Pratchett

Thank you to everyone, who helped me along the way with their support, insightful feedback, and infinite patience.

Prof. Mathias Schardt

Henning, Nora, my friends and family